8-2018

Probabilistic Assessment of Soil Liquefaction Potential and Mitigation

Mengfen Shen
Clemson University, mengfes@g.clemson.edu

PROBABILISTIC ASSESSMENT OF SOIL LIQUEFACTION POTENTIAL AND MITIGATION

A Dissertation
Presented to
the Graduate School of
Clemson University

In Partial Fulfillment
of the Requirements for the Degree
Doctor of Philosophy
Civil Engineering

---

by
Mengfen Shen
August 2018

Accepted by:
Dr. Qiushi Chen, Committee Chair
Dr. C. Hsein Juang, Co-Chair
Dr. James R. Martin
Dr. Jie Zhang

ABSTRACT

It has been well observed and reported that much of the great losses in past earthquakes, such as the 2011 Tohoku earthquake and the 2010-2011 Canterbury earthquake, were attributed to soil liquefaction and the associated ground deformation. Thus, any relevant research that contributes to the worldwide efforts to assess and mitigate liquefaction hazards is considered timely and worthwhile. This dissertation is aimed at addressing two aspects of liquefaction research: (1) improving the existing probabilistic methods for both location-specific and areal liquefaction potential evaluation, (2) creating visualization-based procedure for assessing the effectiveness of dynamic compaction in the liquefaction hazards mitigation. Both are deemed timely contributions to the course of earthquake hazard mitigation efforts by the engineering communities, which are the main objectives of the research.

The dissertation research consists of three separate but related efforts that as a whole address the two main objectives of this research. The first part, "Predicting liquefaction probability based on shear wave velocity: an update", was intended to improve the existing liquefaction evaluation method using shear wave velocity (V_s). The liquefaction evaluation models using V_s were calibrated based on the expanded V_s-based database was created. In this work, the scientific merits of various generalized linear regression models were investigated. Based on the findings of this investigation, the optimal models were recommended for the evaluation of location-specific liquefaction probability.

In the second part of the dissertation research, concerning the "Random field-based regional liquefaction hazard mapping — data inference and model verification using a synthetic digital soil field", the focus was on the areal or regional evaluation of liquefaction potential. Although the random field has been applied to many geotechnical problems, including liquefaction evaluation, abundant field data for assessing various issues of random field modeling, such as the accuracy and the computational demand, are lacking. To this end, an extremely detailed three-dimensional synthetic digital soil field was created, which enabled an extensive data inference and model calibration using the random field theories. This part of the dissertation work was more on fundamental scientific exploration. Nevertheless, it set the foundation for establishing the random field-based visualization procedure for liquefaction mitigation problem in the third part of this dissertation work.

In the third and last part of the dissertation work: "Mitigation of liquefaction hazard by dynamic compaction — a random field perspective", the effectiveness of dynamic compaction (DC) in the mitigation of liquefaction hazards was assessed from a random field perspective. The traditional assessment of this effectiveness was through *in situ* tests before and after DC, and the effectiveness of such approach depends on whether the one-to-one and side-by-side field tests before and after DC are available. In reality, such ideal situation almost always does not exist due to the construction practicality in the operation of DC. The random field modeling removed such need for the one-to-one and side-by-side field tests before and after DC. In this part, a random field based visualization procedure was created so that the liquefaction potential at the entire project site before

and after DC could be clearly compared. The random field based visualization procedure was demonstrated as a practical tool by which the effect of DC could be easily communicated between the engineers and their clients. The scientific endeavor in the creation of a random field based visualization procedure to help solve a practical problem was deemed significant.

In summary, the three parts of this dissertation work as a whole have achieved the two main objectives of the research regarding the liquefaction potential evaluation and the liquefaction mitigation. The scientific merits through these three parts of dissertation work have been demonstrated.

DEDICATION

For my beloved husband

Zhanpu Song

Who always loves, understands, encourages, and supports me.

ACKNOWLEDGMENTS

I would like to express my deepest and most sincere gratitude to my co-advisors, Dr. C. Hsein Juang and Dr. Qiushi Chen. Your guidance and support throughout my time at Clemson University have not only influenced my research work but my professional career as well. I have been greatly inspired by your example and more than grateful for all you've done to prepare me for my career. Without you, it would not have been possible for me to complete my dissertation and other degree requirements.

I am also very grateful for my dissertation committee. To Dr. James R. Martin, thank you for providing me insights from the perspectives of civil engineering practice, and inspiring me to be an outstanding graduate researcher. To Dr. Jie Zhang, thank you for helping me to build firm foundations of my research. Your questions and comments always drove me to think deeply about my work.

I would also like to thank my colleagues, Chaofeng Wang, Wenping Gong, Wenxin Liu, and Weiwei Zhan. Thank you for your supports as we navigated this research journey together.

Mostly, I'm beyond gratitude for those who made me at this point. To my dear husband, my parents, my brother and sister, it is your unconditional love that have made this accomplishment possible. To my dearest friends at Clemson, Kathy and Corina, your joyful companionship on every Friday evening has given me strength to continue my journey. To my host family and friends, the Bacher family, Breanna, Sherri and Rick, you all made my adaptation to a brand-new life smoothly.

Finally, I would like to acknowledge the financial supports from the China Scholarship Council (CSC) throughout this four-year doctoral program. I would also like to acknowledge the supports from the Glenn Department of Civil Engineering at Clemson University, the American International Group (AIG) company, and the Risk Engineering and System Analytics (RESA) center.

TABLE OF CONTENTS

Page

LIST OF TABLES

Table Page

LIST OF FIGURES

Figure Page

List of Figures (Continued)

Figure Page

List of Figures (Continued)

Figure Page

List of Figures (Continued)

Figure Page

CHAPTER I

INTRODUCTION

Problem Statement

Soil liquefaction and liquefaction-induced damage to buildings, lifeline systems and harbor facilities, have been widely observed in many past earthquakes. For example, in the 1995 Kobe earthquake, the impact of liquefaction was found to be greatest on lifelines, mainly on the failure of bridges, buried pipelines, and port facilities (Hamada et al. 1996; Ishihara 1997). In the 1999 Chi-Chi earthquake, soil liquefaction was one of the main causes to the losses of buildings and infrastructures ranging from $20 billion to $30 billion (Uzarski and Arnold, 2001). More recently, about 27,000 houses were damaged in the Tohoku and Kanto districts due to liquefaction during the 2011 Tohoku, Japan earthquake (Ogasawara et al. 2012), and in the 2010-2011 Canterbury, New Zealand earthquakes, approximately half of the $30-billion losses was attributed to soil liquefaction (Cubrinovski et al., 2014).

In light of the great losses attributed to liquefaction in the past earthquakes, especially in the recent Tohoku earthquake and Canterbury earthquake, it is considered timely and significant to conduct research that contributes to the worldwide efforts to assess and mitigate liquefaction hazards. In this dissertation work, the effort is directed to two aspects of liquefaction research: (1) improve the existing probabilistic methods for both location-specific and areal liquefaction potential evaluation, (2) create visualization-based procedure for assessing the effectiveness of ground improvement in the mitigation

of liquefaction hazards. Thus, the main thrust of this dissertation work is to improve/create methods for the liquefaction evaluation and the mitigation of liquefaction hazards through the use of probabilistic and random field approaches.

Objectives and Scope

The main objectives of this research are: (1) to improve the existing probabilistic liquefaction evaluation methods, (2) to study the effectiveness of dynamic compaction in the mitigation of liquefaction hazards.

The scope of this research covers the evaluation of liquefaction probability of sand and silty sand using shear wave velocity (V_s)-based and cone penetration test (CPT)-based liquefaction databases. It covers the location-specific and areal (or regional) evaluation of the probability of liquefaction using case histories and synthetic data. The research work covers the liquefaction potential evaluation and the mitigation of liquefaction hazard. All in all, the scope of the dissertation work is covered by three separate but related journal papers that as a whole address the two main objectives of this research.

Dissertation Organization

This dissertation consists of six chapters. In Chapter I (this chapter), an introduction, including the problem statement, the objectives and scope, and organization of the dissertation, is presented that sets the stage for the entire dissertation. Chapter II, presents the background and methodologies that are required for conducting the dissertation research. This chapter covers the deterministic and probabilistic methods for evaluation

of liquefaction potential of soils, and the countermeasures for liquefaction hazard mitigation. Chapter III through Chapter V present, in sequence, the contents of three journal papers that deal with different aspects of this dissertation work.

In Chapter III, a similar form of a journal paper on "Predicting liquefaction probability based on shear wave velocity: an update" is presented. Here, logistic regression as a form of the generalized linear regression is adopted to assess and update the probabilistic liquefaction potential models using an expanded database of case histories. The optimal models are recommended for both the existing and the expanded liquefaction database.

Chapter IV presents a similar form of a journal paper, "Random field-based regional liquefaction hazard mapping - data inference and model verification using a synthetic digital soil field." In this chapter, an extremely detailed three-dimensional synthetic digital soil field is artificially generated and used to assess and compare three random field-based models for liquefaction hazard mapping.

Chapter V presents the contents of a journal paper, "Mitigation of liquefaction hazard by dynamic compaction - a random field perspective", which is under review. Here the effect of dynamic compaction is assessed through a case study using a random field model. The outcome of the study demonstrates this random field-based visualization procedure as an effective tool in assessing the effect and benefits of dynamic compaction in the mitigation of liquefaction hazard.

Finally, the conclusions and recommendations are made in Chapter VI.

CHAPTER II

METHODS FOR LIQUEFACTION POTENTIAL ASSESSMENT AND LIQUEFACTION MITIGATION

Deterministic Methods for Liquefaction Potential Assessment

Cyclic stress-based simplified methods have been widely used for liquefaction potential evaluation. While the original simplified procedure pioneered by Seed and Idriss (1971 & 1982) was based on a large number of fundamental laboratory studies supplemented with some field observations, the more recent simplified methods were almost always developed solely based on the database of field cases using the framework of the original simplified procedure. In the simplified methods, the seismic loading that can cause a soil to liquefy is generally expressed in terms of cyclic stress ratio (CSR). Because the simplified methods were developed based on calibration with field data that were derived from different earthquake magnitudes and with different overburden stresses, CSR is often "normalized" to a reference state with moment magnitude M_w = 7.5 and effective overburden stress σ'_v = 100 kPa. At the reference state, the CSR is often denoted as $CSR_{7.5,\sigma}$, which may be expressed as follows (e.g., Youd et al. 2001; Juang et al. 2006; Boulanger and Idriss 2012):

$$CSR_{7.5,\sigma} = 0.65\left(\frac{\sigma_v}{\sigma'_v}\right)\left(\frac{a_{max}}{g}\right)\left(\frac{r_d}{MSF \cdot K_\sigma}\right) \tag{2.1}$$

where σ_v = the total overburden stress at the depth of interest (kPa), σ'_v = the effective stress at the depth of interest (kPa), g = the unit of the acceleration of gravity, a_{max} = the peak horizontal ground surface acceleration (a_{max}/g is dimensionless), r_d = the depth-dependent stress reduction factor (dimensionless), MSF = the magnitude scaling factor (dimensionless), and K_σ = the overburden stress adjustment factor (dimensionless). For the convenience of presentation hereinafter, the normalized cyclic stress ratio $CSR_{7.5,\sigma}$ is simply labeled as CSR whenever no confusion would be caused by such use. Details on the input parameters for CSR and the associated component models can be found in the cited references.

In the simplified methods, the liquefaction resistance of a soil is often expressed as cyclic resistance ratio (CRR), based on the concept that CRR is the limiting CSR beyond which the soil will liquefy. An intuitive and empirical method to establish an equation for CRR is to plot the CSR values and *in situ* test data of the collected case histories, such as the corrected SPT blow count ($N_{1,60}$), the corrected CPT tip resistance (q_{t1N}), or the corrected shear wave velocity (V_s), in a two-dimensional chart, and the curve separating the liquefied cases from the non-liquefied cases may be considered as the limiting CSR beyond which the soil will liquefy. This limiting CSR curve thus defines CRR, which may then be expressed as a function of the adopted *in situ* test data. For example, for a saturated sand with little fines, CRR can be expressed as follows (Robertson and Wride, 1998):

$$\mathrm{CRR} = \begin{cases} 0.833[q_{t1N}/1000] + 0.05 & \text{if} \quad q_{t1N} < 50 \\ 93[q_{t1N}/1000]^3 + 0.08 & \text{if} \quad 50 \le q_{t1N} < 160 \end{cases} \tag{2.2}$$

When the soil contains a significant amount of fines, the CRR obtained from Eq. (2.2) has to go through some adjustments. Different ways to adjust CRR for fines content have been recommended and can be found in the literature (e.g., Seed et al., 1983; Youd et al. 2001; Robertson and Wride 1998; Robertson 2010; Boulanger and Idriss 2015).

In a deterministic approach, liquefaction of a soil is predicted to occur if the factor of safety (F_S), defined as the ratio of cyclic resistance ratio (CRR) over cyclic stress ratio (CSR), is less than or equal to 1; on the other hand, no soil liquefaction is said to occur if F_S>1.

Because of the uncertainties that exist in the adopted model and the input data, the computed factor of safety F_S cannot be expressed as a fixed (certain) value; rather, it is more logical to be presented as a random variable. In a deterministic approach, however, these uncertainties are not included in the analysis; rather, a *nominal* factor of safety, a fixed value, is computed using nominal values of input parameters. The term "nominal" value is used herein to refer to a fixed-value estimate of a random variable. For instance, F_S is in fact a random variable, and the nominal F_S is a fixed-value estimate that is based on the standards of practice (e.g., computing with an acceptable procedure using a set of reasonably estimated fixed parameter values). In practice, the nominal factor of safety F_S is often required to be greater than a limiting value (for example, 1.2 to 1.5 as per BSSC 1997) to assure of no occurrence of liquefaction. Use of a limiting (target) F_S value of greater than 1 allows for compensation of the uncertainties that were not included in the deterministic analysis. Choice of a suitable limiting F_S value, however, requires a sound engineering judgment.

Probabilistic Methods for Liquefaction Potential Assessment

To account for all the uncertainties that exist in the adopted model and the input data, probabilistic assessment of liquefaction potential may be performed. The probabilistic assessment of liquefaction potential yields the probability of liquefaction (P_L) for a future case. Thus, the occurrence of liquefaction or not is no longer a "yes-or-no" question. To this end, the liquefaction classes suggested by Chen and Juang (2000) may be used for interpretation of the computed liquefaction probability. For example, if $P_L < 0.15$, it is "almost certain that the soil will not liquefy;" on the other hand, if $P_L > 0.85$, it is "almost certain that the soil will liquefy." The common probabilistic methods for liquefaction potential assessment include the discriminant analysis method, the logistic regression method, artificial neural network method, Bayesian methods, and performance-based methods (Juang et al., 2017a). The logistic regression method and Bayesian methods are more popular thus reviewed as below:

Logistic Regression Method

In the absence of the complete knowledge of model and/or parameter uncertainties, simplified probabilistic models may be established based on database of case histories and later used to estimate the probability of liquefaction of a future case. The simplified models are generally derived from a given database of case histories. For example, many investigators (e.g., Christian and Swiger 1975; Liao et al. 1988; Toprak et al. 1999; Juang et al. 2002; Lai et al. 2006) have derived simplified equations by the logistic regression.

These equations may be expressed in the following form (although a more general form may be used):

$$\ln\left[P_L/(1-P_L)\right] = a_1 + a_2(X) + a_3\ln(\text{CSR}) \tag{2.3}$$

where X is the clean-sand equivalence of corrected SPT blow count or CPT cone tip resistance or shear wave velocity (e.g., Juang et al. 2002).

Logistic regression is often used to predict the response of a binary system. Whether or not a soil will liquefy when subjected to a seismic loading may be considered as a binary event; thus, the logistic regression can be used to predict liquefaction potential. The widespread application of logistic regression may be due to its ease of use (e.g., Juang et al. 2002 & 2015).

The logistic regression is a popular member of the generalized linear regression models, which are a class of statistical models used for the analysis of binary systems (e.g., Hoffmann 2004). However, Zhang et al. (2013) assessed the applicability of different generalized linear models for liquefaction potential assessment, and found that the logistic regression model may not always be the optimal solution for constructing liquefaction models.

It is noted that in each case of the database with which Eq. (2.3) is derived, the *true* values of parameters X and CSR are unknown. Rather, nominal values are computed and these nominal values are used in the logistic regression analysis. Therefore, when Eq. (2.3) is applied to a future case, the nominal values of parameters X and CSR must first be determined and then the liquefaction probability is evaluated. Obtaining the nominal

values is part of the traditional deterministic approach, and thus, it requires little additional effort.

Bayesian Mapping Method

Recognizing that the *true* values of parameters X and CSR are unknown (and thus, the *true* factor of safety F_S of a given case history is unknowable), Juang et al. (2002) analyzed the case histories data by their nominal values. By examining the distributions of the nominal factor of safety (F_S) in the group of liquefaction cases and the group of non-liquefaction cases, respectively, Juang et al. (2002) established a mapping function that relates F_S to the probability of liquefaction (P_L) based on Bayes' theorem (Juang et al. 1999 & 2000):

$$P_L = P(L \mid F_S) = \frac{P(F_S \mid L)P(L)}{P(F_S \mid L)P(L) + P(F_S \mid NL)P(NL)} \tag{2.4}$$

where $P(L)$ and $P(NL)$ are the prior probabilities of liquefaction and no-liquefaction, respectively; and $P(F_S|L)$ and $P(F_S|NL)$ are the probabilities of a given case with known F_S value for the liquefied group and the non-liquefied group, respectively. Juang et al. (2002) assumed that the prior probabilities of a given case are the same [i.e., $P(L) = P(NL) = 0.5$], as they argued that when there was no information to suggest otherwise, the assumption of $P(L) = P(NL)$ was assured by the principle of maximum entropy. Thus, the Bayesian mapping function can be reduced into the form of $P_L = f(F_S)$, where f is an empirical function derived from the database. An example of such equation is expressed as (Ku et al. 2012):

$$P_L = \frac{1}{1+(F_S/0.9)^6} \tag{2.5}$$

where F_S is the nominal factor of safety obtained for a given soil using the Robertson and Wride (1998) method with CPT data. When applying Eq. (2.5) to a future case, the nominal input parameters should be used to compute the nominal F_S, the same procedure to perform a deterministic analysis of liquefaction potential. The nominal F_S is then entered Eq. (2.5) for an estimate of the liquefaction probability. The implication is that on average, the uncertainty level in a future case is approximately the same as the level of uncertainty of the cases in the calibration database. The reader is referred to Ku et al. (2012) for applications to future cases.

In recent years, substantial efforts have been made in the process of model development and model calibration to address the uncertainties in the case histories in the calibration database. To this end, Bayes' theorem has been proven as a powerful tool to consider different sources of uncertainties in a consistent way.

Bayesian Regression Method

Cetin et al. (2004) developed a probabilistic model using the principle of maximum likelihood with an updated database of case histories. The work of Cetin et al. (2004) was comprehensive and had several unique features, for example, use of the maximum likelihood method for the first time in liquefaction data analysis, a specific treatment of sampling bias in the database, and a complete treatment of model and parameter uncertainties. A simplified form of their probabilistic model could be expressed as:

$$P_L = \Phi\left[-\begin{pmatrix} N_{1,60}(1+0.004\cdot FC) - 13.32\ln(CSR) - 29.53\ln(M_w) \\ -3.7\ln\left(\sigma_v' \ / \ p_a\right) + 0.05FC + 16.85 \end{pmatrix} / 2.70\right] \quad (2.6)$$

where Φ is the cumulative standard normal distribution function; FC is fines content; $N_{1,60}$ is the corrected SPT blow count; CSR is the cyclic stress ratio *without* adjustment to the reference state of M_w = 7.5 and σ_v' = 100 kPa, where M_w is the moment magnitude and σ_v' is the effective stress; and p_a is the reference pressure (1 atm ≈ 101 kPa). It is noted that the probabilistic model as expressed in Eq. (2.6) by-passed the safety factor F_S in its development process and has no obvious relation with F_S. In fact, they established a deterministic model (limit state) that is simply an equivalence of Eq. (2.6) with P_L = 0.15.

Because input parameters were treated as random variables in the model development by Cetin et al. (2004), the parameters FC, $N_{1,60}$, CSR, M_w, and σ_v' in Eq. (2.6) are random variables. To evaluate the liquefaction probability P_L for a future case using Eq. (2.6), one has to characterize these input parameters statistically first, and then perform a Monte Carlo simulation to obtain the distribution of P_L (and to determine its mean and standard deviation as desired).

Following the Bayesian method by Cetin et al. (2004) in the development of new liquefaction models, Moss et al. (2006) also developed a similar model for evaluating the liquefaction probability using CPT. Based on re-assessed databases of case histories, Boulanger and Idriss (2012) developed liquefaction potential models using SPT, and later further developed liquefaction potential models using CPT (Boulanger and Idriss 2015). While these latest developments basically followed the one developed by Cetin et al. (2006), a significant exception was that Boulanger and Idriss (2012 & 2015) assigned the

coefficients of variation to key input parameters such as $N_{1,60}$ and CSR, rather than developing site-specific estimations of the magnitudes and distributions of these uncertainties for each case history. Similar to the probabilistic model by Cetin et al. (2004), input parameters are treated as a random variable by Boulanger and Idriss (2012 & 2015) in their model development, thus, the parameters CSR and CRR are random variables, and so is the F_S. Therefore, to evaluate the liquefaction probability for a future case, one has to characterize the input parameters statistically first, and then perform a Monte Carlo simulation to obtain the distribution of the liquefaction probability.

The reader is referred to Juang et al. (2013) for comparison of these probabilistic models that were developed using the Bayesian methods.

Random Field Modeling for Liquefaction Hazard Mapping

The location-specific evaluation of the liquefaction potential has been reviewed previously. This section focuses on the areal or regional evaluation of liquefaction potential, which is essential for liquefaction hazard zoning and mitigation. As the number of test data in a given geotechnical investigation is usually limited, soil properties at a given site may not be characterized adequately. How to map the liquefaction potential in an areal or regional scale based on the limited test data is thus an urgent issue facing the geotechnical engineer.

The early studies of regional liquefaction hazard mapping focused on the occurrence of liquefaction and relied upon the correlations that relate surficial geology to liquefaction susceptibility and potential (Youd and Perkins 1978; Knudsen et al. 2000;

Witter et al. 2006). Later, use of supplementary data such as hydrological and geotechnical data (Holzer et al. 2006a&b; Brankman and Baise 2008; Hayati and Andrus 2008; Heidari and Andrus 2010&2012) or geomorphological data (Papathanassiou et al. 2017) along with the surficial geology data in characterizing and mapping the liquefaction hazards has been reported. In these studies, the liquefaction hazard level (quantified in terms of either liquefaction susceptibility or liquefaction potential) was often assumed to be constant within each surficial geologic unit. This assumption, though convenient for traditional geological mapping, ignores the inherent spatial variability of soil properties and therefore may hinder the accuracy of the generated liquefaction hazard maps (Juang et al, 2018).

In the last two decades, random field theory has been applied to assessing and mapping liquefaction potential or hazards over an area or region (Elkateb et al, 2003; Baise et al., 2006; Lenz and Baise, 2007; Chen et al., 2015; Wang et al, 2017; Juang et al., 2017b; Bong and Stuedlein 2017&2018). The random field model method can consider the spatial variability and dependency, as well as associated uncertainties. The spatial variability and dependence of soil properties has long been recognized: soil properties measured at one location are more similar to those at neighboring locations than those further away (Fenton and Vanmarcke 1998; Vanmarcke, 2010). By drawing multiple random samples, the overall characteristics of the spatial variability and dependence, and the uncertainties involved, can be mathematically modeled by random field models.

Using the random field theories with the known properties (from the actual tests) at limited test locations, the soil properties at unsampled locations can be learned through the knowledge of the spatial variability and dependence of soil properties, and thus the soil properties in a given area with limited test data can be characterized statistically. The gained knowledge of the soil properties in an area allows an areal evaluation and mapping of the liquefaction potential.

Ground Improvement Methods for Liquefaction Hazard Mitigation

In the last four decades, there has been a steady trend toward the use of ground improvement as a countermeasure against the hazard of liquefaction. The ground improvement techniques, such as densification, solidification (e.g., cementation), vibro-compaction, explosive compaction, deep soil mixing, deep dynamic compaction, permeation grouting, jet grouting, pile-pinning and gravel drains or stone columns, have been used in engineering practice to reduce the risk of liquefaction and associated ground deformation (Asgari et al., 2013; Lukas 1995; Han 2015; Shen et al. 2018). The effectiveness of ground improvement in liquefaction mitigation is well observed in the past earthquakes as the sites with ground improvement suffer less ground deformation and subsidence than adjacent, unimproved areas (Mitchell et al., 1991; Dise et al., 1994; Hausler and Sitar 2001; Lee et al., 2001; Martin et al., 2002; Olgun 2003; Hausler and Koelling, 2004).

Dynamic compaction (DC), as one of the ground improvement methods, has been successfully used to strengthen many types of weak ground deposits, including

hydraulically placed silty sands, clay or silty clay fills, miscellaneous fills, sanitary landfills, mine spoils, rockfills, sinkholes, and collapsible soils (Ghassemi et al., 2010; Lukas 1995). Because of its cost efficiency, simplicity and significant reinforcement effect, DC has been extensively used worldwide for soil treatment on a large scale. DC consists of the repeated dropping of heavy weight (tamper) in a pre-determined pattern on the weak ground that needs to be densified. After release, the free-falling heavy tamper builds up energy. The powerful stress wave generated during the impact process destroys the skeleton of the soil grain, decreases the porosity, and effectively compacts the ground (Feng et al., 2015). DC usually progresses in phases. In the first phase (high energy phase), large masses are dropped from greater heights repeatedly. The mass of tamper generally ranges from 5 to 30 tons, drop height ranges from 12 to 30 m, and often between 7 and 15 drops on each compaction point (Mayne et al., 1984; Lukas 1995). During this stage, deep soil layers are usually affected up to the depth of 15 m. Completion of the initial phase is usually followed by a low energy phase, called ‘‘ironing”, intended to densify the surficial layers in the upper 1.5 m (Ghassemi et al., 2010; Mayne et al., 1984).

DC reduces the risk of liquefaction hazards by densifying the soil thus increasing liquefaction resistance. In this dissertation work, the effect of DC in the mitigation of liquefaction is studied in detail through a case study.

CHAPTER III[1]

PREDICTING LIQUEFACTION PROBABILITY BASED ON SHEAR WAVE VELOCITY: AN UPDATE

Introduction

Liquefaction is one of the most common geotechnical hazards triggered by earthquakes. It may cause lateral spreading, surface settlements, and sand boiling, which, in turn, may damage structures and infrastructures and induce losses of life. Among methods for soil liquefaction potential evaluation, simplified methods based on in situ tests, such as standard penetration test (SPT), cone penetration test (CPT), and shear wave velocity (V_s) test, are preferred in geotechnical engineering practices as it is usually difficult and expensive to sample and conduct dynamic testing. With the simplified methods, the liquefaction potential of soil is usually expressed as a factor of safety F_S, which is defined as the ratio of cyclic resistance ratio (CRR) over the cyclic stress ratio (CSR). The soil is said to be liquefied if $F_S \leq 1$ and be non-liquefied if $F_S > 1$. The liquefaction resistance chart, with a horizontal axis to indicate the strength of soil and a vertical axis to indicate the shaking level in terms of CSR, is usually used in a deterministic approach. In such a chart, a single boundary line is used to separate

[1]A similar form of this chapter is published as: Shen, M., Chen, Q., Zhang, J., Gong, W., & Juang, C. H. (2016). Predicting liquefaction probability based on shear wave velocity: an update. Bulletin of Engineering Geology and the Environment, 75(3), 1199-1214, doi:10.1007/s10064-016-0880-8.

liquefied and non-liquefied case histories (e.g., Seed & Idriss 1971, Robertson & Wride 1998, Youd et al. 2001, and Andrus & Stoke 2000).

Due to the uncertainties in soil parameters and seismic loading, it may be desirable to represent the liquefaction potential in terms of liquefaction probability (P_L) rather than safety factor F_S. A number of probabilistic models have been developed for liquefaction potential evaluation using the simplified methods (SPT, CPT and V_s test) derived from the corresponding database (e.g., Christian & Swiger 1975, Liao et al. 1988, Toprak et al. 1999, Juang et al. 2001 & 2012a, Cetin et al. 2004, Ku et al. 2012, and Boulanger & Idriss 2012). Among these models, the logistic regression is widely used for developing the probabilistic contours, which are a set of curves showing liquefaction probabilities (conditional probabilities) in a liquefaction resistance chart. Although probabilistic models based on logistic regression are widely used, there are several other equally competitive models, in the form of generalized linear models (GLMs). GLMs have wide applications in geology, soil science, hydrology, agronomy and ecology (e.g., Gotway & Stroup 1997, Gessler et al. 1995, Lane 2002, and McKenzie & Ryan 1999). The widely used logistic regression in geotechnical engineering is simply one example of the GLMs. By treating the liquefaction potential of a soil deposit during an earthquake as a binary system (i.e., whether or not liquefaction occurs), GLMs can be applied to develop the optimal probabilistic model for liquefaction potential evaluation. It should be of interest to check different model assumptions when developing an empirical model based on a given database such that an optimal model for liquefaction prediction can be attained.

This chapter focuses on the V_s-based simplified methods. The advantages of V_s test include: (1) V_s test can be conducted in gravelly soils and sites where the SPT and CPT are unreliable; (2) V_s test can be also conducted on laboratory samples so that comparison can be made between laboratory test and field test; (3) V_s is an engineering property that can be related to small-strain shear modulus directly (Andrus et al. 1999). In particular, Andrus and Stokoe (2000) pioneered the application of V_s test for liquefaction potential evaluation. They assembled a database with 225 case histories (Andrus et al. 1999) which is widely used to develop the liquefaction model. Generally, the amount of statistical uncertainty involved in liquefaction models may be decreased, as more data become available. Therefore, it is quite necessary to collect new case histories and update the liquefaction models when possible. Between 2010 and 2011, the Canterbury region of New Zealand was shocked by four major earthquake events. Extensive liquefaction phenomena were observed, which provides a good chance to update our knowledge towards the potential of soil liquefaction in a given seismic event. The objective of this chapter is thus two folded: (1) to compile new case histories relating shear wave velocity with soil liquefaction observation; and (2) to assess and update the existing probabilistic models for liquefaction potential evaluation. The structure of this chapter is as follows. First, develop and compare generalized linear models using the adopted database. Then, the new case histories compiled in this study from 22 February 2011 Canterbury earthquake are used to evaluate the performance of developed models. Finally, the models based on the existing database are updated based on the combined database and

the optimal model is recommended for liquefaction potential evaluation using the shear wave velocity measurements.

New Liquefaction Cases from the 22 February 2011 Canterbury earthquake and the adopted databases

Between 2010 and 2011, the Canterbury region of New Zealand experienced a total of four major earthquake events and numerous small aftershocks. The four main earthquakes were on 4 September 2010, 22 February 2011, 13 June 2011 and 23 December 2011. The detailed information of these four major earthquakes is summarized in Table 3.1 (Tonkin & Taylor 2013).

Table 3.1: Summary of Canterbury earthquakes in 2010 and 2011 (Tonkin & Taylor 2013).

Earthquake	NZ Standard Date	M_w	Epicenter	
			Depth (km)	Location
Darfield earthquake (Greendale)	Sep. 4th 2010	7.1	10	35 km W of Christchurch
Christchurch 1 Earthquake (Lyttelton)	Feb. 22nd 2011	6.2	5	10 km SE of Christchurch
Christchurch 2 Earthquake (Sumner, 2 events)	Jun. 13th 2011	6.2	6	10 km SE of Christchurch
			9	10 km SE of Christchurch
Christchurch 3 Earthquake (New Brighton, 2 events)	Dec. 23rd 2011	6.1	8	20 km E of Christchurch
			6	10 km E of Christchurch

These earthquakes caused widespread liquefaction, lateral spreading, and ground settlement, which brought extensive damages to residential dwellings and infrastructures, especially in Christchurch (Cubrinovski et al. 2011). In particular, the 22 February 2011

earthquake was the most damaging event due to its shallow focal depth and the close proximity of its rupture plane to Christchurch (Green et al. 2014, Orense et al. 2011).

Ground Motions of the 22 February 2011 Earthquake

New Zealand is passed through by the active Pacific-Australian Plate boundary, which produces earthquakes, volcanoes, steep terrain and active deformation. As an earthquake-prone nation, New Zealand is well monitored by a dense network of geophysical instruments and automated software applications, as evidenced by GeoNet project (http://geonet.org.nz*)*.

In order to calculate the cyclic stress ratio CSR, the Peak Ground Acceleration (PGA) should be evaluated at each subject location. Using the recorded strong motion data of seismographs in the Canterbury region, the conditional PGA distributions at the case history sites were computed using the spatial PGA contour maps by Bradley & Hughes (2012), which is shown in Figure 3.1. For locations between median contours, the conditional PGA may be obtained by linear interpolation (Khoshnevisan et al. 2015).

Figure 3.1: Contour map of the computed median of conditional PGAs for the 22 February 2011 earthquake (Bradly & Hughes 2012). Inset is a zoom-in view of the studied area showing contours of PGAs and locations of CPT data.

Site Investigation Data in the Canterbury Region

After the September 4, 2010 earthquake, the Earthquake Commission (EQC) of New Zealand engaged Tonkin & Taylor (T&T) to undertake geotechnical investigations, which comprised CPT, machine boreholes, geophysical testing, groundwater observations, laboratory testing, and survey monitoring and environment boreholes. The staged land reports of the investigations can be downloaded from the website of EQC (http://www.eqc.govt.nz). Moreover, the data from geotechnical site investigations in the Canterbury region is enlarged by the delivery agents and clients who are involved in the geotechnical work there.

The compiled data are available in the online database, Canterbury Geotechnical Database (CGD, https://canterburygeotechnicaldatabase.projectorbit.com).

The shear wave velocity dataset studied in this chapter is based on the results of active Multichannel Analysis of Surface Waves (MASW) test, seismic CPT test, and borehole profiles. The geophysical MASW tests are used to provide shear wave velocity

profiles with depth (the average depth is around 13.0 m below the ground level). The CPT profiles are used for I_c calculation to obtain clean sand equivalent V_s. Moreover, the representative samples from borehole are collected for laboratory testing for index properties. In this study, only locations with complete V_s, CPT, and borehole profiles are selected. All the CPT locations and active MASW lines of the cases examined are shown in Figure 3.2.

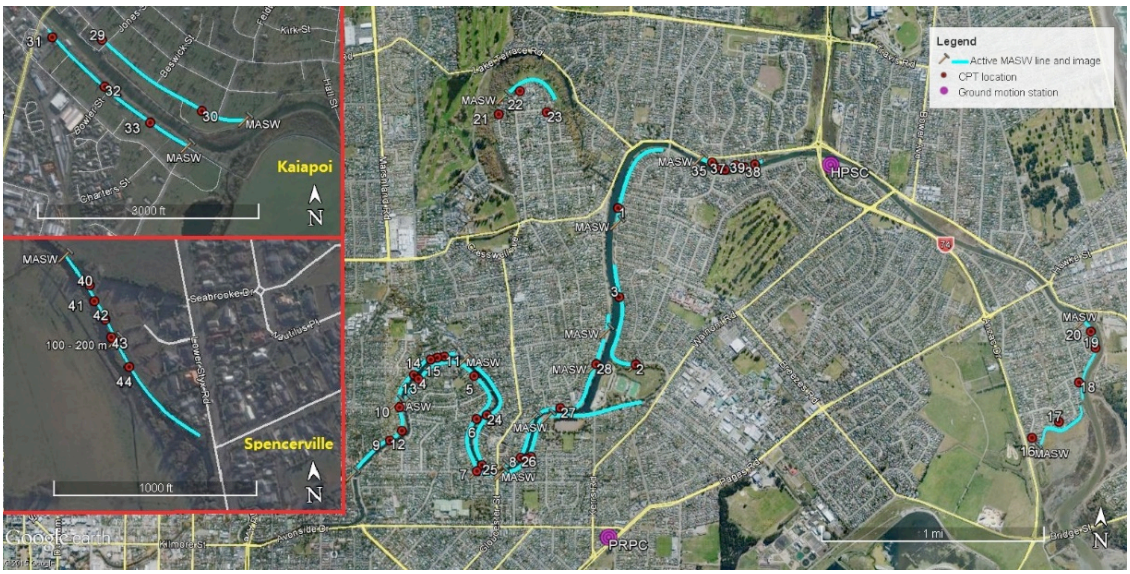

Figure 3.2: CPT locations and active MASW lines. Insets on the left are two additional studied regions not included in the larger area map on the right.

To illustrate how to obtain shear wave value at each location, CPT-116 in Figure 3.3(a) is used as an example. As shown in Figure 3.3(a), the active MASW lines are very close to the most CPT test locations. In A-A' section, the shear wave velocity profile of the point, which is along the MASW 200m-300m line and nearest to the location of CPT-116, is used to represent the shear wave velocity at CPT-116. Then, the shear wave velocity profile with depth can be read from color contour shown in Figure 3.3(b) where CPT-116 is at the chainage of 248 m. When determining the V_s value at the critical layer,

the critical value is taken as the average V_s over a 0.5 m interval to reduce potential biases (Zhou et al. 2012).

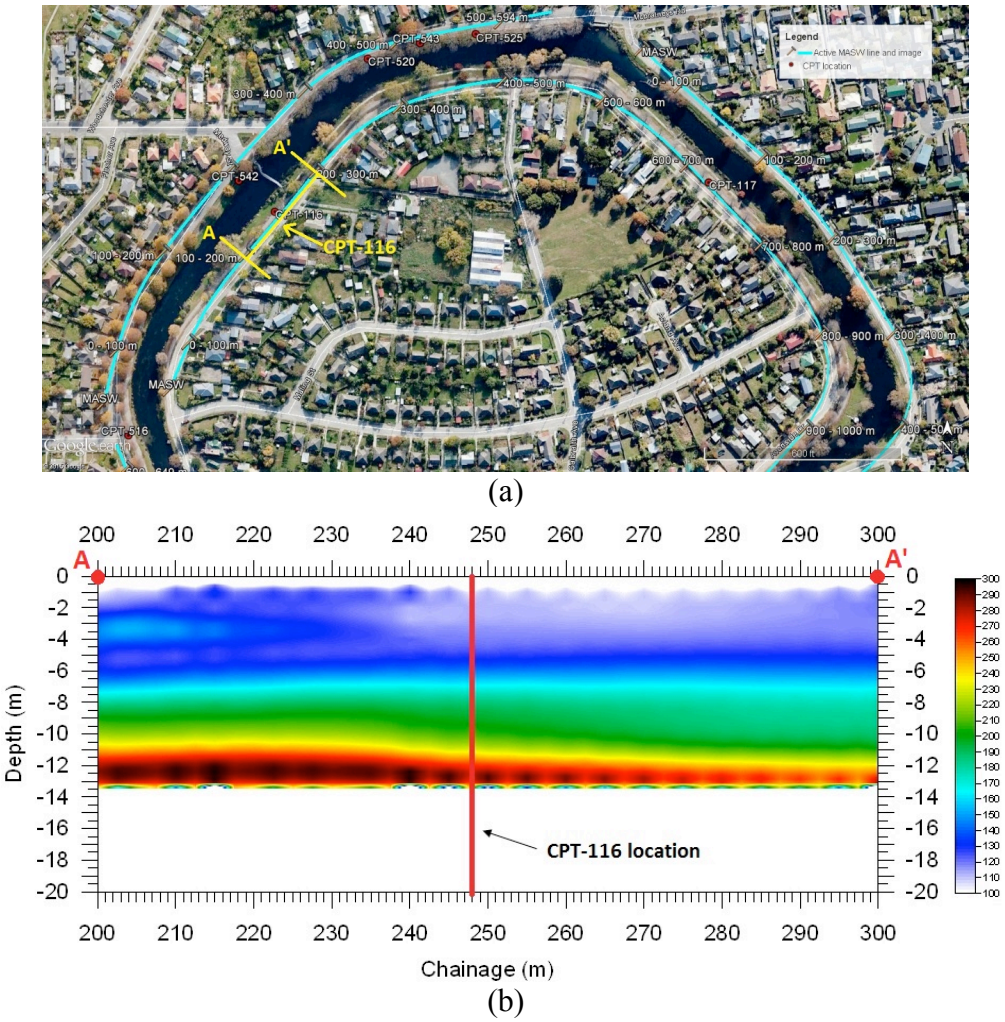

(a)

(b)

Figure 3.3: Determination of shear wave velocity for CPT-116; (a) Location of CPT-116 and nearby MASW lines; (b) Color contour of shear wave velocity along the 200-300 m MASW line.

The laboratory tests include the particle size distribution and the fines content (wet sieve). The fines content (*FC*) of the critical layer is required in the cyclic resistance ratio ($CRR_{7.5}$) calculation to adjust the measured shear wave velocity to a clean sand equivalence. For locations without fines content tests, *FC* is estimated using the site-

specific I_c-FC correlation relationship proposed by Green et al. (2014). The I_c value is calculated using the CPT data and the empirical correlation proposed by Robertson and Wride (1998).

Using the information described previously, the case histories from the 22 February 2011 Canterbury earthquake are summarized in Table 3.2. The table consists of 45 cases in total, among which 36 cases are serious liquefied and 9 cases are marginal liquefied.

Table 3.2: Summary information of case histories from the 22 February 2011 Canterbury earthquake.

Site	No.	CPT Database No.	Test Date	Ground Water Table	Median depth	Upper bound	Total stress	Effective stress	Field Test Data				Calculated Data		2011.02.22 Earthquake Mw=6.3		
				GWT	d_m	d_u	σ_v	σ_v'	q_c	f_s	V_s	FC[1]	I_c	$V_{s1,cs}$	a_{max}	$CSR_{7.5}$	Liq.[2]
				m	m	m	(kPa)	(kPa)	(Mpa)	(Mpa)	(m/s)	(%)		(m/s)	(g)		
Avondale	1	CPT-37	11/19/2010	2.1	6.3	4.5	116.4	75.7	6.69	0.043	154	14	1.90	167	0.37	0.227	2
	2	CPT-855	11/9/2010	2.4	5.5	2.5	100.6	70.7	6.59	0.030	155	5	1.81	169	0.44	0.250	2
	3	CPT-857	11/9/2010	2.4	5.1	3.4	93.0	67.0	7.18	0.035	142	7	1.78	157	0.41	0.230	2
Avonside	4	CPT-116	12/1/2010	1.5	3.8	2.0	69.5	47.4	9.28	0.048	133	41	1.64	166	0.43	0.253	2
	5	CPT-117	11/16/2010	1.3	3.3	1.5	60.2	41.1	4.49	0.026	124	21	1.91	158	0.44	0.261	2
	6	CPT-111	11/18/2010	1.3	3.3	2.5	60.2	41.1	6.91	0.045	136	5	1.77	170	0.46	0.275	2
	7	CPT-135	7/18/2010	2.1	6.0	5.5	111.6	73.4	17.54	0.057	195	11	1.37	215	0.49	0.298	2
	8	CPT-136	7/18/2011	2.0	8.5	7.0	159.5	95.8	13.87	0.082	204	≈10*	1.66	209	0.51	0.329	2
Richmond	9	CPT-540	12/7/2010	2.0	5.2	4.4	96.4	65.1	7.41	0.036	154	3	1.76	171	0.45	0.267	2
	10	CPT-516	11/22/2010	2.4	3.5	3.0	63.4	52.6	6.14	0.037	138	28*	1.85	167	0.44	0.214	2
	11	CPT-525	11/5/2010	1.2	3.6	2.4	66.1	43.0	5.28	0.019	130	1	1.75	160	0.42	0.262	2
	12	CPT-514	11/22/2010	2.0	3.0	2.0	54.4	44.6	2.30	0.010	124	≤ 5*	2.13	152	0.45	0.223	2
	13	CPT-542	12/7/2010	1.5	4.0	2.4	74.2	49.7	7.40	0.034	137	≤ 5*	1.70	163	0.43	0.256	2
	14	CPT-520	1/20/2010	1.1	4.5	2.0	84.4	51.1	6.54	0.023	137	≤ 5*	1.70	162	0.42	0.279	2
	15	CPT-543	12/7/2010	1.0	3.8	2.4	71.1	43.7	7.39	0.033	141	≤ 5*	1.67	173	0.42	0.277	2
Bexley-aranui	16	CPT-155	11/3/2010	1.5	6.1	3.2	114.4	69.3	3.80	0.024	132	10	2.10	145	0.57	0.374	2
	17	CPT-176	9/30/2010	1.9	3.5	2.0	64.1	48.4	4.97	0.013	118	12	1.74	143	0.57	0.306	2
	18	CPT-173	9/30/2010	1.1	4.5	2.0	84.4	51.1	6.53	0.023	126	20	1.70	152	0.56	0.374	2
	19	CPT-178	11/24/2010	1.5	5.5	3.4	101.9	63.2	3.66	0.026	126	17	2.12	143	0.56	0.361	2
	20	CPT-170	11/24/2010	1.5	3.4	2.6	62.8	44.1	2.81	0.026	122	17	2.21	151	0.56	0.320	2
Burwood	21	CPT-277	11/10/2010	1.1	3.0	1.5	55.7	37.1	2.87	0.013	113	13	2.01	146	0.34	0.209	2
	22	CPT-280	11/9/2010	1.6	4.0	1.0	74.1	50.6	4.07	0.017	138	3	1.92	164	0.34	0.201	2

	23	CPT-279	11/8/2010	1.7	3.8	1.7	69.2	49.1	3.68	0.016	114	1	1.96	136	0.35	0.197	2
Dallington	24	CPT-1088	11/17/2010	2.1	9.5	8.0	178.5	105.9	13.60	0.103	187	2	1.75	184	0.47	0.300	2
Lower	25	CPT-1085	11/19/2010	0.9	4.4	2.6	82.8	48.5	3.74	0.020	120	4	1.99	144	0.49	0.338	2
	26	CPT-1086	11/18/2010	1.5	4.0	2.6	74.2	49.7	3.57	0.014	139	16	1.96	168	0.51	0.304	2
	27	CPT-1092	11/18/2010	2.4	4.8	4.0	87.2	64.2	12.21	0.062	134	5	1.59	149	0.48	0.262	2
	28	CPT-1098	11/17/2010	2.4	7.8	6.0	144.6	92.1	14.57	0.076	216	3	1.60	221	0.45	0.279	2
Kaiapoi	29	CPT-1267	11/10/2010	1.4	4.5	3.2	83.0	53.1	7.14	0.029	115	2	1.70	135	0.18	0.116	1
North	30	CPT-1293	11/10/2010	1.5	4.0	3.5	73.3	49.3	5.55	0.028	125	20	1.83	152	0.18	0.109	2
Kaiapoi	31	CPT-1316	11/11/2010	2.0	5.0	3.5	92.6	63.2	4.19	0.030	130	39*	2.06	151	0.18	0.107	1
South	32	CPT-1315	11/10/2010	2.1	3.5	2.0	63.8	50.1	4.76	0.031	129	6	1.95	154	0.19	0.096	1
	33	CPT-1344	12/8/2010	3.3	8.3	6.5	152.8	104.3	7.53	0.035	231	6	1.84	230	0.19	0.108	1
New	34	CPT-300	12/3/2010	2.0	6.3	3.6	117.5	75.3	5.91	0.029	148	30*	1.89	163	0.35	0.213	2
Brighton	35	CPT-317	12/9/2010	0.7	4.0	2.6	75.4	43.1	5.65	0.026	114	≤ 5*	1.78	141	0.35	0.244	2
	36	CPT-318	12/9/2010	0.5	4.4	2.4	83.3	45.1	4.83	0.022	122	≤ 5*	1.85	149	0.34	0.254	2
	37	CPT-301	12/3/2010	2.7	4.8	2.7	86.8	66.7	5.19	0.019	125	≤ 5*	1.85	138	0.34	0.177	2
	38	CPT-319	12/9/2010	0.7	4.3	2.5	80.2	45.4	4.44	0.021	119	≤ 5*	1.89	145	0.34	0.238	2
	39	CPT-320	12/9/2010	0.8	5.2	2.7	98.2	55.1	5.10	0.023	167	≤ 5*	1.86	194	0.33	0.235	2
Spencerville	40	CPT-667	10/28/2010	0.9	3.7	3.0	69.4	41.9	5.35	0.021	127	≤ 5*	1.76	157	0.25	0.164	1
	41	CPT-668	10/28/2010	1.6	3.9	3.0	71.2	49.2	6.80	0.017	115	4	1.61	137	0.25	0.144	1
	42	CPT-669	10/28/2010	1.5	3.6	2.7	65.6	45.5	5.64	0.028	130	26*	1.81	162	0.25	0.144	1
	43	CPT-670	10/28/2010	1.1	3.2	1.1	59.5	39.0	4.93	0.022	136	1	1.80	172	0.25	0.154	1
	44	CPT-671	10/28/2010	2.0	3.1	2.2	56.3	45.5	6.72	0.042	133	26*	1.80	165	0.25	0.125	1
Wainoni	45	CPT-846	11/15/2010	2.0	5.3	4.0	97.4	65.5	13.66	0.072	182	≈10*	1.56	204	0.51	0.302	2

Notes:
[1] The *FC* value with * mark was estimated using site specific I_c-*FC* correlation proposed by Green et al. (2014);
[2] Liq.=0 means non-liquefaction; Liq.=1 means marginal liquefaction; Liq.=2 means serious liquefaction.

Databases and Review of Deterministic Method

Two databases will be used in this study according to different studied purposes. The first database is assembled by Andrus et al. (1999), denoted as Andrus 1999 database herein. It consists of 105 liquefied cases and 120 non-liquefied cases for a total of 225 cases. It includes the shear wave velocity measurements from over 70 sites and soil liquefaction data from 26 earthquakes, as summarized in Table 3.3. The shear wave velocity tests along with liquefaction observations, acceleration data from ground motion stations, and results of laboratory tests were used to determine the cyclic resistance ratio $CRR_{7.5}$ and cyclic stress ratio $CSR_{7.5}$. The deterministic approach proposed by Andrus (2000) is summarized in Appendix A.

The second database is called combined database here, which is the Andrus 1999 database supplemented with the 36 serious liquefied case histories from the 22 February 2011 Canterbury earthquake for a total of 261 cases. The 9 marginal liquefied cases are not included in the combined database to reduce the data uncertainty.

The Andrus 1999 database is adopted to develop the optimal model using the GLMs. The combined database is used to update the proposed model.

Table 3.3: Ranges of measurements of the Andrus 1999 database.

Earthquake	In Situ Ttest Type[1]	Number of Cases		Average Depth	a_{max}	M_w	V_s	FC
		Liq.	Non-liq.	(m)	(g)		(m/s)	(%)
1906 San Francisco, California	Xhole	8	4	4.2-9.9	0.32-0.36	7.7	131-200	<5-44
1957 Daly City, California	SASW	0	5	3.5-7.9	0.11	5.3	105-220	2-12
1979 Imperial Valley, California	Xhole & SASW	4	7	3-4.7	0.12-0.51	6.5	90-173	10-75
1981 Westmorland, California	Xhole & SASW	6	5	3-4.7	0.03-0.36	5.9	90-173	10-75
1983 Borah Peak, Idaho	Xhole & SASW	15	3	1.9-3.7	0.23-0.46	6.9	94-274	<5-6
1987 Elmore Ranch, California	Xhole & SASW	0	11	3-4.7	0.03-0.24	5.9	90-173	10-75
1987 Superstition Hills, California	Xhole & SASW	3	8	3-4.7	0.18-0.21	6.5	90-173	10-75
1989 Loma Prieta, California	Xhole, SASW & SCPT	42	25	2.3-9.9	0.13-0.42	7	91-220	1-57
1994 Northridge, California	SCPT	3	0	5.4-5.6	0.51	6.7	129-160	~10
1975 Haicheng, China	Dhole	5	1	3-10.2	0.12	7.3	98-147	42-92
1985 Taiwan (event LSST2)	Xhole	0	4	5.3-6.1	0.05	5.3	127-156	50
1985 Taiwan (event LSST3)	Xhole	0	4	5.3-6.1	0.02	5.5	127-156	50
1986 Taiwan (event LSST4)	Xhole	0	4	5.3-6.1	0.22	6.6	127-156	50
1986 Taiwan (event LSST6)	Xhole	0	4	5.3-6.1	0.04	5.4	127-156	50
1986 Taiwan (event LSST7)	Xhole	0	4	5.3-6.1	0.18	6.6	127-156	50
1986 Taiwan (event LSST8)	Xhole	0	4	5.3-6.1	0.04	6.2	127-156	50
1986 Taiwan (event LSST12)	Xhole	0	4	5.3-6.1	0.18	6.2	127-156	50
1986 Taiwan (event LSST13)	Xhole	0	4	5.3-6.1	0.05	6.2	127-156	50
1986 Taiwan (event LSST16)	Xhole	0	4	5.3-6.1	0.14	7.6	127-156	50
1964 Niigata, Japan	SASW	3	1	3.2-6.2	011-0.16	7.5	112-162	<5
1980 Mid-Chiba, Japan	Dhole	0	2	6.1-14.8	0.08	5.9	155-195	25-30
1985 Chiba-Ibaragi, Japan	Dhole	0	2	6.1-14.8	0.05	6	155-195	20-35
1987 Chiba0Toho-Oki, Japan	Dhole	0	1	9	0.1	6.5	150	15

1993 Kushiro-Oki, Japan	Susp.	2	0	4.2-4.5	0.41	8.3	135-152	5~7
1993 Hokkaido-Nansei-Oki, Japan	Dhole & Susp.	3	1	2.0-7.0	0.15-0.19	8.3	74-143	<5-54
1995 Hyogoken Nanbu, Japan	Dhole & Susp.	11	8	3.3-15	0.12-0.65	6.9	110-214	2-18

Notes:
[1] In Situ Test Type: Xhole = Crosshole Seismic Test; Dhole = Downhole Seismic Test; SCPT = Seismic Cone Penetration Test; SASW = Spectral Analysis of Surface Wave Test; Susp. = Suspension Logger Test

Prediction of Soil Liquefaction Based on GLMS

Generalized Linear Models (GLMs)

Denote the independent variable as $\mathbf{X} = (x_1, x_2, \ldots, x_i, \ldots, x_p)$, the response of n independent observations as $\mathbf{Y} = (y_1, y_2, \ldots, y_i, \ldots, y_n)$ with expectation of each observation $\mu_i = \mathrm{E}(y_i)$. The generalized linear model usually consists of three components, i.e., a random component, a linear predictor and a link function (Fox 2015, Gelman et al. 1995). The link function $g(\cdot)$ is a link to relate the expectation of the response variable μ_i to the linear predictor η_i as

$$\eta_i = g(\mu_i) \tag{3.1}$$

where the linear predictor η_i is a linear combination of independent variables $\mathbf{X}$. The linear combination of $V_{s1,\,cs}$ and $\ln(\mathrm{CSR}_{7.5})$ used in Juang et al. (2002) is adopted here as the independent variables and η_i is therefore given as

$$\eta_i = b_0 + b_1 x_{i1} + b_2 x_{i2} + \ldots + b_p x_{ip} = b_0 + b_1 (V_{s1,cs})_i + b_2 \ln[(CSR_{7.5})_i] \tag{3.2}$$

The effect of linear predictor as defined in Eq. (3.2) has been investigated by Juang et al. (2002), therefore it is not considered here. Rather, the effect of link functions on liquefaction potential evaluation will be explicitly considered in this chapter. The commonly used link functions and their inverse functions are listed in Table 3.4 (Fox 2015).

Table 3.4: Common link functions and their inverses (Fox 2015).

No.	Model	$\eta_i = g(\mu_i)$	$\mu_i = g^{-1}(\eta_i)$
1	Identity	μ_i	η_i
2	Log	$\ln \mu_i$	$\exp(\eta_i)$
3	Inverse	μ_i^{-1}	η_i^{-1}
4	Inverse-square	μ_i^{-2}	$\eta_i^{-1/2}$
5	Square-root	$\mu_i^{-1/2}$	η_i^{2}
6	Logit (logistic)	$\ln \frac{\mu_i}{1-\mu_i}$	$\frac{1}{1+\exp(-\eta_i)}$
7	Probit	$\Phi^{-1}(\mu_i)$	$\Phi\ (\eta_i)$
8	Log-log	$-\ln[-\ln(\mu_i)]$	$\exp[-\exp(-\eta_i)]$
9	Complementary log-log	$\ln[-\ln(1-\mu_i)]$	$1-\exp[-\exp(\eta_i)]$

The last four link functions in Table 3.4, namely logit (logistic), probit (inverse of normal), log-log and complementary log-log (c-log-log), are commonly used for analysis of binary data and are adopted in this chapter.

For liquefaction potential evaluation considered herein, the response variable y_i can only have two possible values, i.e., 1 for liquefaction and 0 for non-liquefaction. The probability of y_i can be defined as

$$\text{Probability of } y_i = \begin{cases} P(y_i = 1) = P_{Li} & \text{for liquefied cases} \\ P(y_i = 0) = 1 - P_{Li} & \text{for non-liquefied cases} \end{cases} \tag{3.3}$$

Then, the expectation μ_i will be equal to the probability of liquefaction, P_{Li}, as

$$\mu_i = E(y_i) = 1 \times P_{Li} + 0 \times (1 - P_{Li}) = P_{Li} \tag{3.4}$$

Substituting Eq. (3.1) to Eq. (3.4), the probability of liquefaction P_{Li} is expressed as

$$P_{Li} = \mu_i = g^{-1}(\eta_i) = g^{-1}\{b_0 + b_1(V_{s1,cs})_i + b_2 \ln[(CSR_{7.5})_i]\} \tag{3.5}$$

With the Eq. (3.5), using logistic, probit, log-log and complementary log-log models listed in Table 3.4, the probabilistic models can be established and shown from Eq. (3.6) to Eq. (3.9).

Logistic:

$$P_L = \frac{1}{1+\exp\{-[b_0 + b_1 V_{s1,cs} + b_2 \ln(CSR_{7.5})]\}} \tag{3.6}$$

Probit:

$$P_L = \Phi\ [b_0 + b_1 V_{s1,cs} + b_2 \ln(CSR_{7.5})] \tag{3.7}$$

Log-log:

$$P_L = \exp\{-\exp[-(b_0 + b_1 V_{s1,cs} + b_2 \ln(CSR_{7.5}))]\} \tag{3.8}$$

C-log-log:

$$P_L = 1 - \exp\{-\exp[b_0 + b_1 V_{s1,cs} + b_2 \ln(CSR_{7.5})]\} \tag{3.9}$$

Maximum Likelihood Estimation Considering the Sampling Bias

Assume there are n_L liquefied cases and n_{NL} non-liquefied cases in a database. Denote $\theta = (b_0, b_1, b_2, \ldots, b_p)$ as the model parameters to be estimated, and $f(y_i|\theta)$ as the probability density function of $\mathbf{Y}$ given θ, which can be obtained from Eq. (3.5). Then, the likelihood function $l(\theta|\mathbf{Y})$, namely, the chance to observe Y given θ, is equal to the joint probability function as follows

$$l(\theta \mid \mathbf{Y}) = \prod_{i=1}^{n_L} f(y_i \mid \theta) \prod_{j=1}^{n_{NL}} [1 - f(y_j \mid \theta) = \prod_{i=1}^{n_L} g^{-1}(\eta_i \mid \theta) \prod_{j=1}^{n_{NL}} [1 - g^{-1}(\eta_j \mid \theta)] \tag{3.10}$$

The sampling bias effect should be considered for the database. The bias mainly comes from two aspects. One is that the earthquake investigators are more inclined to conduct in situ tests in liquefied sites than in non-liquefied sites. The field tests are not randomly distributed over the studied region. The other is that the observed data may be collected or excluded by prior researchers based on their own prior knowledge and experience or judgment on data quality. Therefore, the compiled database may be varied. Due to the perception that sampling bias exists in the database, a weighted likelihood function, widely used in previous studies (Cetin et al. 2002, Juang et al. 2009, Ku et al. 2012, and Boulanger & Idriss 2012), is adopted in this chapter for sampling bias correction.

$$l(\theta \mid \mathbf{Y}) = \left\langle \prod_{i=1}^{n_L} g^{-1}(\eta_i \mid \theta) \right\rangle^{w_L} \left\langle \prod_{j=1}^{n_{NL}} [1 - g^{-1}(\eta_j \mid \theta)] \right\rangle^{w_{NL}} \tag{3.11}$$

where w_L and w_{NL} are the weighting factors for liquefied cases and non-liquefied cases, respectively. Then, the model parameter θ can be determined by maximizing the value of likelihood function given by Eq. (3.11), or equivalently, the logarithmic of the likelihood function namely log-likelihood $L(\theta \mid \mathbf{Y})$ for computation efficiency.

A proper estimation of w_L and w_{NL} will decrease the sampling bias and reduce the uncertainties of model prediction. There are two approaches commonly used to obtain the weighting factors. The first approach is proposed by Ku et al. (2012), which is an intuitive approach. For the calculation of weighting factor w_L, firstly take the n_L^{th} root of the product $\prod_{i=1}^{n_L} g^{-1}(\eta_i \mid \theta)$ in Eq. (3.11) to find an "equivalent" likelihood case. While for

the calculation of w_{NL}, take n_{NL}^{th} root of the product $\prod_{j=1}^{n_{NL}}[1-g^{-1}(\eta_j \mid \theta)]$. Secondly, the $[(n_L+n_{NL})/2]^{th}$ power is taken for the products of liquefied and non-liquefied cases in last step to "raise" the likelihood back to the parity "structure". With these steps, equations for w_L and w_{NL} are obtained and expressed in Eq. (3.12) and Eq. (3.13) respectively.

$$w_L = \frac{n_L + n_{NL}}{2n_L} \tag{3.12}$$

$$w_{NL} = \frac{n_L + n_{NL}}{2n_{NL}} \tag{3.13}$$

For the Andrus 1999 database, n_L = 105 and n_{NL} = 120; thus, weighting factors are determined to be: w_L = 1.0714 and w_{NL} = 0.9375 (and thus, w_{NL}/w_L = 0.875).

The other approach is proposed by Cetin et al. (2002). The calculations of weighting factors are shown below:

$$w_L = Q_p / Q_s \tag{3.14}$$

$$w_{NL} = (1-Q_p)/(1-Q_s) \tag{3.15}$$

where Q_p is the true population proportion of liquefied cases in nature, and Q_s is sample population proportion of liquefied cases in studied database. It is easy to calculate Q_s for current database, which is 105/225 = 0.4667. However, it is impossible to know the Q_p value. Cetin et al. (2002) proposed two options to get the weighting factors. The first option is to consult with experts on the ratio of weighting factors (w_{NL}/w_L). Cetin et al. (2002) recommended the ratio of weighting factors should be between 1.0 and 3.0 and the most common range is 1.5 to 2.0. The second option is to conduct sophisticated Bayesian

updating analyses for w_{NL} and w_L values. Based on the SPT database, Cetin et al. (2002) obtained w_{NL} and w_L values of 1.2 and 0.8 (w_{NL}/w_L = 1.5), respectively. The values of weighting factors used for the current database will be discussed later.

Model Assessment Criteria

With the developed general linear models, model assessment criteria are used to determine the optimal model. There are several criteria available to assess model performance (Myung & Pitt 2004), including the Akaike information criterion (AIC) (Akaike 1973), the Bayesian information criterion (BIC) (Schwarz 1978), and the cross-validation (CV) (Stone 1974).

Assume there are r candidate models, which are denoted as M_1, M_2,…, M_m,…, M_r. The AIC, BIC and CV of the m^{th} model are defined as follow:

$$AIC_m = -2\ln l(\boldsymbol{\theta}^* \mid M_m, \mathbf{Y}) + 2k \tag{3.16}$$

$$BIC_m = -2\ln l(\boldsymbol{\theta}^* \mid M_m, \mathbf{Y}) + k\ln n \tag{3.17}$$

$$CV_m = -2\ln f[y_{\text{val}} \mid (\boldsymbol{\theta}^* \mid M_m, y_{\text{cal}})] \tag{3.18}$$

where $l(\boldsymbol{\theta}^* | M_m, \mathbf{Y})$ is likelihood function which gets its maximum value in point $\boldsymbol{\theta}^*$ given the model M_m and the observation $\mathbf{Y}$; k is the number of model parameters; n is the number of data points in the database; y_{cal} is the calibration samples and y_{val} is the validation samples; $f(\cdot)$ is the probability density function. A model with minimum value of AIC, BIC and CV is the preferred (optimal) model for each corresponding criterion.

The AIC and BIC are easy to calculate using Eqs. (3.16) & (3.17). The first term is the log-likelihood function, which represents the model fitting effect. The second term

represents the complexity of the model to be evaluated, which is a function of number of model parameters k for the AIC criterion, and of the sampling size n and k for the BIC criterion, respectively. The AIC and BIC criteria are easy to calculate but they do not consider the specific functional form of the probabilistic models. The CV is able to account for the functional form, e.g., the probabilistic models Eqs. (3.6) - (3.9).

For the CV criterion (Myung & Pitt 2004), the database is firstly divided into two sub-samples, i.e., the calibration samples y_{cal} and the validation samples y_{val}. The calibration samples will be used to find the model parameters θ^* using the maximum likelihood method. Then, the validation samples will be used to calculate the CV index defined in Eq. (3.18) given the θ^* from the calibration samples. For the current database, we assign the U.S. liquefaction case histories as the calibration samples and the remaining case histories as the validation samples.

Development of Optimal Model Using Andrus 1999 Database

Sampling Bias Effect

According to Eqs. (3.12) - (3.15), the w_L and w_{NL} are related and can be calculated from each other. Therefore, the sensitivity study of w_{NL}/w_L ratio is performed to investigate the weighting factors effect. Five levels of w_{NL}/w_L (0.875, 1.0, 1.5, 2.0 and 3.0) are selected to construct liquefaction resistance chart using logistic model (P_L = 50%) based on recommendations from previous studies by Ku et al. (2012) (w_{NL}/w_L=0.875) and Cetin et al. (2002) (w_{NL}/w_L ranging from 1.0 - 3.0). Results of the sensitivity study are shown in Figure 3.4.

The solid circles in this figure represent sites where liquefaction occurred and open circles represent sites where liquefaction did not occur. It can be seen from Figure 3.4 that the w_{NL}/w_L affects the liquefaction probability prediction. With the decrease of w_{NL}/w_L, the probabilistic curve moves toward the non-liquefied cases, which means a more conservative prediction. Since the n_L is smaller than n_{NL} for the current shear wave V_s database, the w_{NL}/w_L value should be smaller than 1. The Ku et al. (2012) approach seems more acceptable and reasonable than the Cetin et al. (2002) approach which is based on an SPT database and $n_L > n_{NL}$. Therefore, $w_L = 1.0714$ and $w_{NL} = 0.9375$ ($w_{NL}/w_L = 0.875$) are adopted for the weighted maximum likelihood function.

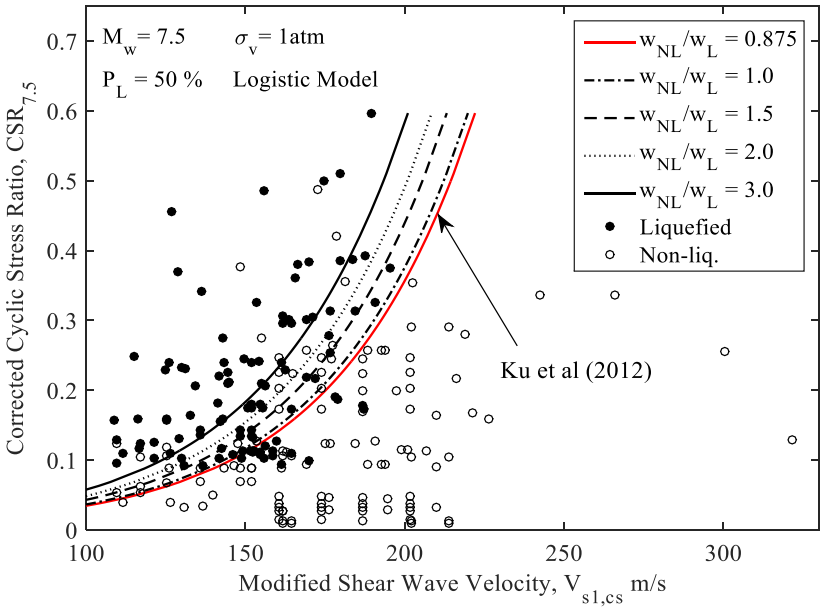

Figure 3.4: Sensitivity study of w_{NL}/w_L ratio (logistic model, $P_L = 50\%$)

It should be noted that some non-liquefied cases in Figure 3.4 clearly fall within the range of liquefied cases. There are at least two possible reasons. One is the existence of a thick capping clay layer, which might have prevented surface manifestation of liquefied

soil. Such cases would have been recorded as non-liquefied even if liquefaction had occurred as discussed in Andrus et al. (2004). Another possible reason is the measurement error in shear wave velocity, ground water table, and/or peak ground acceleration. The issue of data quality is, however, not the focus of this chapter.

Models Comparison and Selection of the Optimal Model

The model parameters of the probabilistic models established in Eqs. (3.6) - (3.9) are determined using the maximum likelihood estimation considering sampling bias as described previously, and the results are listed in Table 3.5.

Table 3.5: Model parameters and assessment index of GLMs for Andrus 1999 database

Model	Model parameters			L(q|D)	AIC	BIC	CV
	b_0	b_1	b_2				
Logistic	14.9935	-0.0614	2.6331	-91.83	189.65	199.90	43.89
Probit	8.6420	-0.0355	1.5139	-91.85	189.69	199.94	44.76
Log-log	11.5106	-0.0453	1.9321	**-90.09**	**186.17**	**196.42**	**43.22**
C-log-log	8.1913	-0.0355	1.5193	-95.54	197.07	207.32	48.89

To compare the developed logistic, probit, log-log and complementary log-log models, the liquefacion resistant charts of these four models are plotted for 6 P_L levels (5%, 10%, 30%, 50%, 85% and 95%) in Figure 3.5. It is observed that at lower levels of probability (i.e., P_L < 30%), the probabilistic curves from different GLMs are very different. The probabilistic curves of probit and logistic models are bracketed by those of log-log and c-log-log models, and the difference is more obvious with the decrease of P_L value. The c-log-log model gives the most conservative prediction, while log-log is the least convervative. For P_L = 30% and 85%, the probabilistic curves yield by the four

models are about the same. For 30% < P_L < 85%, the differences among these four models are negligible. For P_L > 85%, the log-log model becomes the least conservative and deviates from the other three models. It is noted that the probability curves of logistic and probit model are very similar for all P_L levels.

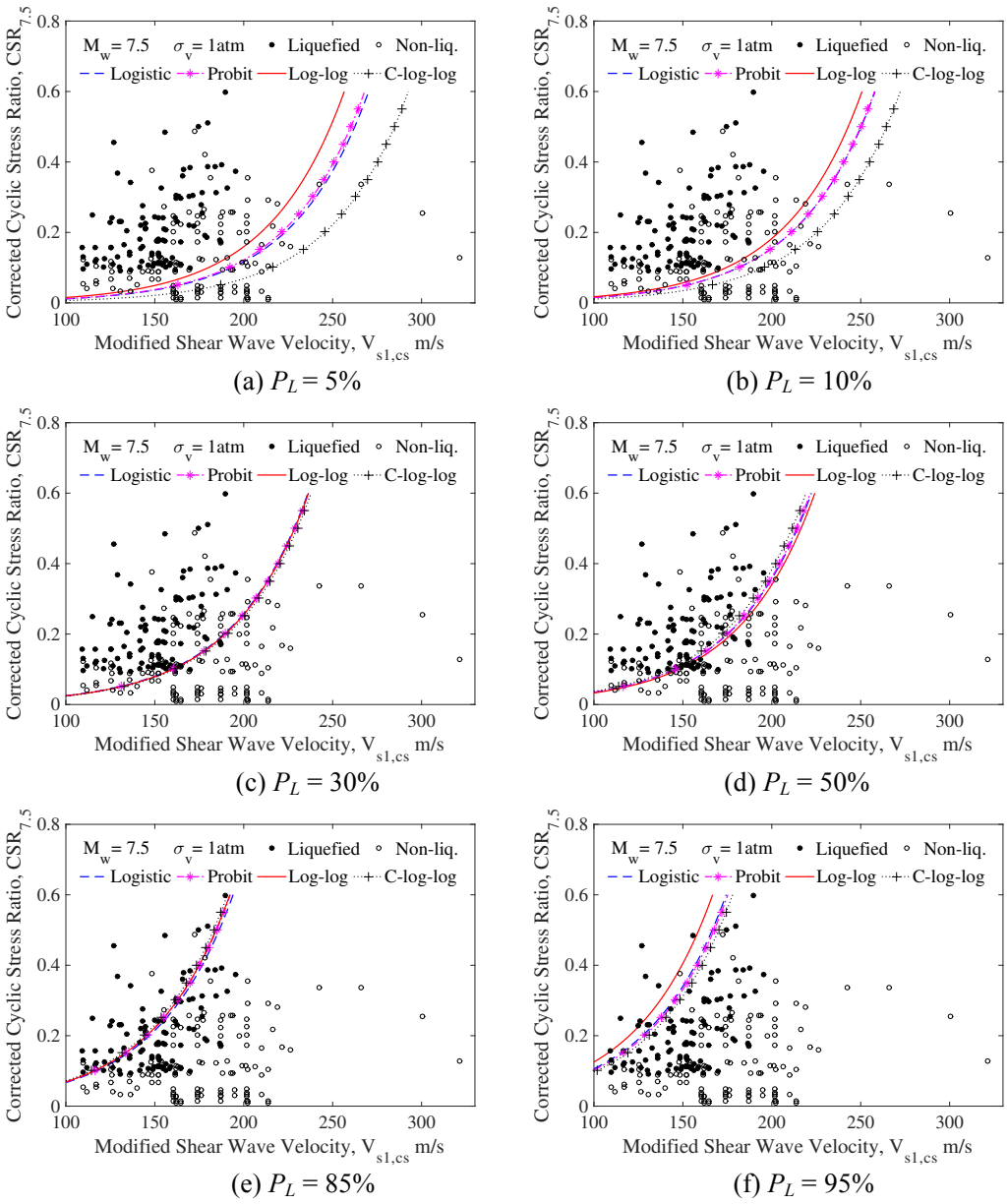

(a) P_L = 5% (b) P_L = 10%

(c) P_L = 30% (d) P_L = 50%

(e) P_L = 85% (f) P_L = 95%

Figure 3.5: Performances of the four generalized linear models under different PL levels

The developed four generalized linear models are also ranked based on the three model assessment criteria, namely AIC, BIC and CV, as expressed in Eqs. (3.16) - (3.18). The results are shown in Table 3.3. It can be concluded that the log-log model is the most optimal since it has the highest log-likelihood value and smallest AIC, BIC and CV values. The logistic model is a close second and is very attractive due to its simple functional form. Therefore, both log-log and logistic model are recommended for liquefaction evaluation based on the shear wave velocity. The model expressions are summarized in Eqs. (3.19) & (3.20).

Log-log:

$$P_L = \exp\{-\exp[-11.5106 + 0.0453V_{s1,cs} - 1.9321\ln(\mathrm{CSR}_{7.5})]\} \tag{3.19}$$

Logistic:

$$P_L = \frac{1}{1+\exp[-14.9935 + 0.0614V_{s1,cs} - 2.6331\ln(\mathrm{CSR}_{7.5})]} \tag{3.20}$$

Comparison with Existing Model

The log-log model, as a new proposed probabilistic model for V_s-based liquefaction evaluation, is compared with two existing models that were developed using the same database (Juang et al. 2002). The first model, denoted as the Juang 2002 logistic model, is developed by a simple logistic regression approach. The expression is shown in Eq. (3.21). The second model, denoted as the Bayesian model, is developed using the Bayesian mapping function. It is expressed in terms of factor of safety F_S and shown in Eq. (3.22).

$$P_L = \frac{1}{1+\exp[-14.8967+0.0611V_{s1,cs}-2.6418\ln(CSR_{7.5})]} \tag{3.21}$$

$$P_L = \frac{1}{[1+(\frac{F_S}{0.73})^{3.4}]} \tag{3.22}$$

The Juang 2002 logistic model is similar in functional form as the logistic model proposed in this chapter, Eq. (3.20), but the model parameters are slightly different. The differences may be caused by the sampling bias effect correction. The comparison between Juang 2002 logistic model and the log-log model proposed in this chapter is shown in Figure 3.6(a). For $P_L < 0.3$ and $P_L > 0.85$, probabilistic curves of the proposed log-log model locate to the left side of the Juang 2002 logistic model, which means the proposed log-log model gives less conservative prediction than the Juang 2002 logistic model. For $P_L = 0.3$ and $P_L = 0.85$, the probabilistic curves of the two models yield very similar predictions. For P_L between 0.3 and 0.85, the proposed log-log model is slightly more conservative than the Juang 2002 logistic model. Such conservative prediction from log-log model has also been observed in Figure 3.5 when compared to the proposed logistic model.

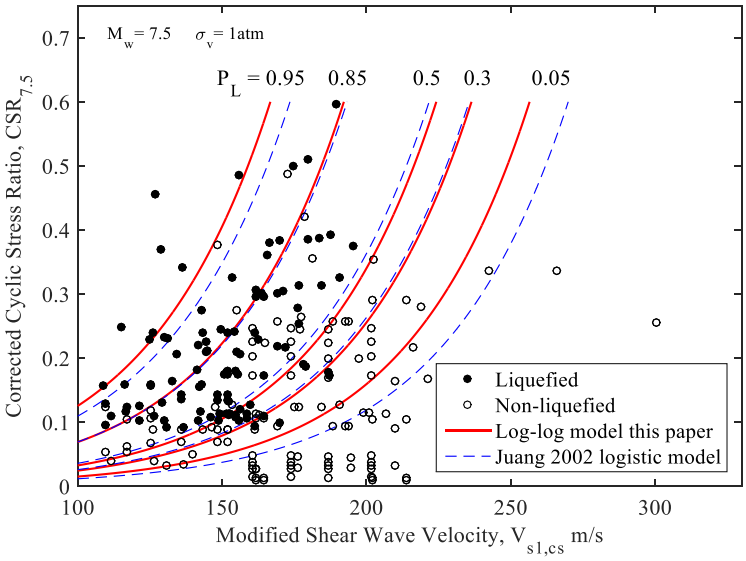

(a)

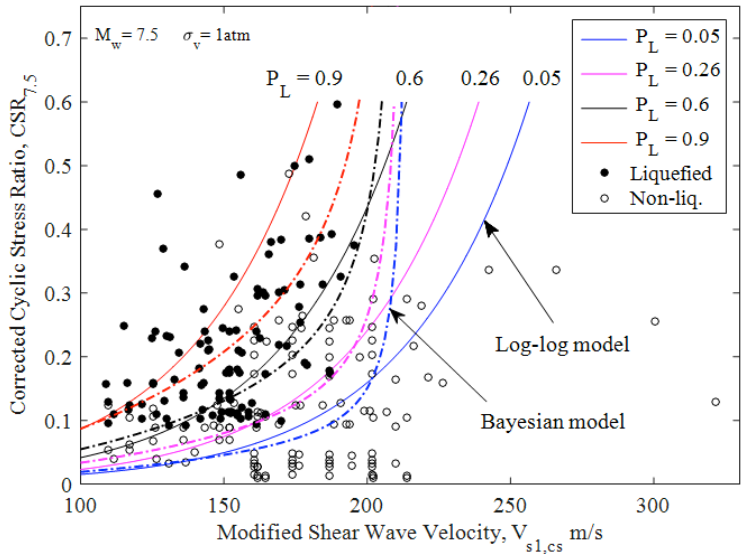

(b)

Figure 3.6: Comparison of log-log model with the existing Juang 2002 logistic model and the Bayesian model; (a) Log-log model and Juang 2002 logistic model; (b) Log-log model and the Bayesian model.

The Bayesian model, which is expressed in terms of F_S, can be converted to forms comparable to the GLMs recoganizing that $F_S = \mathrm{CRR}_{7.5}/\mathrm{CSR}_{7.5}$ and $\mathrm{CRR}_{7.5}$ is a function of $V_{s1,cs}$ as shown in Eq. (A.5). For $F_S = 1$, which is the critical state for a deterministic

method, P_L = 0.26 according to Eq. (3.25). The comparison of the Bayesian model and the log-log model is shown in Figure 3.6(b). From the plot, it can be seen that probabilistic curves yield by the Bayesian model deviate from the log-log model especially for larger values of $V_{s1,cs}$ and $CSR_{7.5}$. For instance, for P_L = 0.26, which corresponding to F_S = 1 in the Bayesian model, the log-log model yields significantly lower $CSR_{7.5}$ compared to the Bayesian model for $V_{s1,cs}$ greater than 200 m/s. The lack of case history data in region of the high shear wave velocity, along with the choice of functional form, might have contributed to such significant disparity between two models. When P_L = 0.6, the probabilistic curves of Bayesian model and log-log model are most close to each other. Finally, when P_L < 0.6 the log-log model is more conservative than Bayesian model, while less conservative when P_L > 0.6.

An Update of Proposed Models Using Combined Database

Model Performance for the 22 February 2011 Earthquake

Before updated the proposed models using the combined database, these models are first checked for their performance against the newly compiled case histories from the 22 February 2011 Canterbury earthquake.

The 45 case histories data listed in Table 3.1, and the proposed log-log and logistic model in Eqs. (3.19) & (3.20), are plotted in Figure 3.7. It is noted that 36 of the 45 data are serious liquefied cases and the other 9 are marginal liquefied cases. It can be seen from Figure 3.7 that 30 of the 36 serious liquefied cases are above the probabilistic curve P_L = 0.65, which, according to the liquefaction likelihood classification defined by Chen

and Juang (2000), is very likely to liquefy. Only two liquefied cases are shown to have a probability of less than 35%. Thus, the proposed models are quite satisfactory in predicting the liquefaction in the 22 February 2011 Canterbury earthquake.

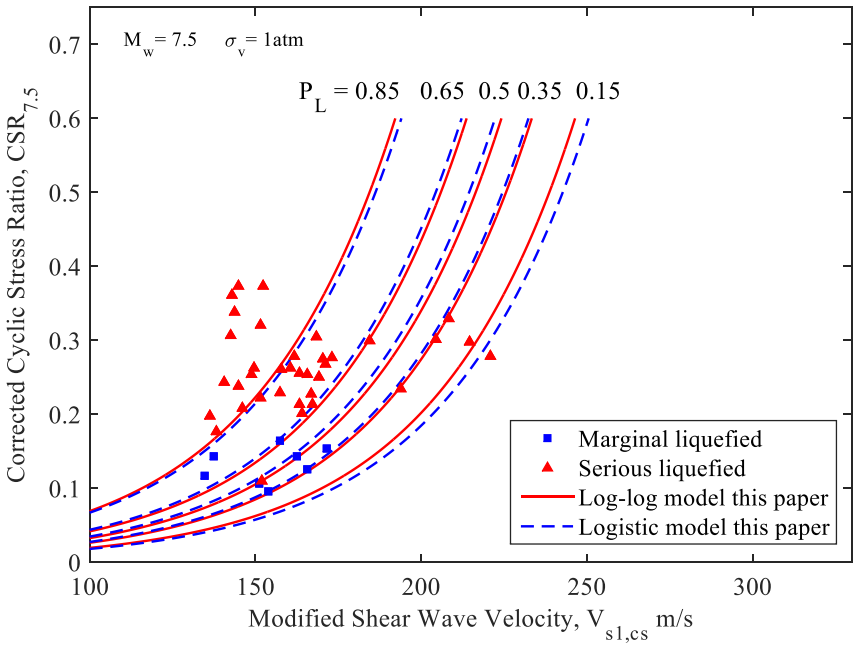

Figure 3.7: Performance of the proposed log-log and logistic model in 22 February 2011 Canterbury earthquake.

Update of the Proposed Models

The above analysis shows that the developed log-log model and logistic model are able to predict new case histories with reasonable accuracy. As more data are available, the developed models can be updated by incorporating more data into the database. In this section, the original Andrus 1999 database is expanded with the 36 serious liquefied case histories compiled in this study from the 22 February 2011 Canterbury earthquake, which results in a combined database of 261 cases. The statistics of the key variables for liquefaction models based on the combined database is shown in Table 3.6.

Table 3.6: Statistics of the variables for combined database

Statistics index	Depth	σ_v	σ_v'	a_{max}	M_w	V_s
	(m)	(kPa)	(kPa)	(g)	/	(m/s)
Minimum	1.9	38.4	27.8	0.02	5.3	74
Maximum	15	299.3	195.4	0.65	8.3	274
Mean	5.4	98.2	65.0	0.26	6.7	143
Standard deviation	2.1	39.5	28.2	0.16	0.6	31
Coefficient of variation	0.400	0.402	0.434	0.628	0.092	0.214

Following the methodology proposed in Section of *Ground Motions of the 22 February 2011 Earthquake*, the four GLMs can be developed based on the combined database. The weighting factors using Ku et al. (2012) approach are calculated to be w_L = 0.9255 and w_{NL} = 1.0875 (w_{NL}/w_L = 1.175), which is adopted for the sampling bias correction. The updated model parameters and the results of model assessments are summarized in Table 3.7.

Table 3.7: Model parameters and assessment index of GLMs for combined database

Model	Model parameters			L(q|D)	AIC	BIC	CV
	b_0	b_1	b_2				
Logit	14.3931	-0.0552	2.8628	-105.89	217.77	228.47	50.38
Probit	8.3135	-0.0320	1.6468	-105.95	217.91	228.60	51.36
Log-log	10.9640	-0.0397	2.1304	**-104.09**	**214.17**	**224.87**	**49.43**
C-log-log	7.9444	-0.0328	1.6283	-110.02	226.04	236.73	55.90

The log-log model remains the optimal model by AIC, BIC and CV criteria while the logistic model ranks second for the combined database. Those results are consistent with results based on the Andrus 1999 database. The updated functional form for the log-log and logistic models are shown in Eqs. (3.23) & (3.24), respectively.

Updated log-log:

$$P_L = \exp\{-\exp[-10.9640 + 0.0397V_{s1,cs} - 2.1304\ln(CSR_{7.5})]\} \tag{3.23}$$

Updated logistic:

$$P_L = \frac{1}{1+\exp[-14.3931 + 0.0552V_{s1,cs} - 2.8628\ln(CSR_{7.5})]} \tag{3.24}$$

The liquefaction resistance charts using the updated log-log and logistic models based on the combined database are shown in Figure 3.8(a) and Figure 3.8(b), respectively.

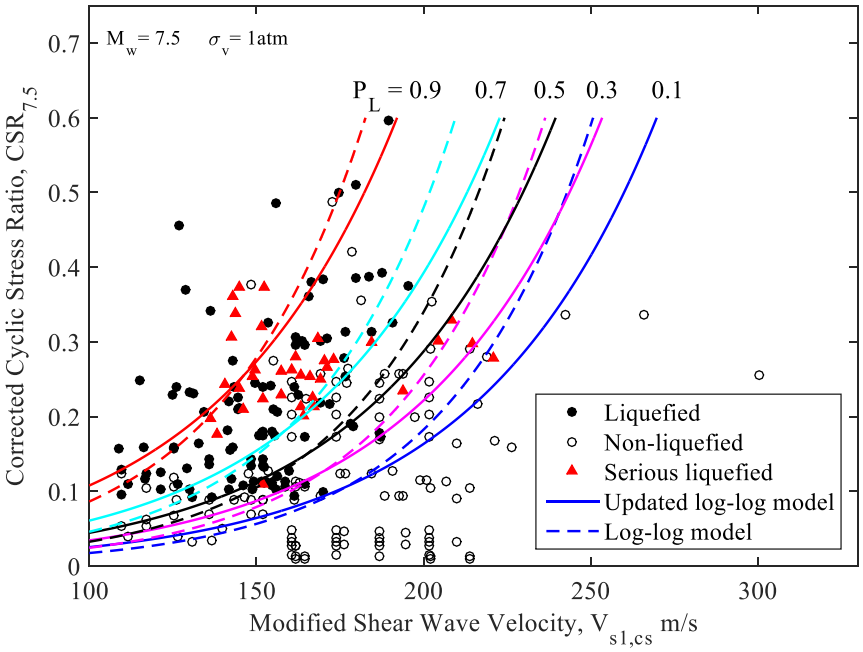

(a)

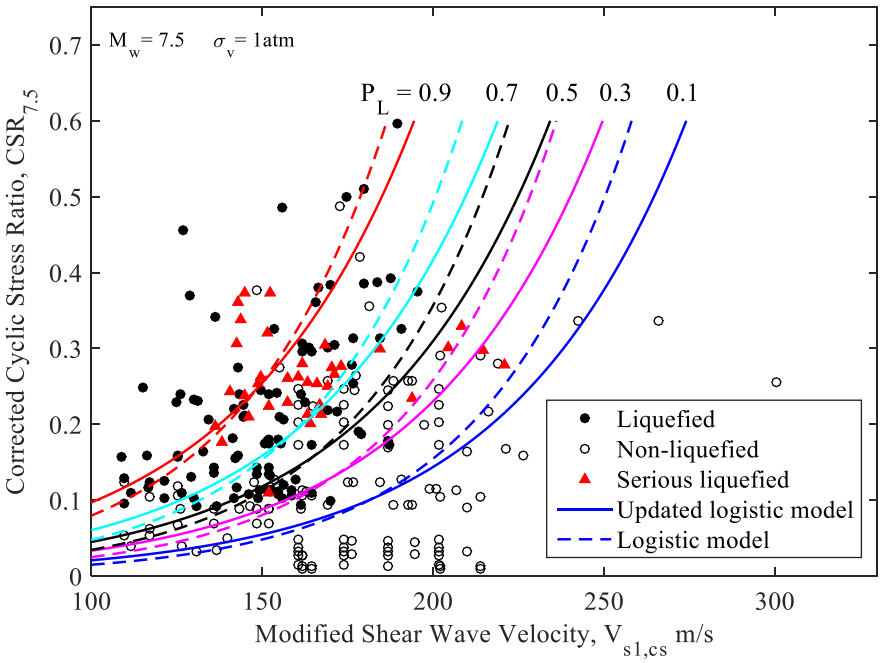

(b)

Figure 3.8: Liquefaction resistance charts of updated log-log/logistic model for combined database and log-log/logistic model for Andrus 1999 database; (a) Log-log model; (b) Logistic model.

The log-log and logistic models based on the Andrus 1999 database are also plotted. Compared to the original models based on Andrus 1999 database, the probability curves of the updated log-log or logistic model shift down to accommodate more liquefied cases added from the Canterbury earthquake, especially in the region with high $V_{s1,cs}$ and $CSR_{7.5}$ values. The probabilistic curves of generalized linear models are found sensitive to the database used for model development.

Summary

In this chapter, probabilistic models for liquefaction potential evaluation based on V_s measurements are developed. Four probabilistic models based on generalized linear

models (GLMs) are developed and calibrated. The maximum likelihood estimation is used to determine the model parameters. Then, the developed generalized linear models are ranked using multiple statistical criteria and applied to assess new case histories derived from the 22 February 2011 Canterbury Earthquake. Based on the assessment criteria adopted, the log-log and logistic models were recommended for the adopted database. The updated log-log model and logistic model were recommended for V_s-based liquefaction potential evaluation.

CHAPTER IV[2]

RANDOM FIELD-BASED REGIONAL LIQUEFACTION HAZARD MAPPING — DATA INFERENCE AND MODEL VERIFICATION USING A SYNTHETIC DIGITAL SOIL FIELD

Introduction

Liquefaction evaluation is an important issue in the field of geotechnical earthquake engineering. Many simplified liquefaction evaluation models have been developed based on collected databases of case histories in the past earthquakes, following the framework of the original simplified procedure (Seed and Idriss, 1971 & 1982). These simplified methods rely on in situ testing, e.g., the standard penetration test (SPT), the cone penetration test (CPT), or the shear wave velocity (V_s) test, as a way to obtain and characterize the strength of the soil to resist liquefaction (e.g., Seed et al. 1985; Robertson and Wride 1998; Andrus and Stokoe 2000; Youd et al. 2001; Finn 2002, Juang et al. 2002&2003; Cetin et al. 2004; Moss et al. 2006; Boulanger and Idriss 2012; Sara et al. 2015; Shen et al. 2016).

Those simplified methods have been used to evaluate liquefaction potential at an in situ test location. To estimate or map liquefaction potentials over an extended region, the

[2] A similar form of this chapter is published as: Juang, C. H., Shen, M., Wang C., & Chen, Q. (2017). Random field-based regional liquefaction hazard mapping - data inference and model verification using a synthetic digital soil field. Bulletin of Engineering Geology and the Environment, doi:10.1007/s10064-017-1071-y.

spatial variation and dependence of soil properties and liquefaction potentials need to be considered. To this end, geostatistical tools and random field models have been increasingly used in recent regional liquefaction mapping.

Focusing on how spatial variations and dependence are considered and incorporated in the mapping process, three types of approaches may be proposed and will be investigated in this study, i.e., the averaged index approach, the two-dimensional (2D) local soil property approach, and the three-dimensional (3D) local soil property approach. To illustrate these approaches, the liquefaction potential at a given location is quantified through an index called the liquefaction potential index (LPI) (Iwasaki et al. 1978&1982; Sonmez 2003). In the averaged index approach, the spatial dependence of liquefaction potential (quantified by LPI) at the test locations is characterized and used as input to random field-based LPI mapping. This approach is widely used in current liquefaction hazard mapping studies (e.g., Holzer et al. 2006a&b; Li et al. 2006; Baise et al. 2006&2008; Lenz and Baise 2007; Juang et al. 2008; Chen et al. 2015; van Ballegooy et al. 2015; Wang et al. 2017). In the 2D and 3D local soil property approaches, the spatial dependence of soil properties, e.g., the cone tip resistance (q_c) and the sleeve resistance (f_s) obtained from CPT tests, or the corrected blow counts $N_{1,60}$ from SPT tests, are characterized and treated as spatially correlated random variables. Once soil properties of interest are generated through random field models for the entire studied region, the corresponding liquefaction potential can be calculated. In the 2D local soil property approach, only the horizontal correlation is considered. The random soil property field is generated layer-by-layer considering the horizontal correlation within the current layer

(e.g., Fenton, 1999; Liu and Chen, 2006; Baker and Faber, 2008; Vivek and Raychowdhury, 2014). In contrast, 3D local soil property approach considers the horizontal and vertical correlations simultaneously. There are few studies that employ a full 3D soil field in regional liquefaction mapping. Examples include the work by Dawson and Baise (2004), and that by Liu et al. (2016), where the authors applied 3D interpolation to evaluate the extent of liquefiable materials.

While geostatistical tools and random field models are increasingly used in liquefaction mapping studies, a systematic assessment and verification of different approaches to account for spatial variation and dependence of soil properties or liquefaction potentials are missing and the implications of various random field-based mapping approaches are unknown. The main challenge is the lack of sufficient data, and therefore lack of knowledge about the soil properties and liquefaction potentials of the field. Moreover, in situ test data are typically sampled at selected and sometimes clustered locations, resulting in additional complexities to assess random field-based model performance.

To overcome these challenges, in this chapter, an extremely detailed three-dimensional synthetic digital soil field is artificially generated and used as a basis to assess and verify various random field-based approaches for liquefaction mapping. Soil properties of interest (e.g., the CPT tip resistance) are known at every location in the synthetic field. The benchmark liquefaction potential fields can, therefore, be obtained for any given hypothetical earthquake event. Moreover, different virtual field test plans are designed to assess their effects on data inference and model performances.

Given such an extensive amount of information, this study will assess and verify various common and uncommon random field-based liquefaction mapping approaches. In particular, this study will assess: (1) the performance and effectiveness of various approaches in mapping quantities of interest (e.g., soil properties, LPIs) over studied region; (2) the effect of amount of field data on the relative performances of different approaches, and (3) the optimal random field-based liquefaction model for mapping liquefaction hazards. This study aims to provide insights on approaches that are commonly used to account spatial variability and dependence in random field-based liquefaction mapping studies.

The remainder of the chapter is structured as follows: in Section of *Random Field-Based Approaches for Liquefaction Mapping*, details of the three random field-based approaches and the adopted random field models are presented; Section of *Synthetic Digital Soil Field and Benchmark Liquefaction Potential Field* provides details of the synthetic digital soil field, where the equivalent clean-sand normalized CPT penetration tip resistance $(q_{c1N})_{cs}$ is considered as soil property of interest and the corresponding benchmark liquefaction potential field is calculated; Section of *Procedure for Model Verification* describes the procedure for model verification, including virtual field testing plans and measures to quantify model performance; Section of *Results and Discussions* presents and discusses results of model verification.

Random Field-Based Approaches for Liquefaction Mapping

In this section, three random field-based approaches for liquefaction mapping are

described along with details of the random field model used in the following simulations.

Mapping Liquefaction Potentials

In this study, a classical CPT-based liquefaction model proposed by Robertson and Wride (1998) and subsequently updated by Robertson (2009) is used to evaluate liquefaction potential of a soil layer. The liquefaction hazard is then quantified and mapped over a region in terms of the liquefaction potential index (LPI) (Iwasaki et al. 1978&1982). Details of the CPT-based liquefaction model and the LPI calculations are included in Appendixes B and C. Depending on how the spatial dependence and variation are integrated in the mapping process, three common and uncommon random field-based approaches will be assessed and verified: the averaged index approach, the two-dimensional (2D) local soil property approach and three-dimensional (3D) local soil property approach, which are denoted herein as M1, M2 and M3, respectively. A schematic detailing these three approaches is shown in Figure 4.1.

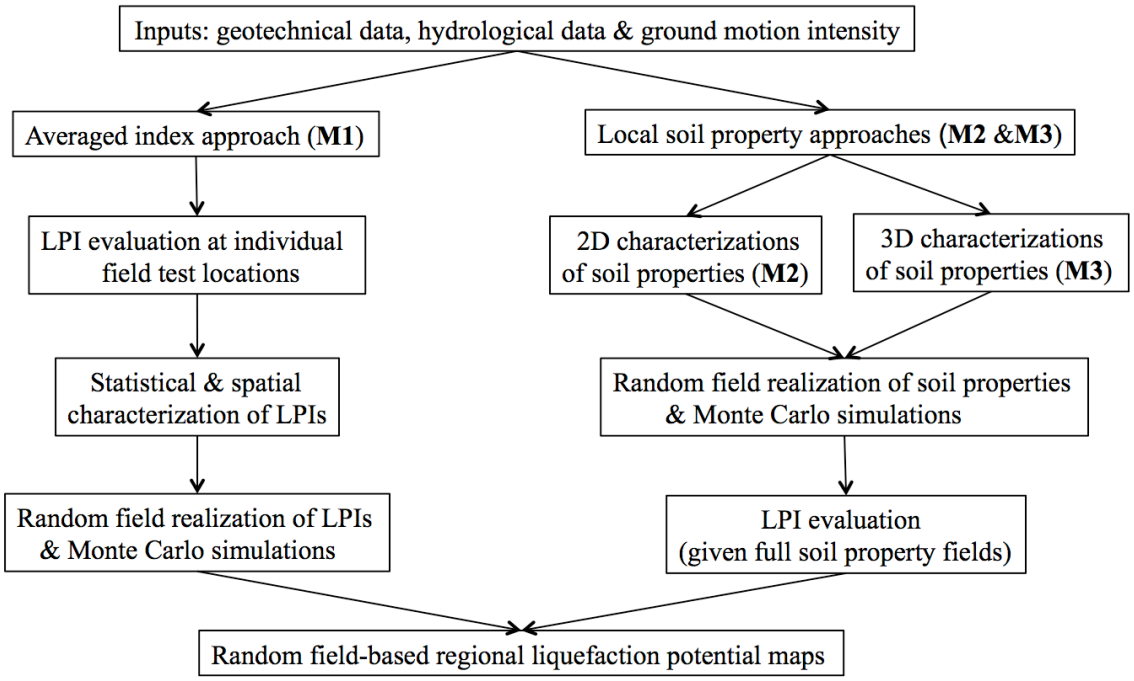

Figure 4.1: The approaches for random field-based liquefaction mapping.

As shown in the figure, the averaged index approach (M1) treats the LPI as the spatially correlated random variable while the 2D and 3D local soil property approaches (M2 and M3) treat the soil properties of interest (e.g., tip resistance from CPT test) as spatially correlated random variables. In the 2D local soil property approach, the random field of soil properties is generated layer-by-layer considering the horizontal correlation within each layer. In contrast, the 3D local soil property approach considers both horizontal and vertical spatial correlations. All approaches will rely on the random field models (described in the next section) and Monte Carlo simulations to generate regional liquefaction potential maps.

Random Field Models

Spatial structures commonly exist in natural soil deposits as evidenced by the fact that

soil properties measured at one location are more similar to those at neighboring locations than those further away. In this work, spatial structure is described using a form of covariance known as the semivariogram $\gamma(\boldsymbol{h})$, which is equal to half the variance of two variables separated by a vector distance $\boldsymbol{h}$

$$\gamma(\boldsymbol{h}) = \frac{1}{2}\mathrm{Var}[Z(\boldsymbol{u}) - Z(\boldsymbol{u}+\boldsymbol{h})] \tag{4.1}$$

where $Z(\boldsymbol{u})$ and $Z(\boldsymbol{u}+\boldsymbol{h})$ are the values of the variable under consideration at locations $\boldsymbol{u}$ and $\boldsymbol{u}+\boldsymbol{h}$, respectively. A scalar form of the vector distance, denoted as h, is commonly used to account for both separation distance and geometric anisotropy

$$h = \sqrt{(\frac{h_x}{a_x})^2 + (\frac{h_y}{a_y})^2 + (\frac{h_z}{a_z})^2} \tag{4.2}$$

where h_x, h_y and h_z are the scalar components of the vector distance along the principal axes of the field; and a_x, a_y and a_z are the corresponding ranges or correlation lengths used to specify how quickly the spatial dependences decrease along those axes.

To generate random field realizations of the variables of interest, a conditional sequential Gaussian simulation method (Goovaerts, 1997) is implemented, which has been extensively used by mining scientists and geostatisticians for natural resource evaluations and spatial prediction of geohazards. It is worth noting that a multiscale extension of this conditional sequential Gaussian simulation method has been developed in recent studies (Baker et al., 2011, Chen et al., 2012, 2015, &2016, Liu et al. 2017).

Following the sequential simulation method, the simulation process could be briefly described as

$$(Z_n \mid \boldsymbol{Z}_p = \boldsymbol{z}) \sim N(\Sigma_{np} \cdot \Sigma_{pp}^{-1} \cdot z, \sigma_n^2 - \Sigma_{np} \cdot \Sigma_{pp}^{-1} \cdot \Sigma_{pn}) \tag{4.3}$$

in which the unknown value, Z_n, at an unsampled location n is drawn from the conditional normal distribution with the mean $(\Sigma_{np} \cdot \Sigma_{pp}^{-1} \cdot z)$ and the variance $(\sigma_n^2 - \Sigma_{np} \cdot \Sigma_{pp}^{-1} \cdot \Sigma_{pn})$; $\boldsymbol{Z}_p$ is the vector known data; Σ is the covariance matrix of neighboring measurements; the subscription p and n mean "previous" and "next", respectively. Once the unknown value Z_n is generated, it is inserted into the "previous" vector, i.e., the known data vector $\boldsymbol{Z}_p$, upon which the "next" unknown value at another un-sampled location will be generated. Detailed process of random field modeling may be found in Chen et al. (2012) and Chen et al. (2015).

Random field models incorporate the spatial dependence of the measured parameter through the covariance matrix. The covariance of values at two separated locations could be expressed as

$$\Sigma = \mathrm{COV}[Z_i, Z_j] = \rho_{Z_i, Z_j} \cdot \sigma_{Z_i} \cdot \sigma_{Z_j} \tag{4.4}$$

where ρ_{Z_i, Z_j} is the correlation between the random variables Z_i and Z_j with standard deviations of σ_{Z_i} and σ_{Z_j}, respectively. The correlation ρ is used to describe the similarity of spatial measurements and is related to the semivariogram $\gamma(\boldsymbol{h})$ by

$$\rho(h) = 1 - \gamma(h) \tag{4.5}$$

An exponential semivariogram model can be expressed as

$$\gamma(h) = 1 - e^{-h} \tag{4.6}$$

where h can be calculated by Eq.(4.2).

Once the empirical semivariogram $\gamma(h)$ is characterized, it will be plugged into the

covariance matrix Eq. (4.4) through Eq. (4.5). Thus the unknown value Z_n at location n could be drawn using Eq. (4.3). The generated value is then assigned to location n and treated as known data. This process is repeated until all the unsampled locations are assigned with values.

Synthetic Digital Soil Field and Benchmark Liquefaction Potential Field

To verify the random field-based liquefaction models generated by the approaches presented in Section of *Mapping Liquefaction Potentials*, a spatially correlated synthetic digital soil field is created and its liquefaction potential fields are used as benchmarks.

Spatially Correlated Synthetic Digital Soil Field

The dimension of the synthetic digital soil field is set as 1000 ×1000 ×20 m (width × length × deep) and a soil element size is correspondingly set as 10 ×10 ×0.05 m. There are a total of 4,010,000 soil elements in the field. The depth of the digital field (20 m) corresponds to the integration depth in LPI calculation defined in Eq. (C.1). The soil element is assigned to have a thickness of 0.05 m to match the vertical sampling interval of a typical CPT test.

Within this field, a three-dimensional and spatially correlated clean sand equivalent tip resistance $(q_{c1N})_{\mathrm{cs}}$ field is generated and its values are assigned to each soil element as shown in Figure 4.2(a). The parameters used to generate the synthetic field are based on the experience gained through the spatial analysis of CPT database in Alameda County of California (Chen et al., 2016; USGS, 2015).

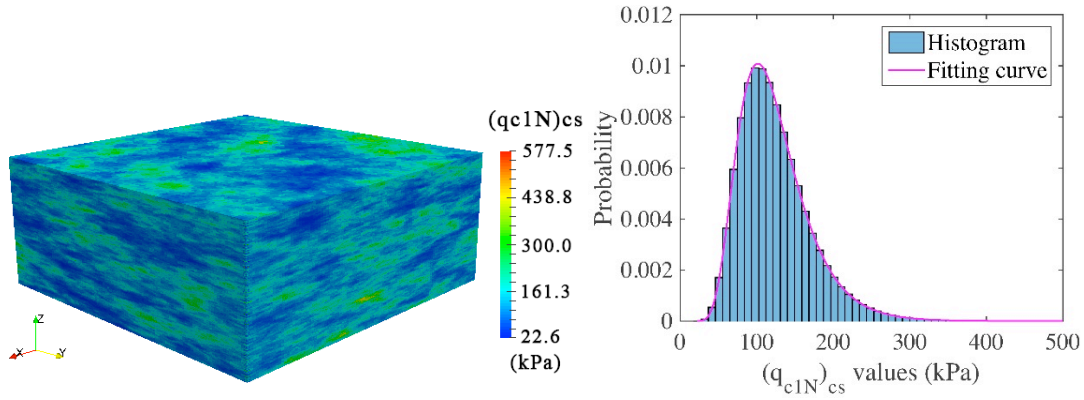

(a) Three-dimensional view (b) Histogram

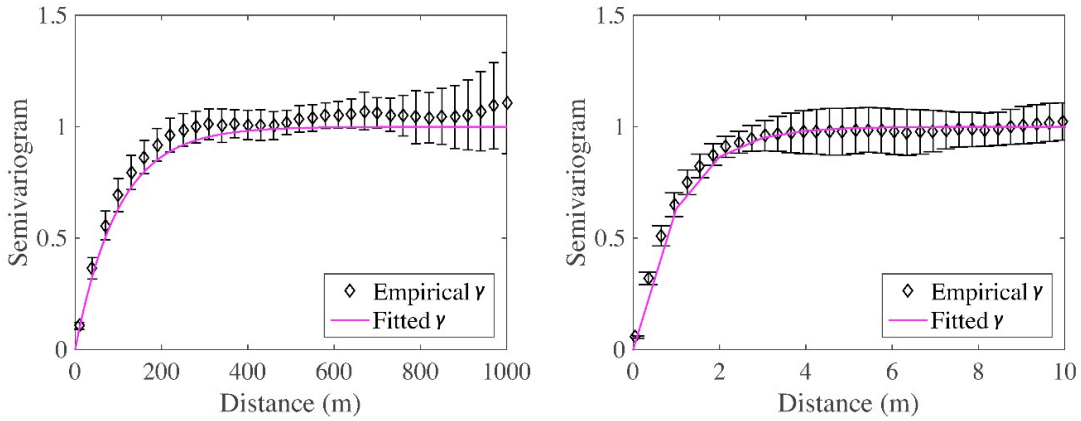

(c) Semivariogram in XY plane (d) Semivariogram in YZ plane

Figure 4.2: The three-dimensional view, the histogram and semivariograms of the synthetic digital $(q_{c1N})_{cs}$ field. The empirical semivariograms (c) and (d) show both the mean values as well as the error bars (± standard deviation) from the averaging of all layers.

The $(q_{c1N})_{cs}$ of the digital soil field is assumed to follow a lognormal distribution, and the spatial correlation of the field is specified as isotropic in the horizontal plane and anisotropic in the vertical plane. The histogram of the $(q_{c1N})_{cs}$ is shown in Figure 4.2(b), with the mean μ and the variance σ^2 as 123.98 kPa and 2182.68 kPa, respectively. The semivariogram $\gamma(h)$ in the XY plane and YZ plane are respectively shown in Figure

4.2(c) and Figure 4.2(d). The error bars (± one standard deviation σ) represent the variance of empirical semivariogram in the 401 XY planes and 100 YZ planes. The magenta line is the fitted γ by Eq. (4.6), and the correlation length $a_x = a_y = 82.59$ m, $a_z = 0.915$ m. For simplicity, the synthetic digital $(q_{c1N})_{cs}$ field is denoted as the "true" $(q_{c1N})_{cs}$ field for use in subsequent model verifications. It should be noted that the true distribution and spatial structure of this digital soil field are unknown to random field-based liquefaction modeling and mapping, same as in the case of a real soil field. The lognormal and assumptions made on spatial correlation are for the convenience of generating the digital field.

Benchmark Liquefaction Potential Field

To calculate the benchmark liquefaction potential index (LPI) field, the following input data for liquefaction model and for a hypothetical earthquake scenario are used: the moist unit weight of the soil γ_m is taken as a constant at 15 KN/m^3, the saturated unit weight γ_{sat} is 19 KN/m^3, the ground water table GWT is at 3 m below ground surface, the maximum horizontal acceleration at the ground surface a_{max} = 0.3g and the moment magnitude $M_w = 7.0$.

The resulting benchmark LPI field is shown in Figure 4.3. It will be used as the benchmark liquefaction potential field for further verification and is denoted as the "true" LPI field. According to the severity class of liquefaction listed in Table 5.1 (Sonmez, 2003), most areas of the field are classified as "high" (IV) or "very high" (V) under the hypothetical earthquake scenario.

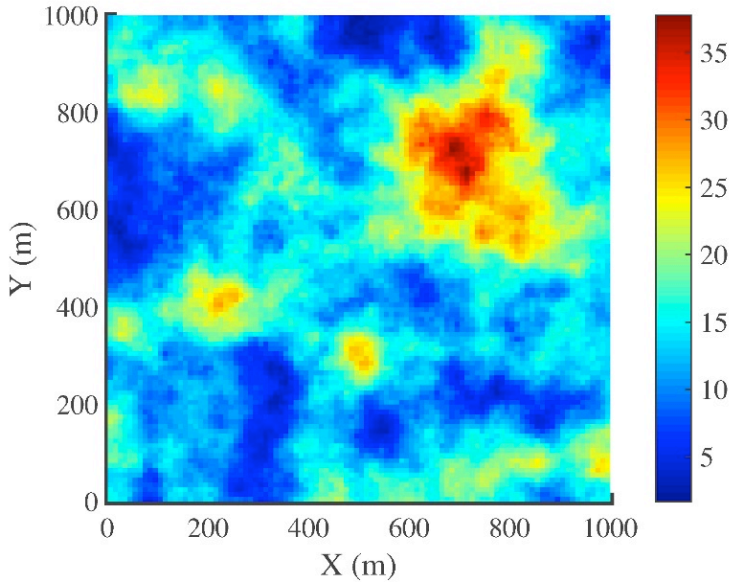

Figure 4.3: The true LPI field under the hypothetical earthquake ($a_{max} = 0.3g$ and $M_w = 7.0$).

Table 4.1: The classification of the Liquefaction Potential Index (LPI) (Sonmez, 2003).

Liquefaction potential index (LPI)	Severity class of liquefaction
LPI = 0	I: Non-liquefiable
0 < LPI ≤ 2	II: Low
2 < LPI ≤ 5	III: Moderate
5 < LPI ≤ 15	IV: High
LPI > 15	V: Very high

The semivariogram of the true LPI field are shown in Figure 4.4(a), and the correlation length $a_x = a_y$ =114.63 m. Figure 4.4(b) is the histogram of the true LPI field. The true LPI approximately follows a lognormal distribution as indicated by the magenta line, and the mean μ and variance σ^2 are 14.20 and 33.66, respectively.

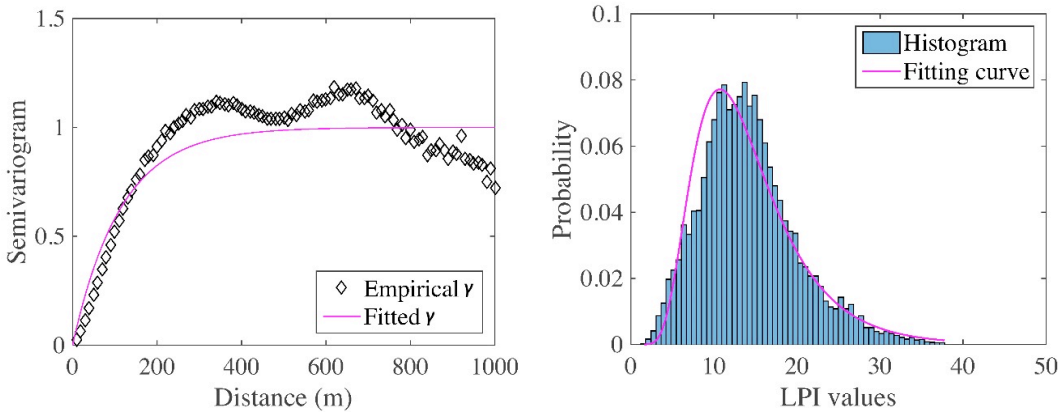

(a) Semivariogram (b) Histogram

Figure 4.4: The semivariogram and histogram of the true LPI field.

Procedure for Model Verification

Virtual Site Investigation Plans

As suggested by Webster and Oliver (1992), a sample size of 100 should give acceptable confidence to estimate variograms or semivariograms of soil properties. Two investigation plans are designed in this chapter to compare the model performances under the scenarios of sufficient and insufficient sample size. As shown in Figure 4.5, plan #1 is designed with a total of 225 evenly -spaced CPT soundings, where the $(q_{c1N})_{cs}$ is extracted from the digital soil field at each sounding location. As a comparison, plan #2 has only 36 evenly-spaced CPT soundings and is used to gauge the random field model performance under insufficient test samples. For the investigation purpose, the element size for investigation plans is designed with 20 m×20 m×0.05 m, which is identical in the vertical direction but four times larger in the XY plane than that of the synthetic digital $(q_{c1N})_{cs}$ field. Five locations marked in the figure, A, B, C, D and E, are used for verification of $(q_{c1N})_{cs}$ profiles. It should be noted that evenly-spaced sampling plans are

considered in the current study, which simplifies the inference process for random field model parameters. In the real-world field investigations, unevenly spaced or clustered sampling locations are commonly used and the inference of random field model parameters can be more challenging. A preliminary analysis in an ongoing study, however, shows that the conclusions reached and presented in this chapter are still valid with unevenly spaced sampling plans.

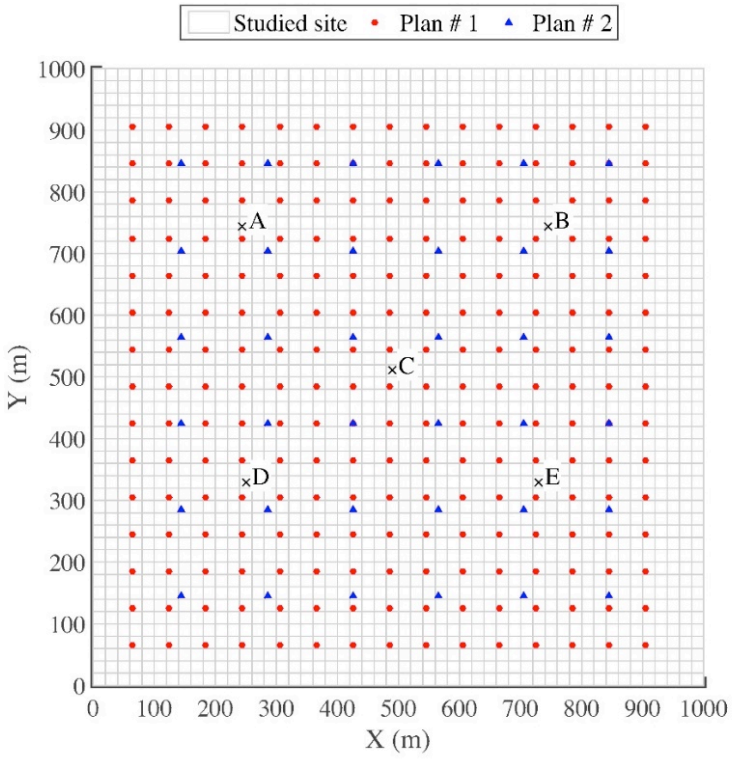

Figure 4.5: The layouts of the virtual site investigation plans (Locations A, B, C, D and E are marked and used subsequently for model verification).

Sample $(q_{c1N})_{cs}$ profiles at selected locations (points A and B in Figure 4.5) are shown in Figures 4.6(a) and 4.6(b), respectively. The corresponding profiles of cyclic resistance ratio (CRR), the cyclic stress ratio (CSR) and the factor of safety (F_S) are

calculated and plotted. With the F_S profile, the LPI value at a specific location can be calculated by integrating the F_S along the soil depth using Eq. (C.1).

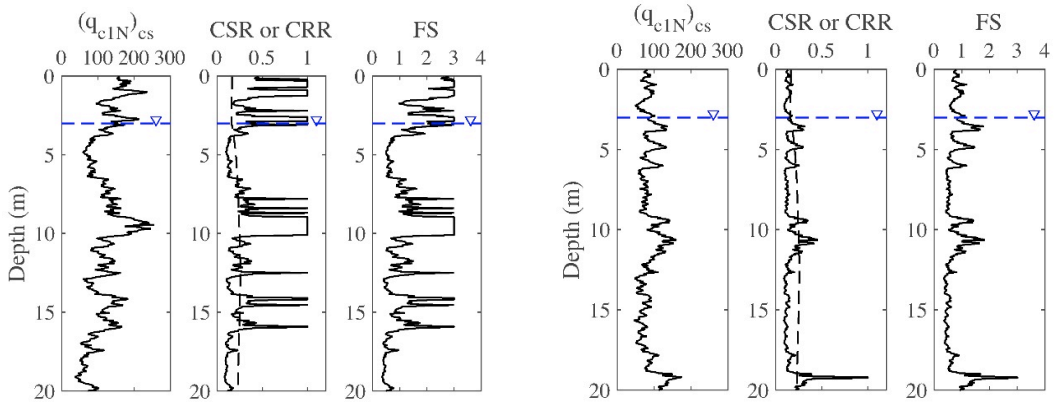

(a) The profiles at location A (b) The profiles at location B

Figure 4.6: The profiles for the test samples at location A and B marked in Figure 4.5 (the blue dash lines at depth of 3 m represent the ground water table; the black dash lines in CSR or CRR subplots represent the CSR and the black solid lines represent the CRR).

Data Inference and Random Field-Based Liquefaction Model Generation

The previously described investigation plans provide "field data" necessary to infer random field model parameters. For the averaged index approach (M1), the LPI values at field testing location are needed. For the local soil property approaches (M2 and M3), soil property, e.g., $(q_{c1N})_{cs}$ values, are needed. Regardless of the mapping approach, statistical parameters (e.g., the statistical distribution, mean μ and variance σ^2) are inferred from field data. Empirical semivariograms are calculated, from which analytical semivariogram models (e.g., an exponential semivariogram function) can be fitted. With the parameters for statistics and semivariogram of the test samples, the random field-based liquefaction models can be generated using procedures discussed in Section of *Random field-based approaches for liquefaction mapping*. For each mapping approach,

1000 Monte Carlo simulations (MCSs) are performed, providing data to estimate not only the expected values of the mapped quantities across the field but also the associated uncertainties.

Assessment of Model Performance

The model performances of random field-based liquefaction models are assessed using the "true" data from the synthetic digital soil field and the benchmark liquefaction potential field (true fields). The models are assessed for two aspects: 1) histogram assessments to check if the random field models can simulate the data distribution of the true fields, and 2) semivariogram assessments to verify if the random field models can capture the spatial variability of the true fields. These assessments are made for both $(q_{c1N})_{cs}$ field and LPI field. For $(q_{c1N})_{cs}$ field, the comparisons of $(q_{c1N})_{cs}$ profiles at specific locations are made to verify the random field-based liquefaction model performances. And for LPI field, the cumulative frequency plot and differences between true and simulated fields are assessed to evaluate the model performance.

In addition, three information theory-based measures are adopted to quantitively assess model performances, i.e., the mean absolute percentage error (MAPE), the root mean square deviation (RMSD) and the bias factor (Armstrong and Collopy, 1992; Prasomphan and Mase, 2013; Kung et al., 2007; Juang et al., 2012b).

$$\text{MAPE} = \frac{1}{n}\sum_{i=1}^{n}\left|\frac{(X_{\text{true}})_i - (X_{\text{sim}})_i}{(X_{\text{true}})_i}\right| \tag{4.15}$$

$$\text{RMSD} = \sqrt{\frac{1}{n}\sum_{i=1}^{n}[(X_{\text{true}})_i - (X_{\text{sim}})_i]^2} \tag{4.16}$$

$$\text{Bias factor} = \frac{1}{n}\sum_{i=1}^{n}\frac{(X_{\text{sim}})_i}{(X_{\text{true}})_i} \tag{4.17}$$

where n is the number of data; i is the i^{th} data; X is the model output value, e.g., the LPI or $(q_{c1N})_{\text{cs}}$ value in this chapter; X_{true} is the true LPI or $(q_{c1N})_{\text{cs}}$ value, and X_{sim} is the simulated or predicted value.

Smaller MAPE or RMSD value indicates a better model performance. For the bias factor, a value of greater than 1 means the model overestimates the true field, a value of less than 1 means an underestimation, and a value of 1 means an unbiased prediction. As discussed in the *Introduction* Section, the element size of the adopted investigation plans is larger than the synthetic digital field and the liquefaction potential field in XY plane. Therefore, an average operation is taken when the data from synthetic digital field and liquefaction potential field are used in the calculation of values of the MAPE, RMSD and bias factor.

Results and Discussions

Following the procedure of the above Section, results of random field-based liquefaction models by the averaged index approach, and the 2D and 3D local soil property approaches (M1, M2, and M3) are assessed and verified in this section. Unless otherwise stated, results of the random field-based liquefaction models are averaged over 1000 Monte Carlo simulations.

Model Assessment and Verification: Soil Property Fields

The histograms of the true and simulated $(q_{c1N})_{\text{cs}}$ values for both investigation plans

are plotted in Figure 4.7. The blue bins represent the true $(q_{c1N})_{cs}$ histogram, and the red dash lines and cyan dash-dot lines represent histogram fitting curves for simulated $(q_{c1N})_{cs}$ values using M2 and M3, respectively. It can be seen from Figure 4.7(a) that both random field models predict the statistical distribution of the true soil property field well, providing that sufficient field data (investigation plan #1) are available to infer model parameters. On the other hand, the model performance deteriorates for the case with insufficient field data (investigation plan #2), as shown in Figure 4.7(b). The differences between predictions using 2D (M2) and 3D (M3) local soil property approaches are almost negligible.

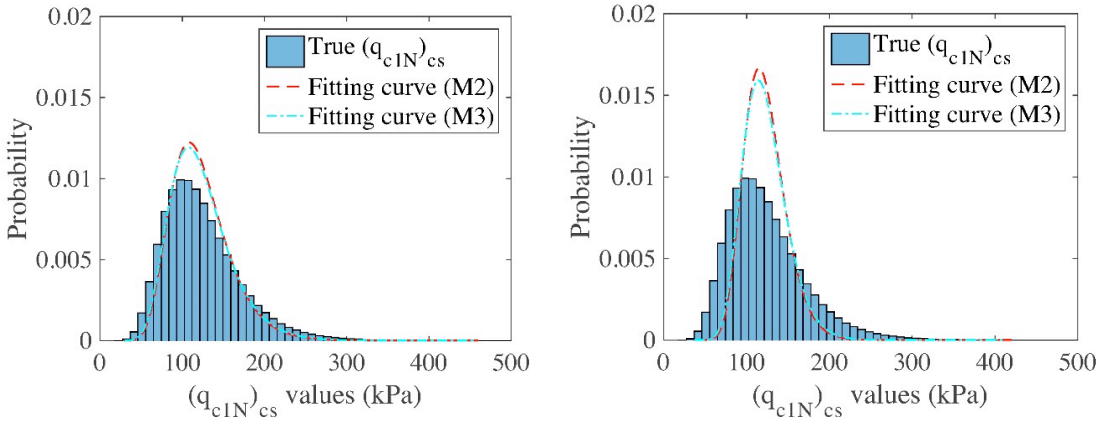

(a) Plan #1 (15 × 15) (b) Plan #2 (6 × 6)

Figure 4.7: The histograms of true and simulated $(q_{c1N})_{cs}$ fields of M2 and M3 for the both investigation plans.

The ability of random field models to capture the underlying spatial structure of the soil property field is also examined. Empirical semivariograms of the true $(q_{c1N})_{cs}$ field and the simulated $(q_{c1N})_{cs}$ fields are shown in Figure 4.8.

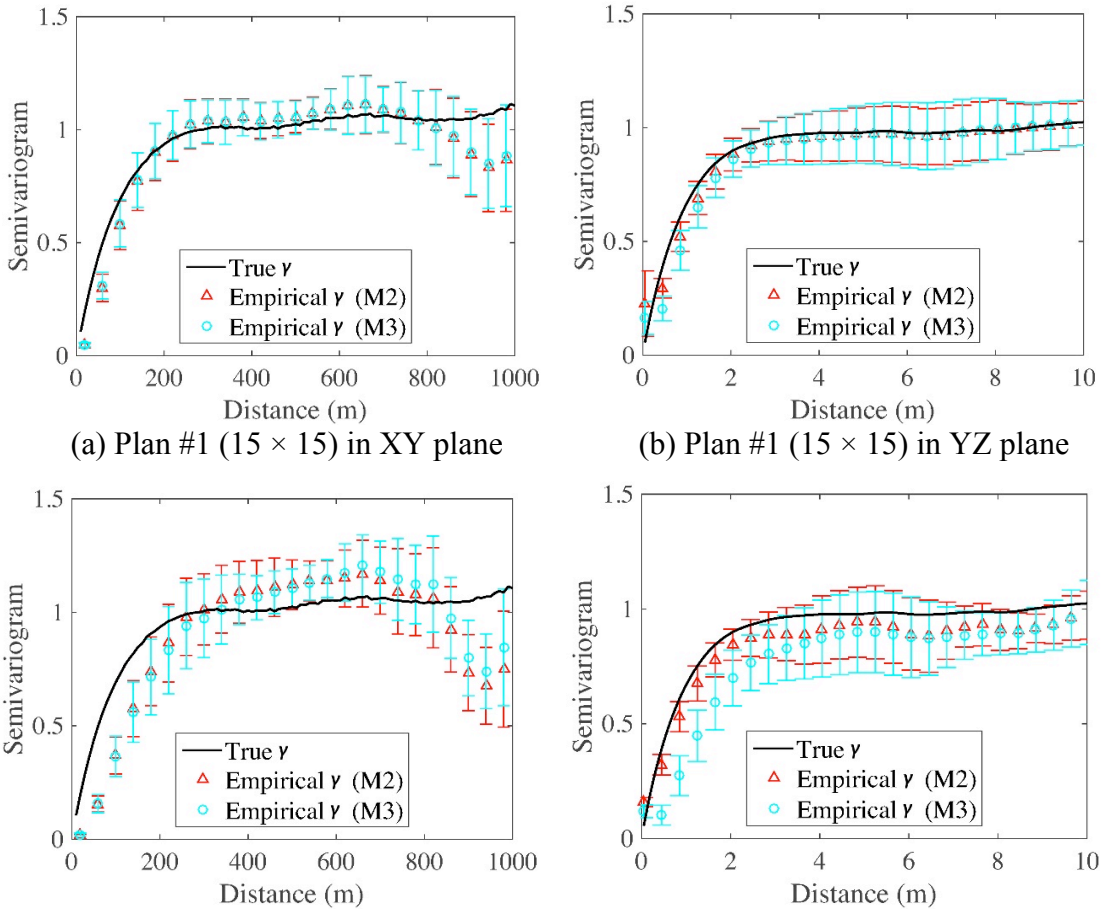

(a) Plan #1 (15 × 15) in XY plane

(b) Plan #1 (15 × 15) in YZ plane

(c) Plan #2 (6 × 6) in XY plane

(d) Plan #2 (6 × 6) in YZ plane

Figure 4.8: The semivariograms of true $(q_{c1N})_{cs}$ field and simulated $(q_{c1N})_{cs}$ fields of M2 and M3 for the both investigation plans.

The red triangles and cyan circles represent the mean values of the calculated empirical semivariograms by M2 and M3 in the XY plane and in the YZ plane, respectively. The error bars indicate ± one standard deviation from the mean. It can be seen from the plots that for investigation plan #1, both models capture the spatial structure of the soil property field well. For investigation plan #2, the semivariograms of M2 and M3 deviate from the trend of the true semivariogram, which is not surprising as insufficient data yield less accurate estimate of model parameters.

Figures 4.9(a) and 4.9(b) plot the $(q_{c1N})_{cs}$ profiles at selected locations (marked as point C, D and E in Figure 4.5) for investigation plans #1 and #2, respectively. It can be seen from Figure 4.9 that with sufficient sampling data (plan #1), the simulated $(q_{c1N})_{cs}$ profiles of M2 and M3 match the true profile very well. As the amount of sampling data decreases (plan #2), the $(q_{c1N})_{cs}$ profiles of M2 and M3 deviates from the true soil profile, indicating information loss and a reduction in the accuracy of predicted soil profiles.

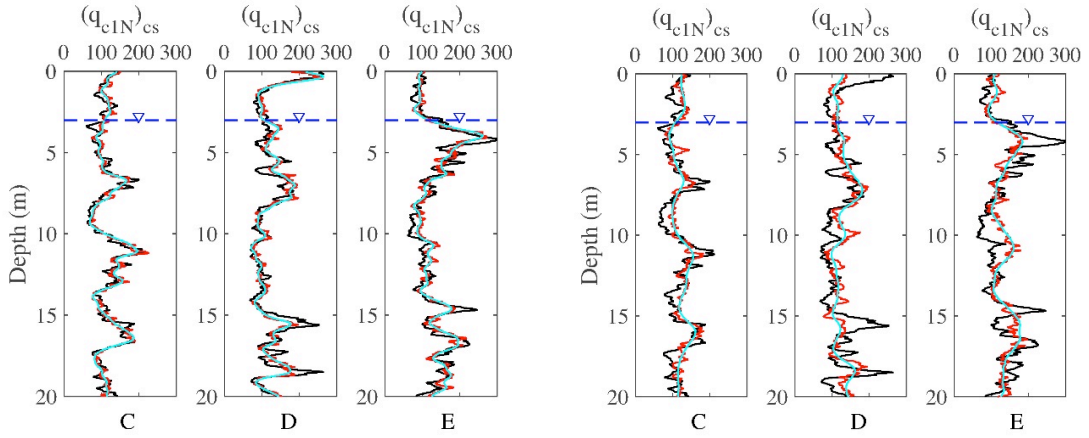

(a) Plan #1 (15 × 15) (b) Plan #2 (6 × 6)

Figure 4.9: The profiles of the true and simulated $(q_{c1N})_{cs}$ fields at the sampling locations C, D, and E marked in Figure 4.5 (the black, red and cyan lines correspond to the true $(q_{c1N})_{cs}$ profiles, the simulated $(q_{c1N})_{cs}$ profiles of M2 and M3, respectively).

To quantitatively assess model performances, the three measures introduced in Section of A*ssessment of model performance*, i.e., the MAPE, RMSD and the bias factor, are calculated and summarized in Table 4.2 for the simulated $(q_{c1N})_{cs}$ fields by the local soil property approaches (M2 and M3). Note that in the averaged index approach (M1), $(q_{c1N})_{cs}$ field is not needed and therefore, no result from M1 is presented in Table 4.2. Smaller MAPE and RMSD values mean better performance, and bias factor closer to one means more accurate model. MAPE and RMSD values for both local soil property

approaches (M2 and M3) are relatively small compared with the mean (123.98 kPa) and variance (2182.68) of the true field, which indicates a relatively good prediction. M3 performs slightly better than M2. For the bias factors, all model results yield slightly greater than one bias factor, which means the random field-based models slightly overpredict. The sampling size also affects the prediction accuracy, simulations with sufficient field data (plan #1) yield better results. For all cases considered, the 3D local soil property approach (M3) outperforms the 2D local soil property approach (M2).

Table 4.2: The criteria index for the $(q_{c1N})_{cs}$ random fields.

Index	Approach 1 (M1)		Approach 2 (M2)		Approach 3 (M3)	
	Plan #1	Plan #2	Plan #1	Plan #2	Plan #1	Plan #2
MAPE	NA	NA	0.147	0.238	0.136	0.226
RMSD	NA	NA	24.569	36.480	22.887	35.157
Bias factor	NA	NA	1.029	1.071	1.024	1.066

Note: NA means not available

Model Assessment and Verification: Liquefaction Potential Fields

In this section, the LPI fields predicted using random field-based approaches are assessed and verified.

Figure 4.10 plots the histograms of the true and simulated LPI fields. All of the random field-based liquefaction models perform well for investigation plan #1 as the histogram fitting curves of M1, M2 and M3 are close to the true LPI histogram. The prediction accuracy decreases with the reduction in sample size, as indicated by Figure 4.10(b).

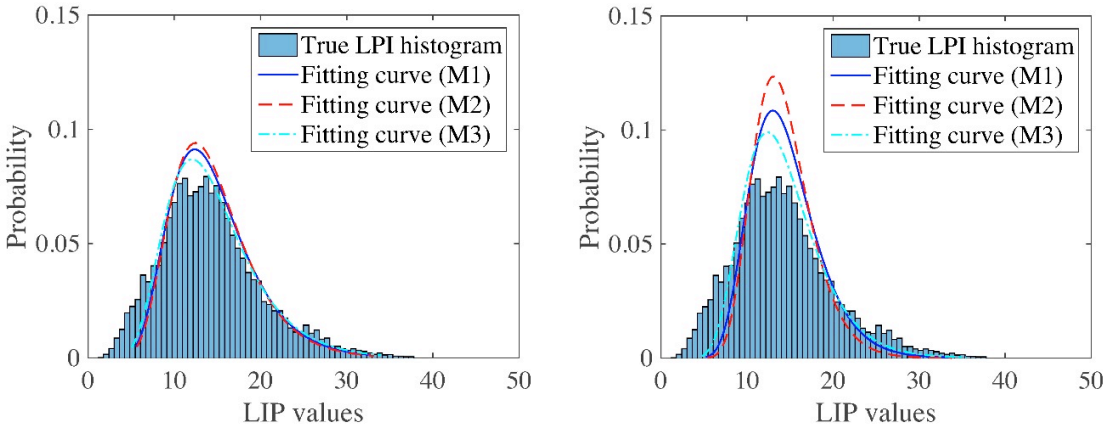

(a) Plan #1 (15 × 15) (b) Plan #2 (6 × 6)

Figure 4.10: The histograms of the true LPI field and simulated LPI fields of M1, M2 and M3 for the both investigation plans.

The semivariogram for simulations with investigation plan #1 and plan #2 are shown in Figures 4.11(a) and 4.11(b), respectively. The blue squares, red triangles and cyan circles represent the mean values of the calculated empirical semivariograms by M1, M2 and M3, respectively. The error bars indicate ±one standard deviation from the mean. It shows that the semivariograms of M1, M2 and M3 are very close to the true empirical semivariograms using sufficient samples (investigation plan #1). The variability increased when the distance of semivariogram is greater than 800 m as evidenced by longer error bars. However, the use of insufficient samples (plan #2) yields significant differences between the results of the three models and true empirical semivariograms.

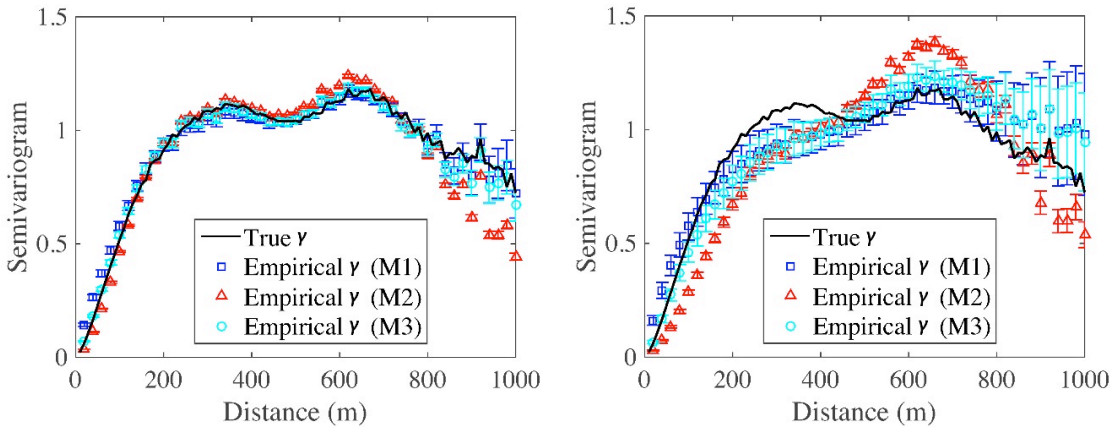

(a) Plan #1 (15 × 15) (b) Plan #2 (6 × 6)

Figure 4.11: The semivariograms of the true LPI field and simulated LPI fields of M1, M2 and M3 for the both investigation plans.

The performances of random field-based liquefaction models throughout the studied site are next analyzed with the cumulative frequencies shown in Figure 4.12. From Figure 4.12, it can be seen that the cumulative frequencies of M1 and M3 are very close to the true ones for both investigation plans. The model performance of M2 is worse than M1 and M3, especially under the insufficient test samples, as shown in Figure 4.12(b). With severity class of liquefaction defined in Table 4.1, it is possible to estimate the percentage of the studied site that may experience a particular level of liquefaction damage. For instance, from Figure 4.12(a), 96% of the studied site may experience a moderate to high liquefaction (LPI > 5) and 37% may experience a very high liquefaction (LPI > 15).

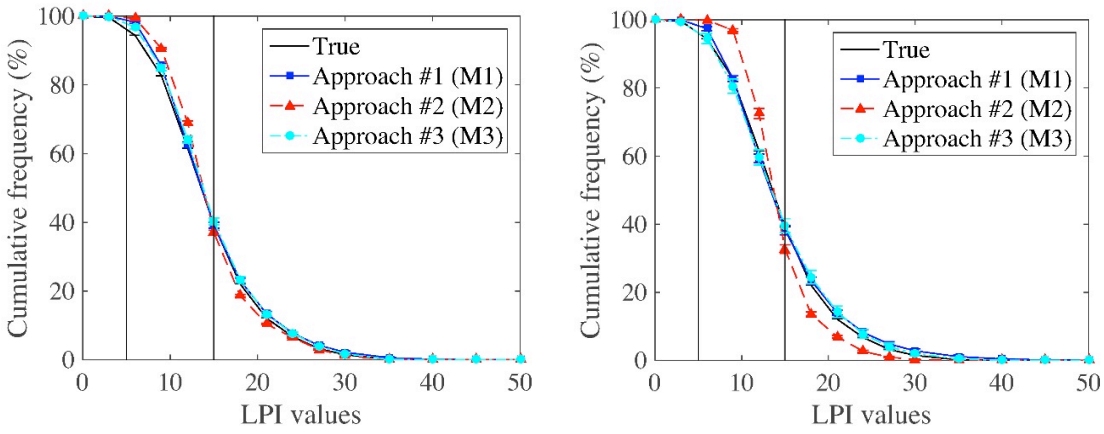

(a) Plan #1 (15 × 15) (b) Plan #2 (6 × 6)

Figure 4.12: The cumulative frequency of the true LPI field and simulated LPI fields of M1, M2 and M3 for the both investigation plans.

The contours in Figure 4.13 are the differences between the simulated LPI values of M1, M2 and M3 and the true LPI values. The red color represents an overestimation, blue color represents an underestimation and green color represents an unbiased prediction. Observations of the contours clearly reveal that for investigation plan #1, most of the areas are within the unbiased or little bias region, indicating good model performances of the three random field models. Over- and underestimations happen mostly around the edges of the field due to a lack of sampling data. Again, the reduction of the sample size increases the bias of the prediction, as indicated by the contours corresponding to simulations with plan #2 data.

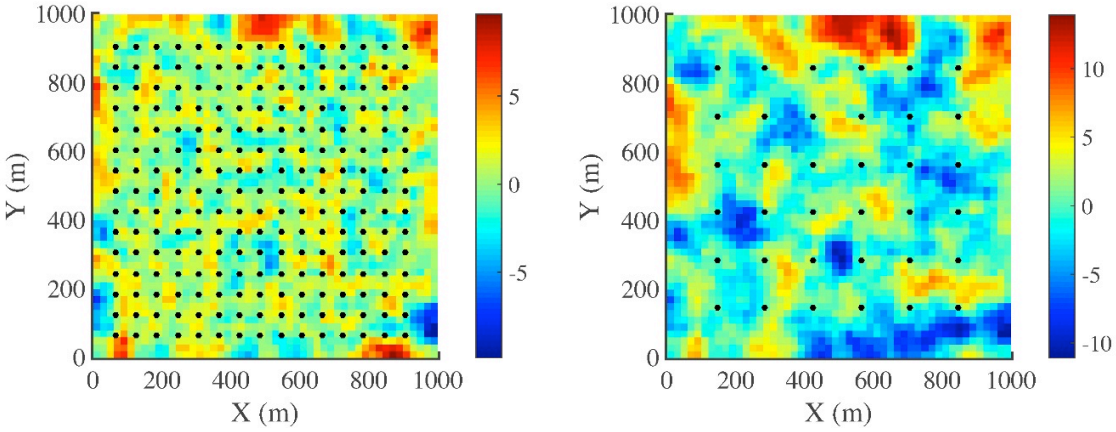

(a) M1, plan #1

(b) M1, plan #2

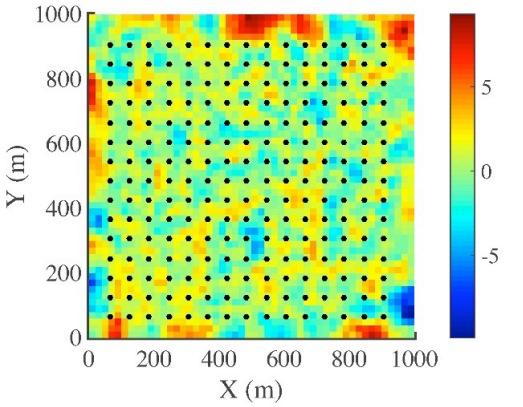

(c) M2, plan #1

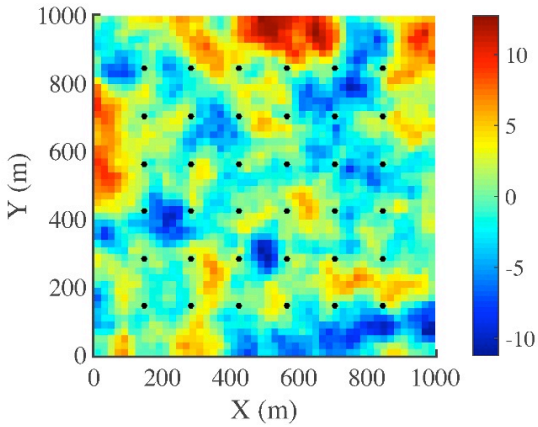

(d) M2, plan #2

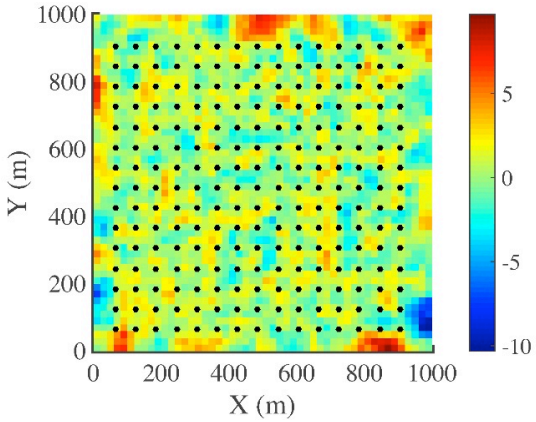

(e) M3, plan #1

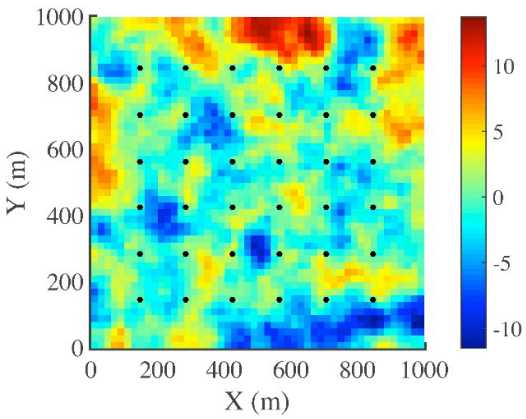

(f) M3, plan #2

Figure 4.13: Contours of the simulated LPI values (LPI_{sim}) of M1, M2 and M3 minus true LPI values (LPI_{true}) for the both investigation plans.

To further examine the model performances, a set of scatter plots for true LPI values

(LPI_{true}) versus simulated LPI values (LPI_{sim}) of M1, M2 and M3 for the both investigation plans are shown in Figure 4.14. The data for investigation plan #1 are concentrated around 1:1 line, while many variabilities observed in the data for investigation plan #2. All of the three the random field models (M1, M2 and M3) overestimate the field at low LPI values and underestimation at high LPI values. However, the over or under estimations are mainly located around edges of the field, which is similar to the trends observed in Figure 4.13.

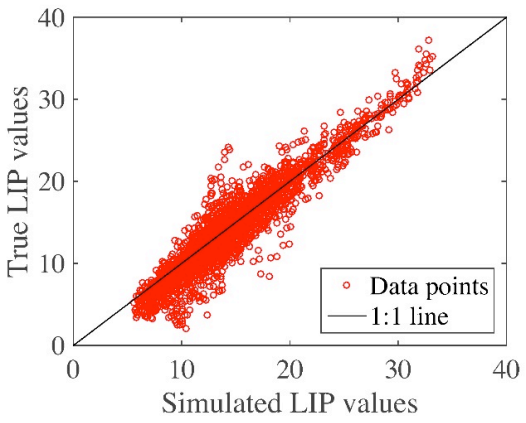

(a) M1, plan #1

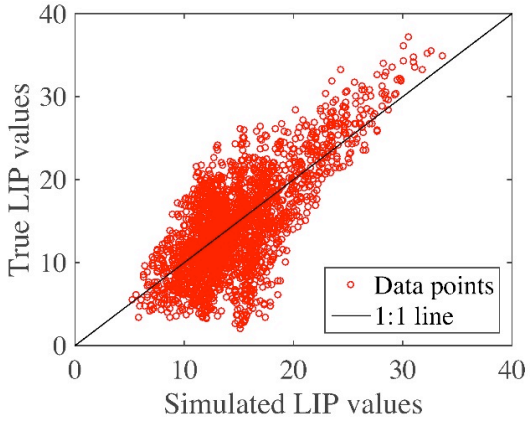

(b) M1, plan #2

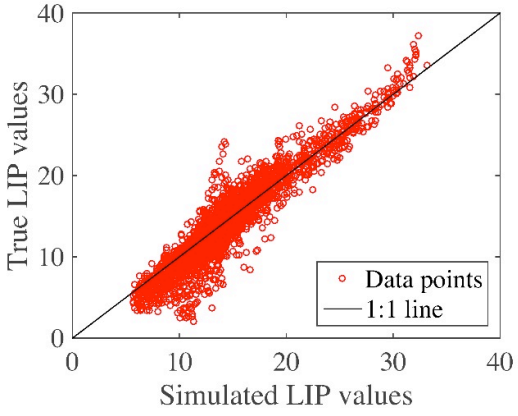

(c) M2, plan #1

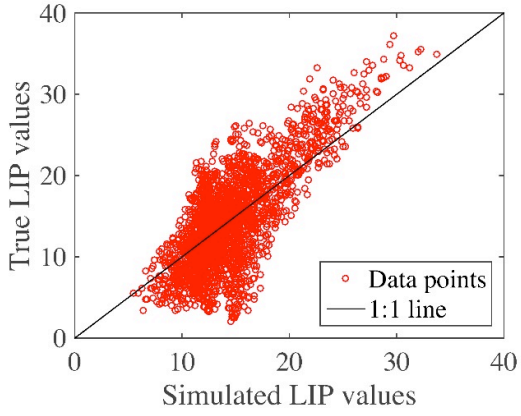

(d) M2, plan #2

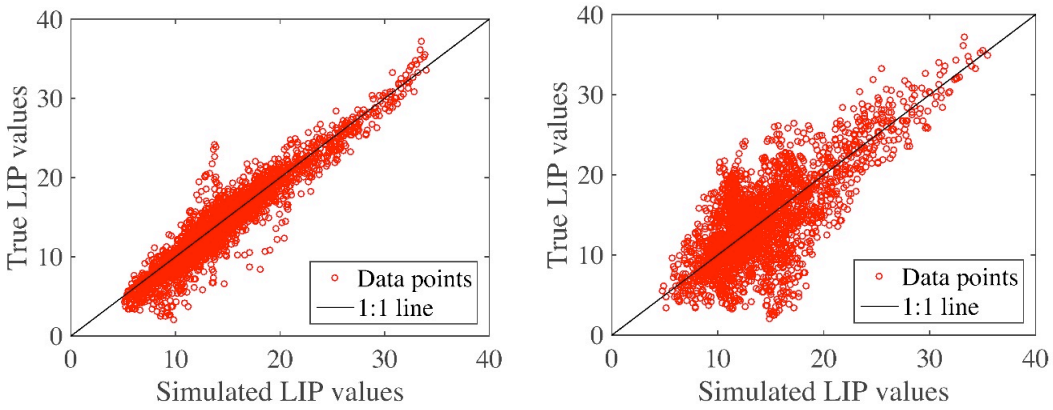

(e) M3, plan #1 (f) M3, plan #2

Figure 4.14: The true LPI values (LPI_{true}) versus simulated LPI values (LPI_{sim}) of M1, M2 and M3 for the both investigation plans.

The model performances of LPI field are also quantitatively assessed with the MAPE, RMSD and bias factor. The calculated indices for M1, M2 and M3 are summarized in Table 4.3. All three models predict relatively accurate LPI values over the entire field when the data from plan #1 are used. The M3 outperforms M1, and the latter outperforms M2. All three approaches slightly overestimate the LPI field as the bias factors are all greater than one. When the number of test samples are insufficient (Plan #2), the model performances based on MAPE and bias factor are M3 (best), M2 (second), and M1 (worst). By RMSD, however, M2 (3.876) is slightly better than M3 (3.897) and better than M1 (3.965). It indicates that the local soil property approach (M2 and M3) is superior to the averaged index approach (M1) in predicting the liquefaction potential field when the sampling data is insufficient.

The computational efficiency of a model is also of concern when evaluating the model performance. The computational time required for obtaining the 1000 LPI random fields based on investigation plan #2 are 4.5 mins, 1090.6 mins, and 5237.4 mins for M1,

M2 and M3, respectively. These numbers are meaningful only on a relative basis, as they depend on the computer used in the computation. The averaged index approach (M1) dominates in terms of computational efficiency and would be the clear choice when computational cost is of major concern.

Table 4.3: The criteria index for the LPI random fields.

Index	Approach 1 (M1)		Approach 2 (M2)		Approach 3 (M3)	
	Plan #1	Plan #2	Plan #1	Plan #2	Plan #1	Plan #2
MAPE	0.146	0.300	0.150	0.293	0.130	0.285
RMSD	2.030	3.965	2.047	3.876	1.878	3.897
Bias factor	1.085	1.151	1.088	1.138	1.070	1.120

Based on the comparisons of the accuracy criteria and the computational efficiency, M3 outperforms M2 in predicting the local soil property field, but M2 is more efficient than M3 in both scenarios of sufficient and insufficient test samples. For the liquefaction potential field, M3 performs better than M1 than M2 given the sufficient test samples. However, the performance of M1 is similar to M3 when the comparisons are based on histogram, semivariogram and cumulative frequency. In addition, M1 is the most efficient random field model. Therefore, under the scenario of sufficient test samples, M1 is recommended for constructing the liquefaction potential field. Under the scenario of insufficient test samples, however, M3 is recommended as it is more accurate than M2, and offers more information than M1.

Discussions

In this work, data inference and model verification are carried out based on a synthetic digital soil field. The synthetic field affords us an extremely detailed

information on soil properties and a benchmark field for liquefaction potential. The focus of this work is on understanding and verifying different random field-based approaches for liquefaction potential mapping, and use of synthetic digital field in this fundamental study has distinctive advantages over any real-world site investigation data.

On the other hand, it is important to note the assumptions and limitations of the synthetic field and the associated model verification process when drawing conclusions from the analysis. For instance, in preparing the synthetic field and in generating random field models, stationarity of the random field is assumed. Soil properties are assumed to be isotropic on a horizontal plane and anisotropic on a vertical plane. In reality, non-stationary variations of soil properties are quite common. In addition, only evenly-spaced virtual field investigation plans are considered in this study, which simplifies the inference of random field model parameters. In real-world field investigations, unevenly spaced and/or clustered sampling locations are common in engineering practice. Further study to consider the effect of unevenly spaced and/or clustered sampling plans on the data inference and model verification processes and outcomes for random field-based liquefaction hazard mapping is warranted.

Summary

In this chapter, a three-dimensional synthetic digital soil field is artificially generated and used as a basis to assess and verify various random field-based models for liquefaction mapping. The liquefaction potential is assessed using a classical CPT-based liquefaction model, and the result is expressed in terms of the liquefaction potential index.

Three random field-based liquefaction models are assessed and verified, namely, the averaged index approach (M1), the two-dimension local soil property approach (M2), and the three-dimension local soil property approach (M3). Two virtual field testing plans are designed. Here, performances of the three models are evaluated in terms of resulting sample histograms, empirical semivariograms and are compared using three information theory-based criteria, i.e., the mean absolute percentage error (MAPE), the root mean square deviation (RMSD) and the bias factor. Results show that all random field-based models examined in the study yielded a slightly more conservative prediction of liquefaction potential over the studied field. All these models captured fairly well the benchmark liquefaction potentials in the studied field.

CHAPTER V[3]

MITIGATION OF LIQUEFACTION HAZARD BY DYNAMIC COMPACTION — A RANDOM FIELD PERSPECTIVE

Introduction

Soil liquefaction and liquefaction-induced damage to buildings, lifeline systems, and port facilities, have been widely observed in recent earthquakes, e.g., 1999 Chi-Chi earthquake, 2008 Sichuan earthquake, 2010 Chile earthquake, 2010-2011 New Zealand earthquakes, 2011 Tohoku earthquake, etc. For example, in 1999 Chi-Chi earthquake, soil liquefaction was one of the main causes to the buildings and infrastructures loss ranging from $20 billion to $30 billion (Uzarski and Arnold, 2001); and in the 2010-2011 New Zealand earthquakes, approximately half of the $30-billion losses were attributed to soil liquefaction (Cubrinovski et al., 2014). Mitigating liquefaction hazards is a significant part of the earthquake resistant design (Seed, 1981; Seed, 1982).

Dynamic compaction (DC) is one of the common ground improvement methods and has been successfully applied to strengthen many types of weak ground deposits, such as loose sands and silts, hydraulic fill deposits, and landfill deposits (Lukas, 1995). DC has

[3] A similar form of this chapter is under review: Shen, M., Juang, C. H., & Chen, Q. (2018). Mitigation of liquefaction hazard by dynamic compaction - A random field perspective.

also been found to be an effective technique to mitigate liquefaction hazards, as evidenced by the improved ground performance to resisting liquefaction during past earthquakes (Dise et al., 1994; Hausler and Koelling, 2004; Hausler and Sitar, 2001; Lee et al., 2001). Dynamic compaction reduces the risk of liquefaction hazards by densifying the soil, leading to increased liquefaction resistance. To evaluate the effect of dynamic compaction, in situ tests, such as cone penetration test (CPT), are usually conducted before and after DC. With CPT data and using deterministic liquefaction models (Robertson, 2009; Robertson and Wride, 1998), the liquefaction potential of soil at a CPT location before and after DC can be evaluated. However, the locations of CPT before and after DC in a ground improvement project may not match, often far away from each other, due to the local construction practice, project management style, and client requirements. This reduces the effectiveness of the conventional one-to-one comparison of the factor of safety (F_S) or liquefaction potential values before and after DC at a given CPT location. Furthermore, due to the complexity of the depositional history and environment, engineering properties of a soil often vary in the subsurface space from one point to another. Consequently, soils in some areas of a project site are much susceptible than the soils in other parts. Therefore, it is desirable to investigate and visualize the liquefaction potential of the entire site to aid in the design of DC and to assess the effectiveness of DC in mitigating the liquefaction hazard.

In the last two decades, geostatistical tools and random field theory have been applied to assessing and mapping liquefaction potential or hazards (Baise et al., 2006; Chen et al., 2016a; Chen et al., 2016b; Elkateb et al., 2003; Juang et al., 2017b; Lenz and Baise,

2007; Liu et al., 2016; Wang and Chen, 2017; Wang et al., 2017). The spatial variability and dependence of soil properties have long been recognized (Fenton and Vanmarcke, 1998; Onyejekwe et al., 2016; Popescu et al., 1997; Vanmarcke, 2010): soil properties measured at one location are more similar to those at neighboring locations than those further away. By drawing multiple random samples, the overall characteristics of the spatial variability and dependence and the uncertainties involved can be mathematically modeled with random fields. Random field modeling provides an effective approach to estimate liquefaction potential of soils at unsampled locations based on the characterized statistical distribution and spatial variability, thus permitting an effective mapping of liquefaction hazard over an area of interest. By visualizing and comparing the liquefaction hazard of the entire project site before and after DC that is enabled through the random field modeling approach, the effect and benefits of DC in the mitigation of liquefaction hazard can be easily demonstrated.

In this study, a dynamic compaction (DC) project with before and after CPT investigations for a reclaimed ground in Taiwan is adopted as an example to demonstrate the effectiveness of the proposed random field-based evaluation procedure. The location-specific liquefaction potential analysis using the deterministic (i.e., F_S-based) approach is firstly performed. Then, the areal liquefaction is assessed in terms of liquefaction potential index (LPI), followed by the random field modeling of LPI and the creation of the liquefaction hazard map of the study site. The effectiveness of DC in the mitigation of liquefaction hazard is demonstrated through visualization of this hazard at different ground shaking levels for both before and after DC.

Liquefaction Potential: from Location-Specific to Areal Analysis

In this section, the formulations for two liquefaction potential indicators, the factor of safety (F_S) against liquefaction and the liquefaction potential index (LPI), are first summarized in Section *Factor of safety (F_S) against liquefaction* and Section *Liquefaction potential index (LPI)*, respectively. The F_S-based liquefaction potential indicator is usually adopted in a location-specific analysis, in which an F_S profile along the depth can be created and used to identify the critical layer(s) that is susceptible to liquefaction at the sampling location. The LPI based liquefaction potential indicator is a single value at the sampling location that integrates weighted F_S values along the depth (Iwasaki et al., 1982). The random field modeling based on the LPI values at sampled locations is then presented in Section *Liquefaction mapping by random field modeling*. These formulations and modeling procedures provide the working knowledge for evaluating the liquefaction potential of soil from location-specific to areal perspective.

Factor of Safety (F_S) Against Liquefaction

Among methods for soil liquefaction potential evaluation, simplified methods based on *in situ* tests, such as standard penetration test (SPT), cone penetration test (CPT), and shear wave velocity (V_s) test, are preferred in geotechnical engineering practices (Andrus and Stokoe II, 2000; Robertson and Wride, 1998; Seed and Idriss, 1971; Youd et al., 2001). With the simplified methods, the factor of safety (F_S) against liquefaction is used to express the liquefaction potential. F_S is defined as the ratio of cyclic resistance ratio (CRR) over the cyclic stress ratio (CSR) as shown in Eq. (1). The soil is said to be

liquefied if $F_S \leq 1$ and be non-liquefied if $F_S > 1$.

$$F_S = \frac{\text{CRR}}{\text{CSR}} \tag{5.1}$$

The liquefaction resistance CRR is typically computed using the *in situ* test data. The CPT-based liquefaction model proposed by Robertson and Wride (1998) and subsequently updated by Robertson (2009) is adopted in this study to calculate the CRR, which is summarized in Eq. (2). The CRR is a function of the clean-sand equivalence of the normalized cone tip resistance, $q_{t1N,\text{cs}}$. The reader is referred to (Robertson, 2009; Robertson and Wride, 1998) for details regarding the evaluation of $q_{t1N,\text{cs}}$.

$$\text{CRR} = \begin{cases} 0.833[q_{t1N,\text{cs}}/1000] + 0.05 & \text{if} \quad q_{t1N,\text{cs}} < 50 \\ 93[q_{t1N,\text{cs}}/1000]^3 + 0.08 & \text{if} \quad 50 \leq q_{t1N,\text{cs}} < 160 \end{cases} \tag{5.2}$$

It should be noted that Eq. (2) is applicable only to soils with soil behavior type index I_c of no greater than 2.6. For a soil with $I_c > 2.6$, it is considered too clay-rich to liquefy, and CRR is set to a high value (in such case, however, the value of $q_{t1N,\text{cs}}$ is meaningless and by-passed in the evaluation of CRR). If $q_{t1N,\text{cs}} \geq 160$, CRR is also set to a high value, e.g., 1.0, indicating no liquefaction is expected under any known seismic loading.

The CSR represents the earthquake loading as applied to soil in the context of liquefaction, and the following adjusted form is adopted (Juang et al., 2006; Youd et al., 2001):

$$\text{CSR} = 0.65\,(\frac{a_{\max}}{\text{g}})\,(\frac{\sigma_{\text{vo}}}{\sigma'_{\text{vo}}})\,(r_d)\,(\frac{1}{\text{MSF}})\,(\frac{1}{K_\sigma}) \tag{5.3}$$

where $a_{\max}$ is the maximum horizontal acceleration at the ground surface; g is the

gravitational acceleration and equal to 9.81 m/s^2; σ_{vo} and σ'_{vo} are the total and effective vertical overburden stresses, respectively; r_d is the stress reduction factor; MSF is the magnitude scaling factor and K_σ is the overburden correction factor.

The stress reduction factor r_d is a function of depth z and defined below (Youd et al., 2001):

$$r_d = \frac{1.000 - 0.4113z^{0.5} + 0.04052z + 0.001753z^{1.5}}{1.000 - 0.4177z^{0.5} + 0.05729z - 0.006205z^{1.5} + 0.001210z^2} \tag{5.4}$$

The magnitude scaling factor MSF is related to the moment magnitude M_w as (Youd et al., 2001):

$$\text{MSF} = \frac{10^{2.24}}{M_w^{2.56}} \tag{5.5}$$

The K_σ in Eq. (6) is the overburden correction factor for CSR (Youd et al., 2001). The correction is applied when the σ'_{vo} greater than 100 kPa.

$$K_\sigma = \left(\frac{\sigma'_{vo}}{P_a}\right)^{(f-1)} \tag{5.6}$$

where P_a is the atmospheric pressure; f is an exponent and recommended as: f = 0.7 to 0.8 for relative densities between 40 and 60%; f = 0.6 to 0.7 for relative densities between 60 and 80%.

Liquefaction potential index (LPI)

The liquefaction potential index (LPI) defined by Sonmez (2003), which was originated by Iwasaki et al. (1982), is adopted in this study as the index for mapping the liquefaction hazard. LPI is defined based on the assumption that the liquefaction severity

is related to the thickness of the potentially liquefiable layers and the factor of safety (F_S) against liquefaction. LPI is defined as follows (Sonmez, 2003 after Iwasaki et al., 1982):

$$\mathrm{LPI} = \int_0^{20} w(z) F_L \mathrm{d}z \tag{5.7}$$

where z is the soil depth in meters (only the top 20 m of soil profile is considered); $w(z)$ is a function of soil depth; F_L is a function of F_S against liquefaction.

$$w(z) = 10 - 0.5z \tag{5.8}$$

$$F_L = \begin{cases} 0 & F_S \geq 1.2 \\ 1 - F_S & F_S \leq 0.95 \\ 2 \times 10^6 e^{-18.427 F_S} & 0.95 < F_S < 1.2 \end{cases} \tag{5.9}$$

Sonmez (2003) provided an updated significance scale, or severity class, for LPI values as shown in Table 5.1, with which the liquefaction severity at the location can be assessed.

Table 5.1: Classification of the Liquefaction Potential Index (Sonmez, 2003)

Class	Liquefaction potential index (LPI)	Severity class of liquefaction
1	LPI = 0	I: Non-liquefiable
2	0 < LPI ≤ 2	II: Low
3	2 < LPI ≤ 5	III: Moderate
4	5 < LPI ≤ 15	IV: High
5	LPI > 15	V: Very high

Liquefaction Mapping by Random Field Modeling

As indicated by Toprak and Holzer (2003), LPI provides a convenient tool for risk-based decisions and liquefaction hazard mapping. Focusing on how spatial variability and

dependence are considered and incorporated in the liquefaction mapping process, three approaches may be used to generate LPI hazard map (Juang et al., 2017b). They are the averaged index approach, the two-dimensional (2D) local soil property approach, and the three-dimensional (3D) local soil property approach. The averaged index approach is adopted in this chapter as it is widely used in current liquefaction hazard mapping studies (Baise et al., 2006; Bong and Stuedlein, 2017; Bong and Stuedlein, 2018; Chen et al., 2016a; Lenz and Baise, 2007; Wang and Chen, 2017; Wang et al., 2017), and it is the most computationally efficient among the three approaches. In the averaged index approach, the probability distribution and the spatial dependence of LPI values at the test locations are characterized and used as inputs for random field modeling. The probability distribution can be easily inferred from test data. The LPI values at the test locations are fitted to a lognormal distribution, thus ln(LPI) will be used in the characterization of spatial dependence and the random field simulation process, which are introduced as follow.

Spatial characterization of LPI

In this study, spatial dependence or spatial variation structure is described using a form of covariance known as the semivariogram γ, which is equal to one half of the variance of two variables separated by a vector distance $\boldsymbol{h}$:

$$\gamma(\boldsymbol{h}) = \frac{1}{2}\mathrm{Var}[Z(\boldsymbol{u}) - Z(\boldsymbol{u}+\boldsymbol{h})] \tag{5.10}$$

where $Z(\boldsymbol{u})$ and $Z(\boldsymbol{u}+\boldsymbol{h})$ are the values of the variable (i.e., ln(LPI) in this study) under consideration at locations $\boldsymbol{u}$ and $\boldsymbol{u}+\boldsymbol{h}$, respectively. A scalar form of the vector distance $\boldsymbol{h}$,

denoted as h, is commonly used to account for both separation distance and orientation (e.g., Chen et al., 2012), and therefore can be used to simulate anisotropic random fields:

$$h = \sqrt{\left(\frac{h_x}{a_x}\right)^2 + \left(\frac{h_y}{a_y}\right)^2 + \left(\frac{h_z}{a_z}\right)^2} \tag{5.11}$$

where h_x, h_y and h_z are the scalar components of the vector distance along the principal axes of the field; and a_x, a_y and a_z specify how quickly the spatial dependences decrease along the respective axes. The LPI random field studied in this chapter is two-dimensional, thus $h_z = 0$. Further, the ln(LPI) is assumed to be anisotropic in x and y axes thus $a_x = a_y$.

Sequential simulation process

To generate random field realizations of the variables of interest, a conditional sequential Gaussian simulation method (e.g., Goovaerts, 1997; Baker and Faber 2008; Baker et al., 2011) is implemented, which has been extensively used by mining scientists and geostatisticians for natural resource evaluations and spatial predictions of geohazards. Following the sequential simulation method, the simulation process could be briefly described as

$$(Z_n \,|\, \boldsymbol{Z}_p = \boldsymbol{z}) \sim N(\Sigma_{np} \cdot \Sigma_{pp}^{-1} \cdot z, \sigma_n^2 - \Sigma_{np} \cdot \Sigma_{pp}^{-1} \cdot \Sigma_{pn}) \tag{5.12}$$

in which the unknown value, Z_n, at an unsampled location n is drawn from the conditional normal distribution with the mean $(\Sigma_{np} \cdot \Sigma_{pp}^{-1} \cdot z)$ and the variance $(\sigma_n^2 - \Sigma_{np} \cdot \Sigma_{pp}^{-1} \cdot \Sigma_{pn})$. It is noted here that $\Sigma_{np} \cdot \Sigma_{pp}^{-1}$ are essentially the weights assigned in the simple Kriging process (Goovaerts, 1997); $\boldsymbol{Z}_p$ is the vector of known data; Σ is the

covariance matrix of neighboring measurements; the subscriptions p and n mean "previous" and "next", respectively. For the realization, one value of $\boldsymbol{Z}_n$ is drawn at random from the posterior univariate normal distribution. Once the unknown value Z_n is generated, it is inserted into the "previous" vector, i.e., the known data vector $\boldsymbol{Z}_p$, upon which the "next" unknown value at another un-sampled location will be generated. Detailed process of random field modeling may be found in Chen et al. (2015) and Wang et al. (2017).

Random field models incorporate the spatial dependence of the measured parameter through the covariance matrix. The covariance of values at two separated locations could be expressed as

$$\Sigma = \mathrm{cov}[Z_i, Z_j] = \rho_{Z_i,Z_j} \cdot \sigma_{Z_i} \cdot \sigma_{Z_j} \tag{5.13}$$

where $\mathrm{cov}[Z_i, Z_j]$ is the covariance of the random variables Z_i and Z_j, and ρ_{Z_i,Z_j} is the correlation coefficient between the random variables Z_i and Z_j with standard deviations of σ_{Z_i} and σ_{Z_j}, respectively. The correlation coefficient ρ is used to describe the similarity of spatial measurements and is related to the semivariogram γ by

$$\rho(h) = 1 - \gamma(h) \tag{5.14}$$

The semivariogram γ can be calculated using Eq. (5.10), which is termed empirical γ (i.e., experimental semivariogram) herein. Then the empirical γ is fitted with a theoretical model, such as spherical, exponential, Gaussian or power model (Goovaerts, 1997), to determine three model parameters, including nugget effect, sill, and range. The exponential semivariogram model is adopted and expressed as

$$\gamma(h) = \omega[1 - \exp(\frac{h}{a})] + \tau \tag{5.15}$$

where τ presents the nugget, i.e., the semivariance when h equals zero; $\omega + \tau$ is the sill, namely the constant semivariance when h is greater than the range, indicated by $3a$. It is noted here that the nugget effect is a geostatistical term used to describe the variability seen between samples that are closely spaced. The nugget effect is composed of a geological component, which can be thought of as inherent, and a sampling component, which is subjected to randomness.

Once the semivariogram γ is characterized, it will be plugged into the covariance matrix Eq. (5.13) through Eq. (5.14). Thus, the unknown value Z_n (i.e., ln(LPI) in this study) at location n could be drawn using Eq. (5.12). The generated value is then assigned to location n and treated as known data. This process is repeated until all the unsampled locations are assigned with values. Each sequential Gaussian simulation realization varies in space, although it is conditional on observed samples. Thus, Monte Carlo simulations (MCSs) will be used to generate realizations of the ln(LPI) random fields, then the results will be transformed back to lognormal distribution, which are used for the probabilistic and spatial assessment of LPI evaluation over the area of interest.

Location-specific Liquefaction Potential Analysis

In this section, the site conditions and dynamic compaction at the study site are first introduced. Then, two CPT samples are used as an example to illustrate the location-specific liquefaction potential analysis.

Site Conditions

The location of the study site is shown in Figure 5.1, and the size of the study site is 2000 m × 800 m. It is located in the Lukang district of the Chang-Hwa Coastal Industrial Park (CHCIP) on the west coast of central Taiwan, where a large-scale land reclamation project was completed. As described in Lee et al. (2001) and Shen et al. (2018), the CHCIP area is an extension of the recent alluvial plains (Qa) of the Changhua County. The alluvium forms the flood plains and recent terraces of the larger streams that dissect the island. The alluvium also includes coastal sand dunes, recent lacustrine and swamp deposits, and cave deposits in limestone terrain (Ho, 1988). The study site was reclaimed by hydraulic filling. The filling material comes from sediments under the waterways and the sea, which consists mainly of silty sand to fine sand. The thickness of the hydraulic fill is approximately 4 to 5 m. A backfill of gravel of approximately 0.2 m is placed over the hydraulic fill. From the soil profiles that were derived through the standard penetration tests (SPTs), within the top 20 m, the site mainly consists of silty sands (SM or SP–SM according to the Unified Soil Classification System) with thin layers of silts (ML) or silty clays (CL).

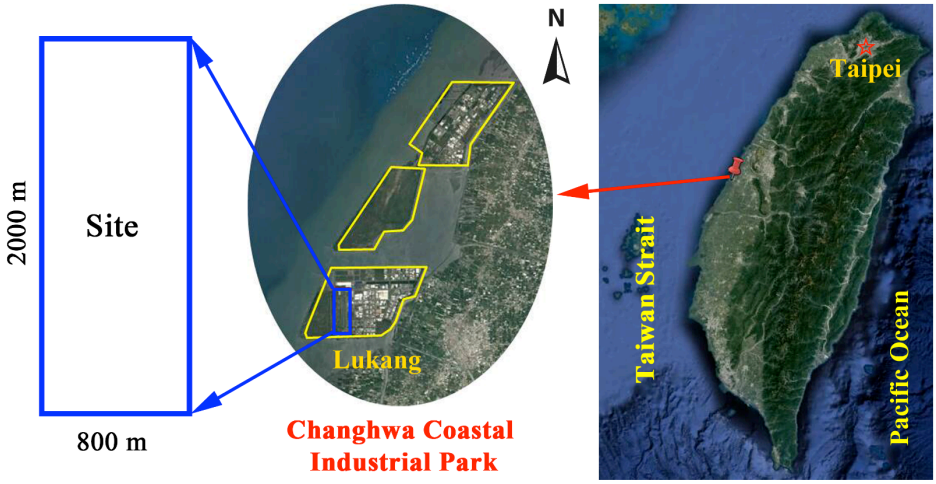

Figure 5.1: Location of the study site.

Dynamic Compaction at the Site

The study site is located in the seismic zone II according to the seismic design specifications for highway bridges (Ministry of Communication 1996), which specifies the earthquake seismic loading defined by a maximum horizontal acceleration at the ground surface a_{max} of 0.23g and a moment magnitude M_w of 7.5 based on a return period of 475 years.

The loose sand in the upper layer of the study site was considered to have high potential to liquefy when subjected to the design earthquake (Lee et al., 2001). Thus, a ground improvement project through dynamic compaction (DC) was undertaken at the study site to mitigate the liquefaction hazard. The reader is referred to the literature (e.g., Lukas 1995; Han 2015) for details of the DC technique. In the study area, DC was carried out with a main pounder that weighed 25 tons, which had a base area of 3 m^2 and a drop

height of 20 m. The sequence of DC with the main ponder is illustrated in Figure 5.2 with three passes in a subzone of 10 m by 10 m. After the completion of DC with the main pounder, the craters and surrounding soils were leveled and the surface tamped with a smaller pounder that weighted 12 tons and had a base area of 6 m^2 and a drop height of 10 m.

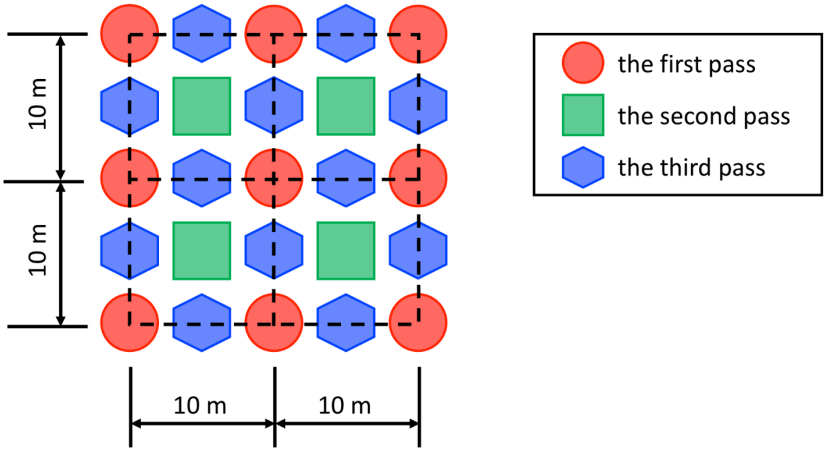

Figure 5.2: Dynamic compaction in each zone in three passes.

Before DC, 27 cone penetration tests, denoted as CPT_{BC}, were conducted over the entire site to investigate the soil properties. After the DC, additional 27 cone penetration tests, denoted as CPT_{AC}, were performed again at the locations near the CPT_{BC} to estimate the effect of dynamic compaction. Figure 5.3 shows the layout of the CPT tests both before and after the compaction. The coordinates of the 27 CPT_{BC} and CPT_{AC} are listed in Table 5.2 and Table 5.3, respectively. It can be seen from Figure 5.3 that the 27 CPT_{BC} and CPT_{AC} spread over the study area, which affords the evaluation of liquefaction potential for the entire study area. Next, the location-specific liquefaction

potential analysis is performed to illustrate the use of the traditional deterministic method.

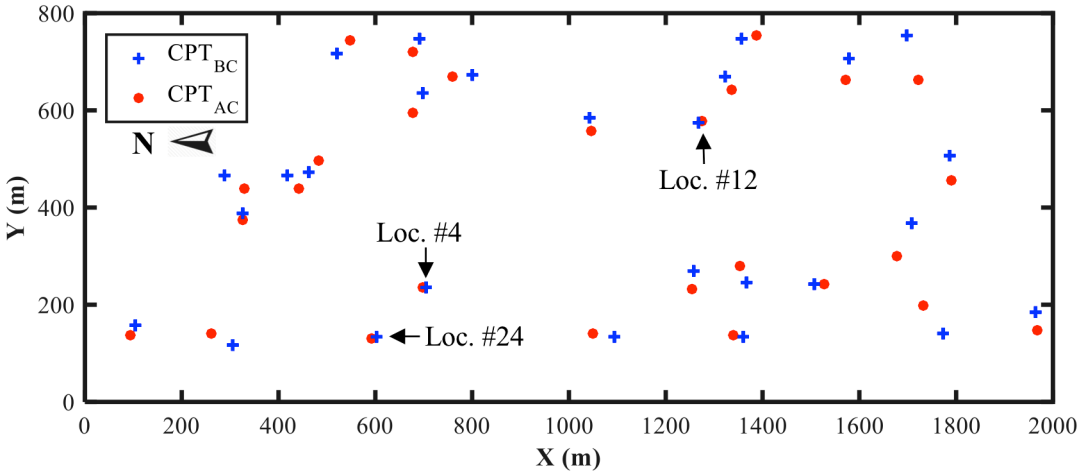

Figure 5.3: Layout of the CPT investigations before compaction (CPT_{BC}) and after compaction (CPT_{AC}). (Note: locations marked are used for location-specific liquefaction analysis).

Table 5.2: Locations of 27 CPT soundings at the project site before compaction (CPT_{BC}) and its LPI values (LPI_{BC}) under two seismic shaking levels.

CPT_{BC} No.	Before Compaction (BC)		LPI_{BC}	
	X_{BC} (m)	Y_{BC} (m)	Design earthquake	Chi-Chi earthquake
1	1358	749	12.5	1.1
2	1788	508	18.6	1.8
3	1366	247	18.9	2.0
4	706	236	11.6	3.8
5	288	465	20.2	2.3
6	690	748	12.0	0.6
7	697	635	12.8	0.5
8	417	466	19.8	2.6
9	307	117	12.4	0.4
10	1774	139	14.1	1.4
11	1708	369	15.5	2.7
12	1268	573	21.6	5.8
13	1699	753	14.8	1.1

14	1580	708	17.0	1.8
15	1507	242	17.9	1.7
16	1963	184	24.0	7.7
17	1321	670	11.2	0.9
18	1043	586	12.6	0.9
19	801	672	12.7	0.7
20	521	718	14.3	0.5
21	326	387	14.5	0.7
22	464	474	16.3	0.8
23	103	159	15.2	0.3
24	603	133	10.1	1.5
25	1095	134	14.2	0.4
26	1258	269	20.7	5.7
27	1359	133	22.0	6.2

Table 5.3: Locations of 27 CPT soundings at the project site after compaction (CPT_{AC}) and its LPI values (LPI_{AC}) under two seismic shaking levels.

CPT_{AC} No.	After Compaction (AC)		LPI_{AC}	
	X_{AC} (m)	Y_{AC} (m)	Design earthquake	Chi-Chi earthquake
1	1387	753	2.0	0.00382
2	1790	457	1.7	0.00381
3	1352	278	3.2	0.34916
4	698	237	1.8	0.40665
5	329	438	6.3	0.08327
6	677	722	0.7	0.00000
7	677	596	4.9	0.02116
8	442	440	3.0	0.00508
9	262	139	3.7	0.03093
10	1732	198	1.9	0.00000
11	1679	299	3.1	0.15454
12	1274	578	5.4	0.85594
13	1722	662	4.4	0.00407
14	1573	662	1.8	0.00082
15	1529	242	2.7	0.00797
16	1967	147	2.0	0.00470
17	1336	644	3.2	0.07942
18	1045	558	2.6	0.00224
19	761	671	1.4	0.00000
20	548	744	2.1	0.02032
21	327	376	4.2	0.07450
22	482	497	3.5	0.00265

23	95	136	2.8	0.01370
24	592	131	11.1	2.35815
25	1051	140	3.7	0.02302
26	1254	233	3.0	0.01693
27	1339	137	7.7	0.26813

Location-specific Liquefaction Potential Analysis

To calculate the factor of safety (F_S) against liquefaction, the following set of input data is adopted for the CPT-based liquefaction model: the moist unit weight of the soil γ_m is 16 KN/m^3, the saturated unit weight γ_{sat} is 19 KN/m^3, and the groundwater table (GWT) in the study site is observed at 2 m below the ground surface. The design earthquake at the study site is adopted as the level of seismic loading: a_{max} = 0.23 g and M_w = 7.5.

Figure 5.4(a) shows the location-specific F_S-based liquefaction analysis at location #4 (marked in the layout in Figure 5.3). The first subplot of Figure 5.4(a) is the profiles of $q_{t1N,cs}$ before compaction (BC) and after compaction (AC), which clearly shows the increase in soil strength over the depths between 1 m and 8 m. Below the depth of 8 m, there was little change in the soil strength. It can be seen that DC tends to disturb and loosen the top layers (top 1 m) even though it compacts the deeper layers (up to 8 m). The second subplot of Figure 5.4(a) shows the CSR and CRR profiles along the depth for both BC and AC. It can be seen that before DC, the CRR is much smaller than CSR between the depths of 2 m and 5 m, which is the critical layer of soil liquefaction at the location #4. Within the critical layer, there were very thin layers of non-liquefiable clay material, which is reflected by the abrupt change of CRR in

these very thin layers. If these noises (exhibited in these very thin layers) are ignored, the critical layer is easily identified. Below the depth of 6.5 m, there exists a layer of clayey silt and silty sand mixtures (Lee et al., 2001), which is deemed non-liquefiable (assigned herein with CRR = 1), although the $q_{t1N,\mathrm{cs}}$ values are very low. After DC, the CRR is greatly increased, especially in the critical layer. The third subplot of Figure 5.4(a) shows the F_S profiles of BC and AC, and the effect of DC in the increase of F_S, especially in the critical layer, is evidenced.

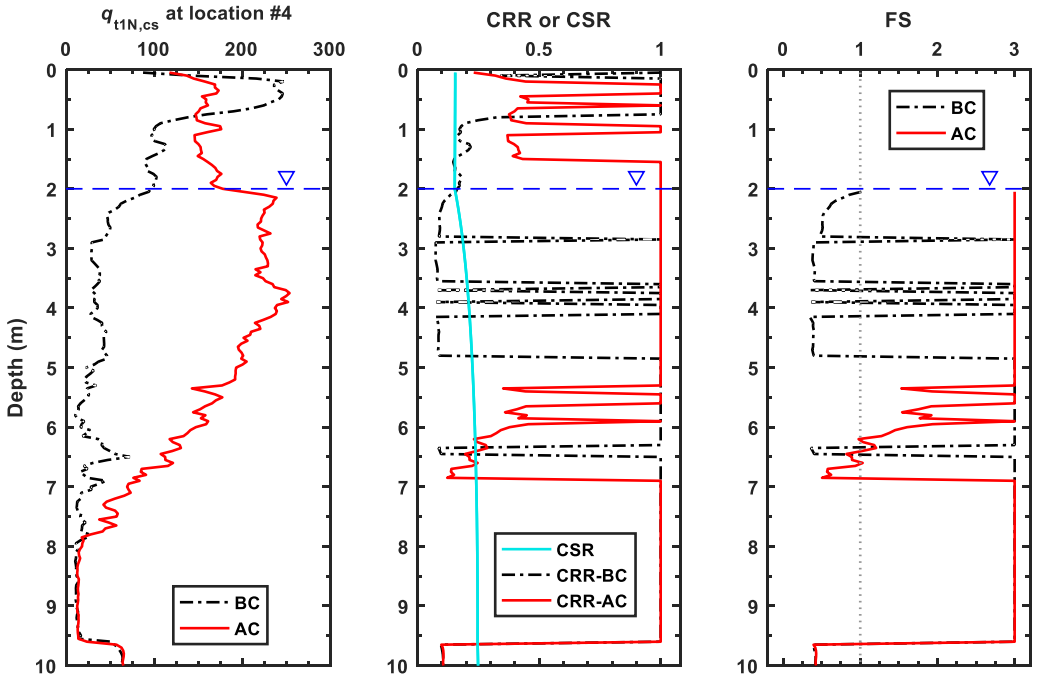

(a)

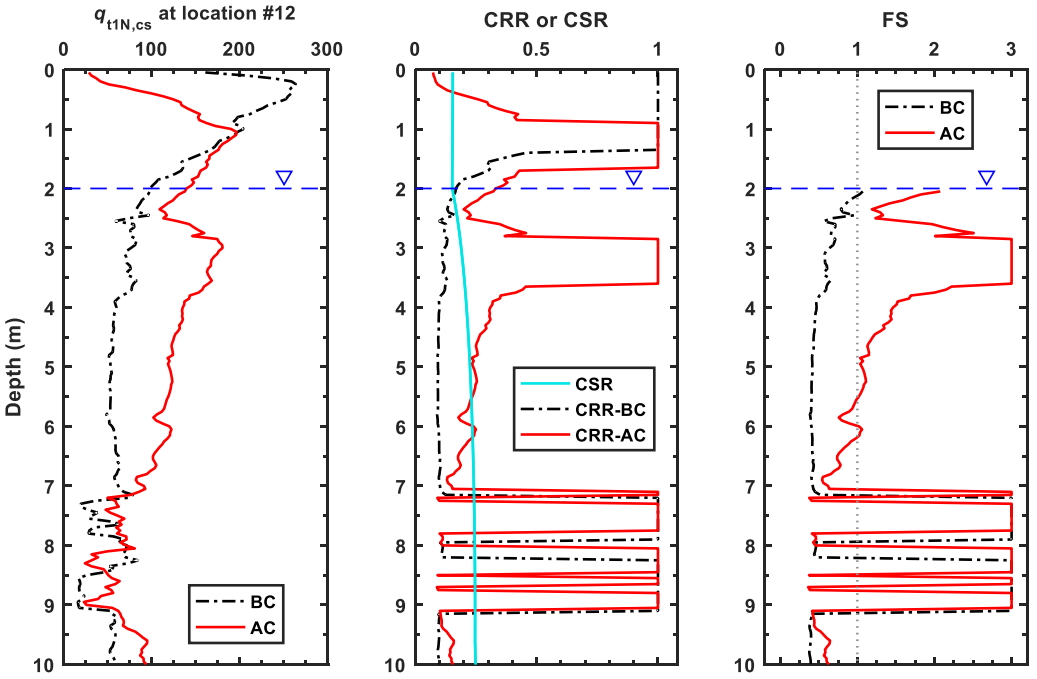

(b)

Figure 5.4: Location-specific liquefaction potential analysis at (a) location #4; (b) location #12 under the shaking level of the design earthquake.

Figure 5.4(b) shows the location-specific F_S-based liquefaction analysis at location #12 (marked in the layout in Figure 5.3). It can be inferred from the third subplot of Figure 5.4(b), the critical layer at this location is between the depths of 2 m and 7 m based on the F_S profile before DC. After DC, the liquefaction potential at this location has been reduced virtually to zero (i.e., $F_S > 1$) within the first 5 m from the ground surface. However, the DC is not effective when the depth is greater than 5 m under the shaking level of the design earthquake. In short, based on the results shown in Figure 5.4, the liquefaction potential at one location varies from the other due in part to the spatial variation of the natural deposit and the depositional variation of the hydraulic fill.

It should be noted that the distances between CPT_{BC} and CPT_{AC} at both location # 4 and location #12 are approximately 8 m. The distance between CPT_{BC} and CPT_{AC} can affect the accuracy of comparison of their liquefaction resistance. As can be seen from the data shown in Table 5.2 and Table 5.3, the distance between each pair of CPT_{BC} and CPT_{AC} is in a range of 8 m to 94 m with an average of 37 m. This may lead to an inaccurate evaluation of the effect of DC using the location-specific liquefaction potential analysis as presented previously. This problem may be overcome by adopting the areal liquefaction potential analysis through the use of random field modeling, which will be introduced in the next section.

Areal Liquefaction Potential Analysis

To improve the communication of the effect of DC between the engineers, contractors and clients, the visualization of the liquefaction potential at a project site that covers a significant area is conceptually attractive. To visualize the liquefaction potential in the project area under a given earthquake-shaking scenario, random field modeling of the LPI field is performed. In addition, through the generated LPI maps before and after DC, the effect of DC over the entire study site can be evaluated.

The LPI Hazard Map Generated by Random Field Modeling

The shaking level of the design earthquake at the DC project site is adopted in the liquefaction analysis discussed in this section. Firstly, the LPI values of the 27 CPT samples before compaction, denoted as LPI_{BC}, and after compaction, denoted as LPI_{AC}, are calculated using the CPT-based liquefaction evaluation method summarized in Section *Liquefaction potential index (LPI)*. The calculated LPI_{BC} and LPI_{AC} values are listed in Table 5.2 and Table 5.3, respectively. It can be seen from Table 5.2 that, before compaction, all of the LPI_{BC} values are in the range between 10.1 and 24.0, corresponding to "high" to "very high" liquefaction severity class (refer to Table 5.1). This indicates that the study area, in general, has very high liquefaction potentials. After compaction, the LPI_{AC} values are significantly reduced to a range of 0.7 to 11.1.

To characterize the statistical and spatial distributions of the LPI_{BC} and LPI_{AC} values in the study area, the histogram and semivariogram of the LPI values are first constructed. Figure 5.5(a) and Figure 5.5(b) are the histograms of the LPI_{BC} and LPI_{AC}

values obtained at the CPT locations. The lognormal distribution is used to fit both histograms. The descriptive statistics including the minimum value, maximum value, mean, standard deviation, and coefficient of variation (COV) of 27 LPI_{BC} and 27 LPI_{AC} values for design earthquake are provided in Table 5.4.

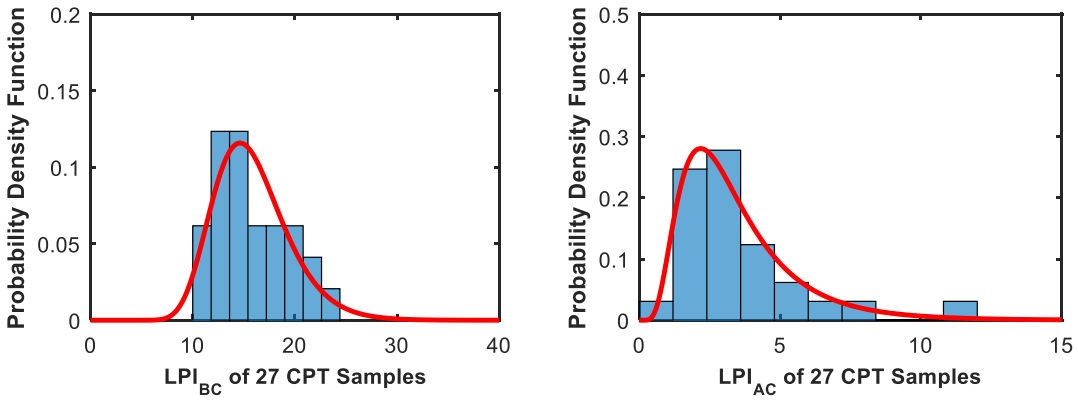

(a) (b)

Figure 5.5: The histogram of the LPI values of the 27 CPT samples under the seismic loading of the design earthquake: (a) before compaction; (b) after compaction.

Table 5.4: Descriptive statistics of the LPI_{BC} and LPI_{AC} values of 27 CPT soundings under two seismic shaking levels.

Statistics	Design Earthquake		Chi-Chi Earthquake	
	LPI_{BC}	LPI_{AC}	LPI_{BC}	LPI_{AC}
Minimum	10.1	0.7	0.3	0.00
Maximum	24.0	11.1	7.7	2.36
Mean	15.8	3.5	2.1	0.18
COV	0.24	0.62	0.98	2.67

As the LPI follows the lognormal distribution, the ln(LPI) is used to characterize semivariogram and generate random fields in the sequential Gaussian simulation. Accordingly, the semivariograms of the $\ln(LPI_{BC})$ and $\ln(LPI_{AC})$ values of the 27 CPT

samples are shown in Figure 5.6(a) and Figure 5.6(b), respectively. The blue squares are the empirical γ calculated from the $\ln(LPI_{BC})$ or $\ln(LPI_{AC})$ values at CPT locations. A weighted least square method by Cressie (1985) is used to fit the empirical γ. The red lines are the fitted γ using the exponential semivariogram model expressed in Eq. (5.15) and the fitting parameters are marked in the figures. It can be seen that the empirical γ of $\ln(LPI_{AC})$ is more scatter than the one $\ln(LPI_{BC})$, and the nugget effect is prominent for the fitted γ of $\ln(LPI_{AC})$.

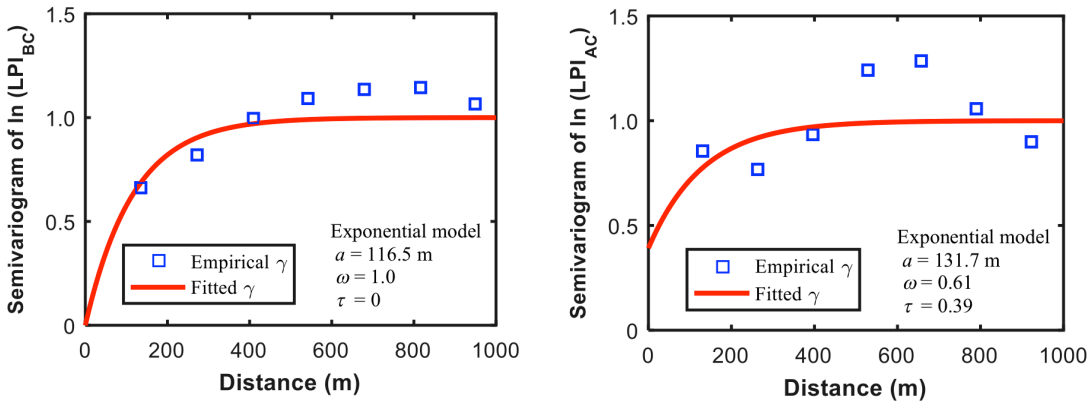

(a) (b)

Figure 5.6: The semivariogram of the LPI values of the 27 CPT samples under the shaking level of the design earthquake: (a) before compaction; (b) after compaction.

With the histogram and semivariogram as inputs, the random field model can be established and used for generating the liquefaction hazard map. In this case study, grid size of the random field is set as 10 m, which is the same as the subzone size in Figure 5.2. Through a parametric study, it is found that 1000 Monte Carlo Simulations (MCSs) is enough to get a stable random field, as the COV of the LPI values is barely varied with additional increase of MCS number. Each MCS generates one realization of the ln(LPI)

field. Then, the LPI field (transformed back to lognormal distribution) averaged from 1000 MCSs is used to present the liquefaction hazard of the entire site.

Figure 5.7(a) shows the LPI_{BC} map averaged from 1000 MCSs. It can be seen that the project site has very high potential to liquefy under the shaking level of the design earthquake. The associate uncertainty of the outcomes of random field modeling can also be visualized. Figure 5.7(b) shows the COV of LPI_{BC} at each location calculated from 1000 MCSs. It can be seen that the COV become larger at locations far away from the CPT sounding locations, especially at the margins of the study site. The COV map in this case offers a means to visualize the precision of the random field modeling.

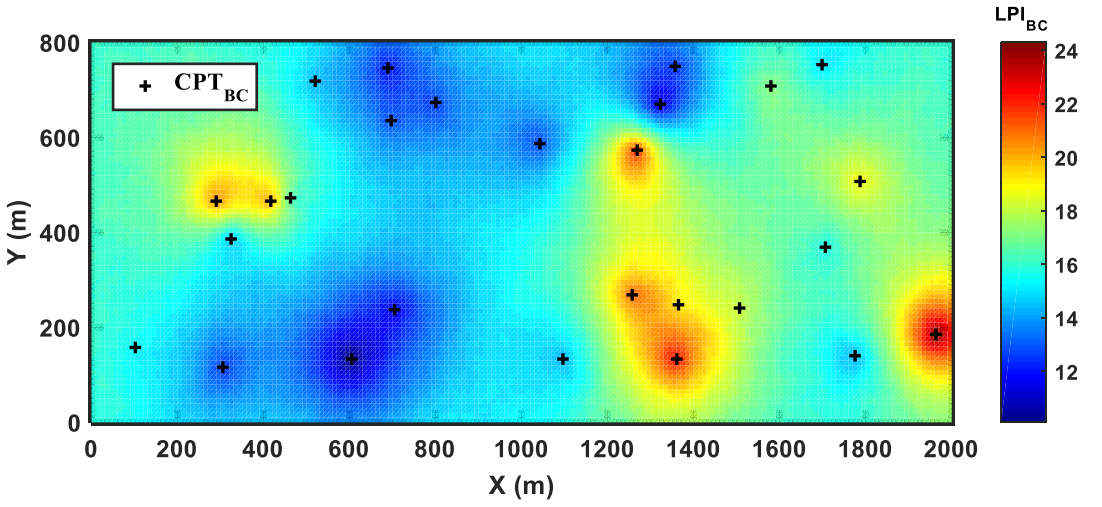

(a)

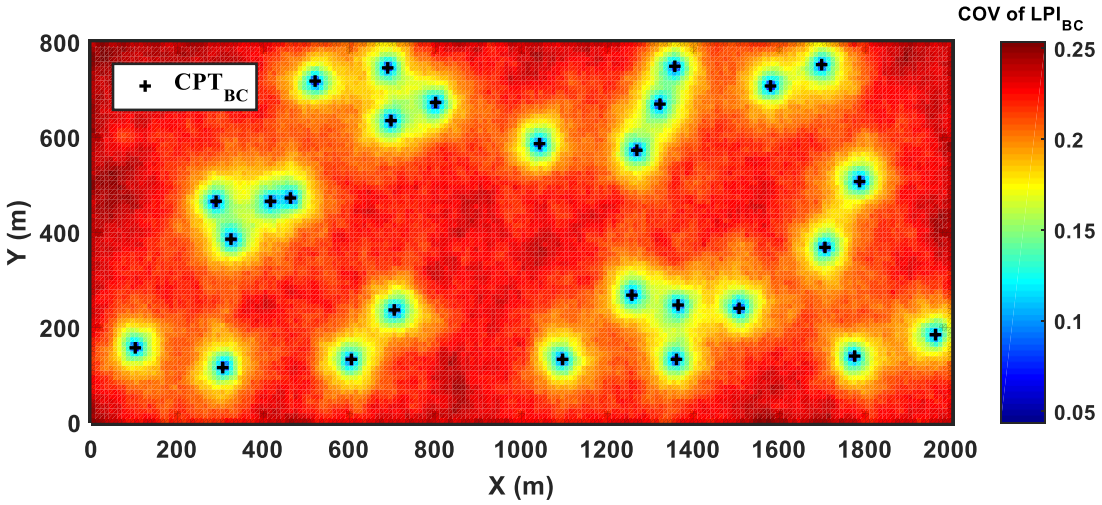

(b)

Figure 5.7: The pre-compaction LPI map (LPI_{BC}) under the shaking level of the design earthquake: (a) mean value of LPI_{BC}; (b) COV of LPI_{BC} calculated from 1000 MCSs.

The liquefaction hazard map can also be interpreted with the liquefaction severity class. Using the Figure 5.7(a) and the liquefaction severity classification in Table 5.1, the liquefaction map based on the severity class can be generated and shown in Figure 5.8(a). It can be clearly seen that the liquefaction severity of the study area was in Class 4 (high) to Class 5 (very high) before DC.

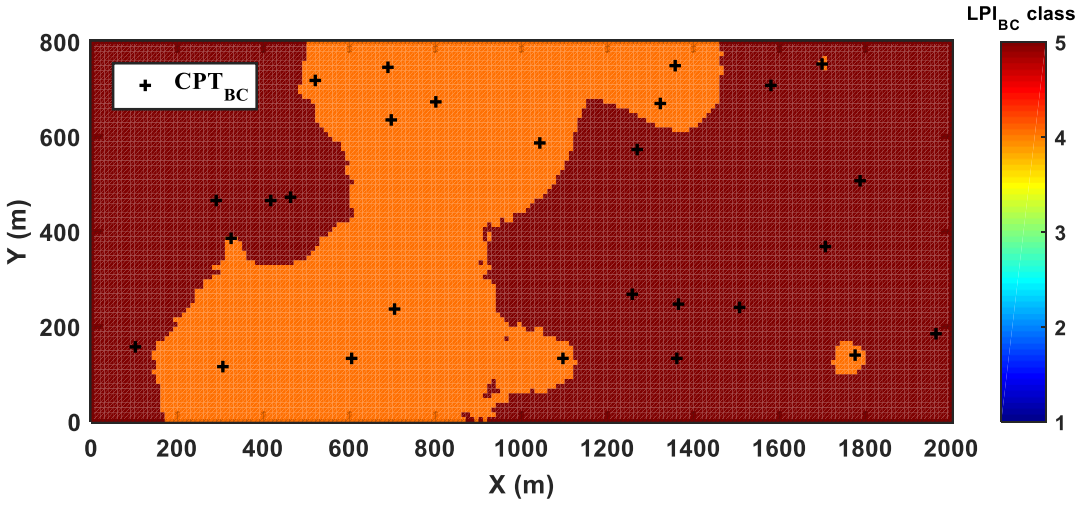

(a)

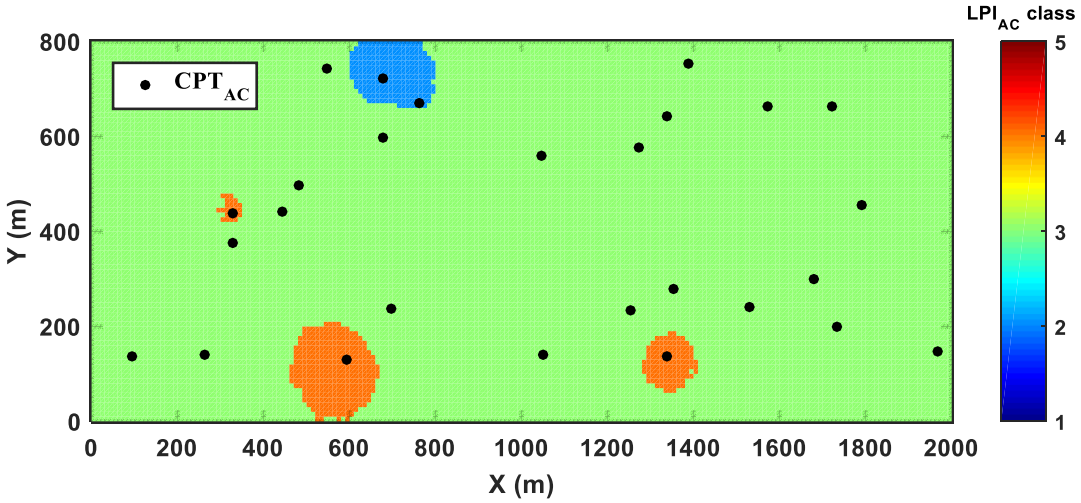

(b)

Figure 5.8: The LPI severity class map under the shaking level of the design earthquake: (a) before compaction; (b) after compaction.

With the liquefaction hazard map, including the LPI value map in Figure 5.7(a) and the LPI severity class map in Figure 5.8(a), the liquefaction risk can be easily visualized. The visualization maps are a useful tool in the design and construction processes of dynamic compaction, especially for communications between the engineers, contractors and the clients.

Effectiveness of Dynamic Compaction based on Areal Analysis

Following the same procedure presented above, the after-compaction liquefaction hazard map can be obtained through random field modeling and the results are shown in Figure 5.8(b). The liquefaction hazard maps derived for the scenarios of before DC and after DC, namely Figure 5.8(a) and Figure 5.8(b), can be compared and the effectiveness of the DC can be visualized.

Additional quantitative comparison, in terms of LPI_{AC} vs. LPI_{BC}, using all data from the entire site, is shown in Figure 5.9(a). For the study area, the effectiveness of DC in reducing LPI values is clearly demonstrated. It is noted that some LPI pairs are close to 1:1 line, which means less improvement is achieved with DC at these locations.

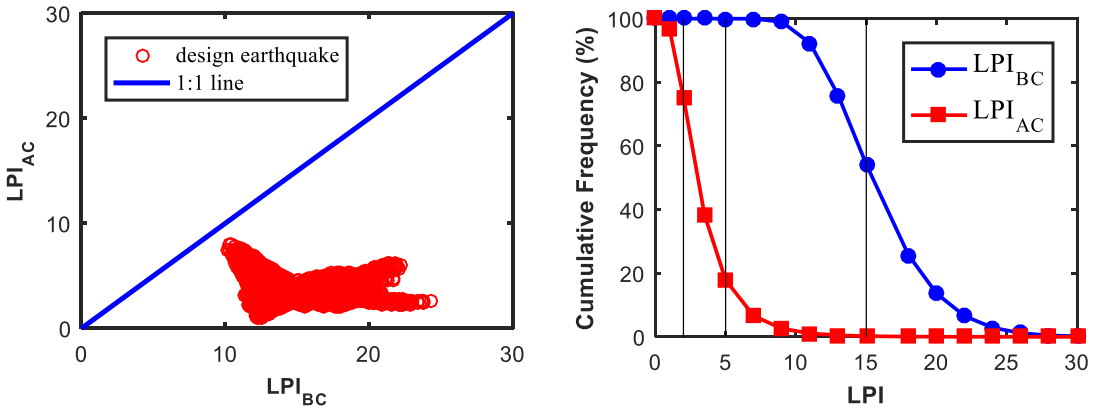

(a) (b)

Figure 5.9: The effect of dynamic compaction under the shaking level of the design earthquake: (a) LPI_{AC} vs. LPI_{BC}; (b) cumulative frequency plot of LPI_{BC} and LPI_{AC}.

Figure 5.9(b) shows the cumulative frequency distributions of simulative LPI_{AC} and LPI_{BC} values. The cumulative frequency of LPI is defined by the percentage of LPI values equal and greater than a threshold LPI value. For example, after DC, the LPI_{AC} values greater than 5 is 18%. In other words, there is only 18% chance that the LPI_{AC}

values will exceed 5 in this study area after DC. As a comparison, there is 100% chance that the LPI_{BC} values will exceed 5 in this study area before DC. Reducing the chance of exceeding LPI = 5, which is a threshold suggested by Toprak and Holzer (2003) for surface manifestations of liquefaction, from 100% before DC to 18% after DC is indeed very significant. Similarly, the chance of exceeding LPI = 15 drops from 54% before DC to zero after DC. As indicated in Table 5.1 (Sonmez, 2003), LPI > 15 indicates a "very high" liquefaction hazard. Such reduction in the likelihood from 54% to zero is drastic, which again demonstrates the effectiveness of DC at this project site. All these easy-to-see effects of DC in the mitigation of liquefaction hazard are enabled through random field modeling, and as such, the latter is demonstrated as a useful tool in geotechnical practice, not just an academic exercise.

Finally, an index called ground improvement ratio (R_I) is defined below for estimation of the effect of dynamic compaction on a relative basis:

$$R_I = \left(\frac{LPI_{BC} - LPI_{AC}}{LPI_{BC}}\right) \times 100\% \tag{5.16}$$

Figure 5.10 shows the improvement ratio (R_I) of the entire study area (project site) under the shaking level of the design earthquake. Other than a subzone in the lower left part of the project site, identified as location #24 in Figure 5.3, the entire study area is shown with an improvement ratio ranging approximately from 65% to 90%. To investigate this exception in the effect of DC, the location-specific liquefaction analysis before and after DC is carried out at location #24 and the results are shown in Figure 5.11. It can be seen that below the depth of 7 m, the $q_{t1N,cs}$ values after compaction are

smaller than those before compaction, which leads to a decrease in LPI (i.e., $LPI_{BC} < LPI_{AC}$) and a lower LPI severity class. This abnormal outcome might be caused by the errors in the CPT soundings, the variation in the DC operation, and the soil variability between the two CPT test locations. Further study is needed to confirm this observation at this local location. Nevertheless, the effectiveness of the random field-based visualization for assessing the effect of DC is further confirmed.

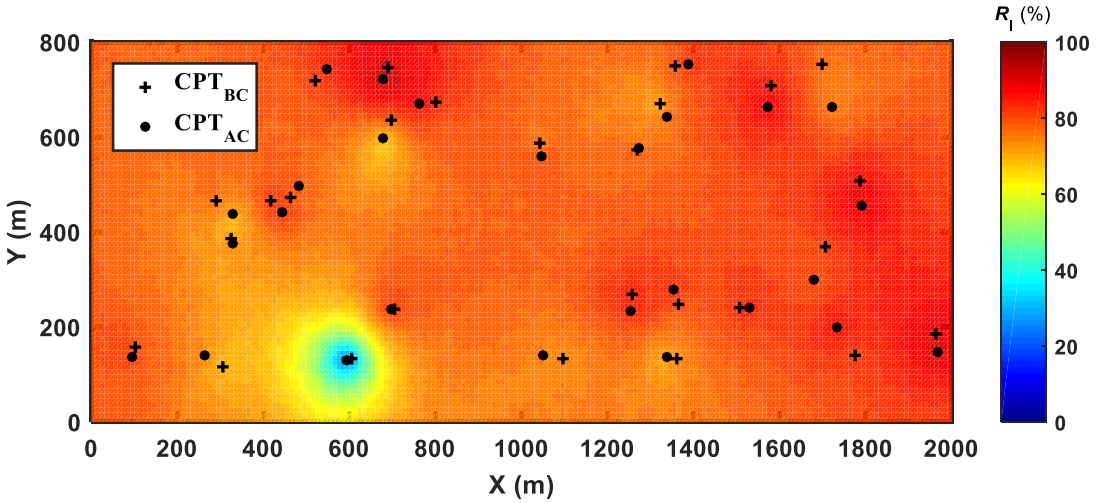

Figure 5.10: The improvement ratio (R_I) for the study site under the shaking level of the design earthquake.

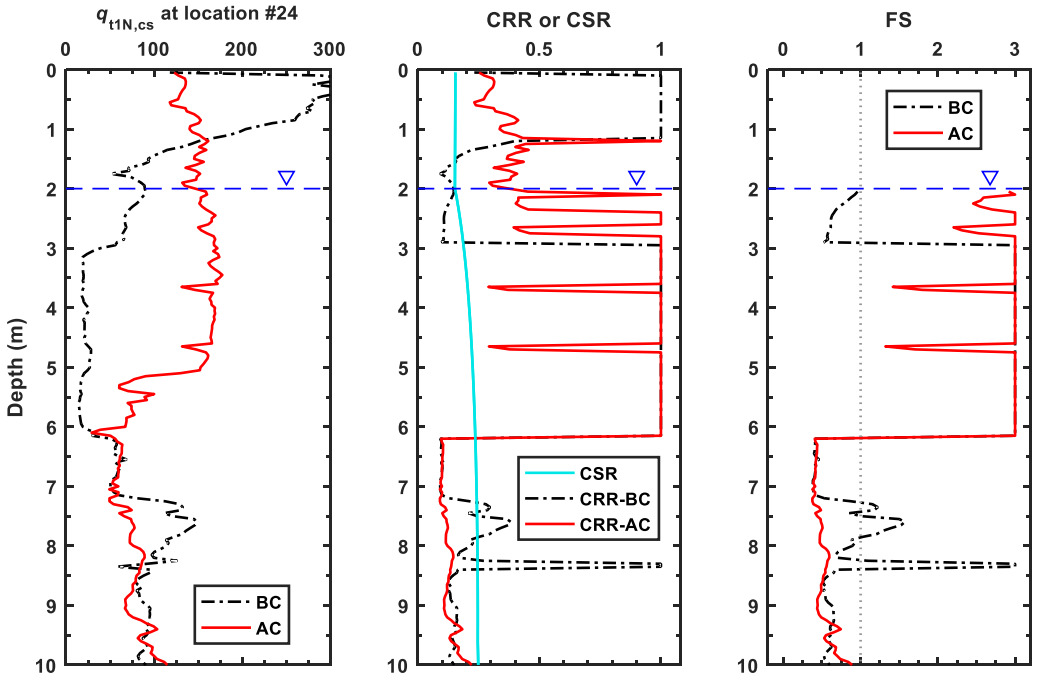

Figure 5.11: Location-specific analysis at location #24 under the shaking level of the design earthquake.

Performance of the site during the 1999 Chi-Chi earthquake

During the progression of the dynamic compaction (DC) project at the study site, a major earthquake, known as the 21 September 1999 Chi-Chi earthquake (M_w = 7.6), struck the central Taiwan. The earthquake caused a peak ground surface acceleration of a_{max} = 0.12 g at the study site, and soil liquefaction manifestation was observed in the zone where the DC had not been carried out. To check the accuracy of the random field modeling, the LPI hazard maps of the study site under the shaking level of the Chi-Chi earthquake (M_w = 7.6 and a_{max} = 0.12 g) are generated and compared with liquefaction observation.

Similar to the analysis made previously for the design earthquake, the histograms and semivariograms of the LPI_{BC} and LPI_{AC} values at CPT sounding locations using the Chi-Chi earthquake ground motion parameters are first characterized. The descriptive statistics of 27 LPI_{BC} and LPI_{AC} values are shown in Table 5.4. Following the same procedure as in the previous analysis, the LPI hazard maps (in terms of severity class) before and after DC under the shaking level of the 1999 Chi-Chi earthquake are obtained, as shown in Figures 5.12(a) and (b), respectively. It should be noted that at the time of the 1999 earthquake, the DC had been carried out only in part of the site, as illustrated in Figure 5.12 where the completed area is marked with dash lines.

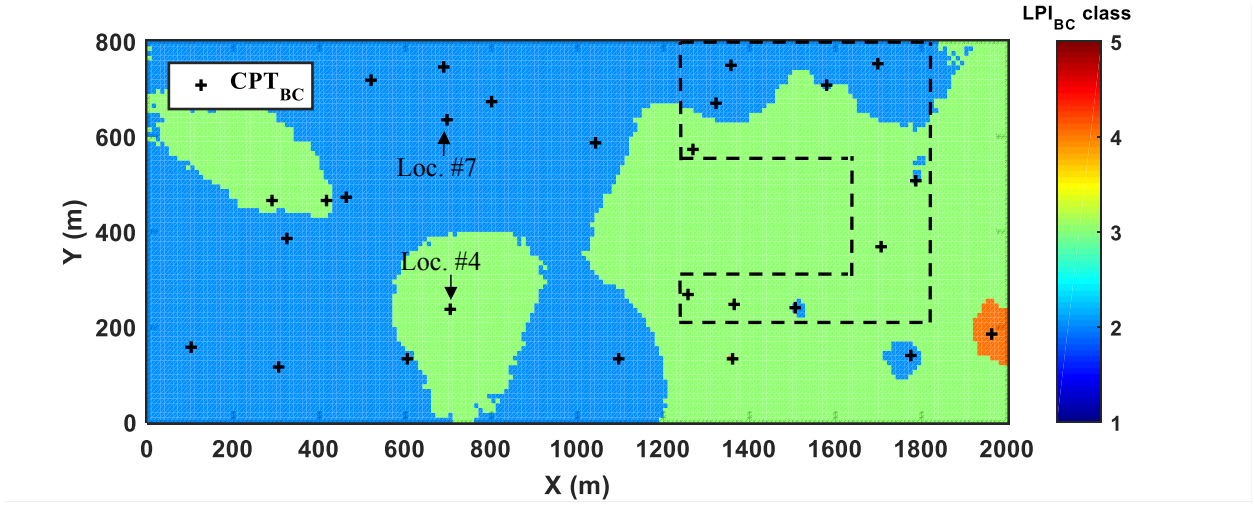

(a)

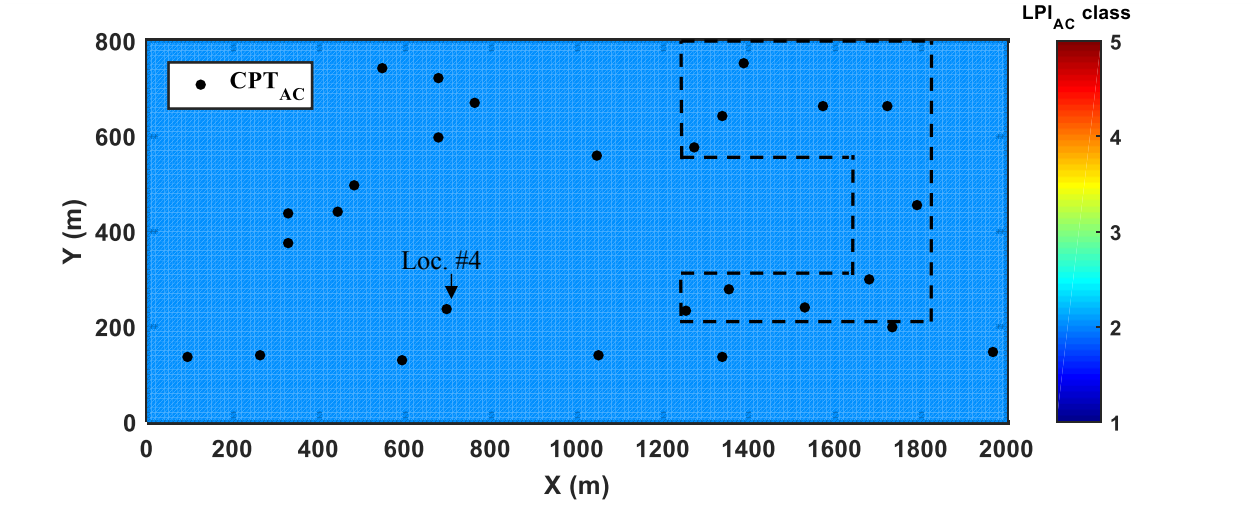

(b)

Figure 5.12: The LPI map averaged from 1000 MCS under the shaking level of the 21 September 1999 Chi-Chi earthquake (the area enclosed by dash line is the DC area completed prior to the Chi-Chi earthquake): (a) before compaction (LPI_{BC}); (b) after compaction (LPI_{AC}).

As reported in Lee et al. (2001), there was no observed liquefaction manifestation in the area that the DC work had been completed. This is consistent with the results of random filed modeling shown in Figure 5.12(b), as the area enclosed by dash lines is assessed with a liquefaction severity of Class 2 (minor). In the unimproved area at this site, however, the evidences of soil liquefaction were found during the 1999 Chi-Chi

earthquake. For example, in the vicinity of location #4, where DC had not been carried out, the sand boiling was observed with the ground settlement of 33–45 cm. The field observation is quite consistent with the generated LPI hazard map shown in Figure 5.12(a), as the liquefaction severity at location #4 was in Class 3 (moderate). For another example, in the vicinity of C-7 wet surface was observed after the 1999 event, which is consistent with the random field modeling of minor liquefaction prediction (see Figure 5.12a).

Compared to Figure 5.8(a) and Figure 5.8(b), the liquefaction potential of the project site (study area) is much smaller due to a smaller level of seismic loading. The effect of the shaking level and the effectiveness of DC may be more obviously observed with Figure 5.13, which is the box plots of simulated LPI_{BC} and LPI_{AC} values for both the design earthquake level and the Chi-Chi earthquake level of shaking. The dynamic compaction is shown as an effective technique to mitigate liquefaction hazards regardless of the shaking level, although in this case, the effect is more profound at higher ground shaking level.

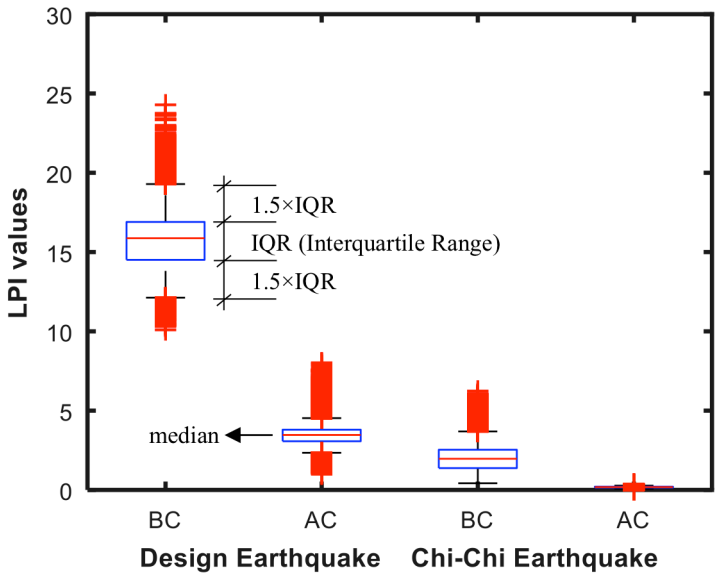

Figure 5.13: The box plot of simulated LPI_{BC} and LPI_{AC} values for both design earthquake and the Chi-Chi earthquake. (Note: data points beyond the whiskers are displayed by symbol +).

Limitations of the Study

The index LPI has been widely used in mapping the liquefaction hazard over an extended area or a region (Bong and Stuedlein, 2017; Bong and Stuedlein, 2018; Chen et al., 2016a; Holzer et al., 2006; Toprak and Holzer, 2003). It was adopted in this study for its convenience in assessing the effect of dynamic compaction (DC) on the liquefaction hazard under the seismic shaking. However, the LPI is a complex index, affected by many factors (Lee et al., 2004; Li et al., 2006). A careful calibration of LPI is always desirable. In this study, the calibration by Sonmez (2003) was adopted. Although no re-calibration of this LPI was carried out in this study, the use of this LPI is believed to be appropriate, since the focus was to assess the effect of DC (i.e., the relative performance

of the ground before and after DC) from the random field perspective. The use of improvement ratio (R_I) helps ease the concern of different interpretations of the LPI, as it provides an assessment of the ground improvement for the purpose of mitigating liquefaction hazard by DC on a relative basis.

Another limitation on the use of LPI in this study is the fact that most CPT soundings carried out after DC were limited to a shallower depth (up to the depth of approximately 10 m), as the design of DC in this project focused on the mitigation of the liquefaction potential of the critical layers, typically at the depths of 2 m to 6 m. The effect of DC at this project site was limited to the depth of approximately 8 m by design. Thus, post DC tests were limited to this depth accordingly. This is different from the definition of LPI that is extended to the depth of 20 m, although the weights given to the deeper layers (> 10 m) in the LPI are much lower than those at shallower depths.

Summary

In this chapter, the effect of dynamic compaction was assessed from a random field perspective. Specifically, a random field-based visualization procedure was developed as a means to assess the effect and benefits of dynamic compaction in the mitigation of liquefaction hazard. The CPT data before and after dynamic compaction in a ground improvement project were seldom available in an ideal one-to-one and side-by-side correspondence, which often complicated the evaluation of the effectiveness of dynamic compaction in the mitigation of liquefaction hazard. The random field-based visualization procedure developed in this study overcame this obstacle, and enabled an easy

observation of the effect and benefits of the dynamic compaction in the mitigation of liquefaction hazard.

CHAPTER VI

CONCLUSIONS AND RECOMMENDATIONS

Conclusions

The main objectives of this dissertation research as stated in Chapter I were: (1) to improve the existing probabilistic liquefaction evaluation methods, (2) to study the effectiveness of dynamic compaction in the mitigation of liquefaction hazards. These objectives have been accomplished through the work of three journal papers that cover a wide range of aspects: (I) in terms of the data employed, this dissertation work used V_s-based and CPT-based liquefaction databases, as well as synthetic data; (II) the work covered both location-specific evaluation and areal (or regional) evaluation of the probability of liquefaction; (III) the work addressed the problems from liquefaction potential evaluation to liquefaction hazard mitigation; (IV) the work utilized the random field theory to assess the effect of dynamic compaction in the mitigation of the liquefaction hazards. The conclusions of this dissertation work are summarized below:

***The following conclusions were drawn from the results of the study, "Predicting liquefaction probability based on shear wave velocity: an update" presented in Chapter III*:**

(1) Among the four GLMs developed, the log-log is found the optimal based on the Akaike information criterion (AIC), Bayesian information criterion (BIC), cross-validation (CV). The widely used logistic model, which has a simpler form, ranks

second based on these model assessment criteria. The log-log and logistic models are recommended for evaluating liquefaction probability based on V_s measurements.

(2) The sampling bias effect should be considered for developing probabilistic models. The weighted log-likelihood function is adopted to correct sample bias. The sensitivity study of the w_{NL}/w_L ratio shows that the Ku et al. (2012) approach for weighting factors is effective for correcting sampling bias effect.

(3) The generalized linear models are found to be sensitive to the database used for model development. The recommended probabilistic models are found quite satisfactory when they are checked against the new case histories derived from the 22 February 2011 Canterbury Earthquake. Further, with the combined database (with additional 36 serious liquefied cases), the updated log-log and logistic model are recommended for V_s-based liquefaction evaluation.

***The following conclusions were drawn from the results of the study, "Random field-based regional liquefaction hazard mapping - data inference and model verification using a synthetic digital soil field" presented in Chapter IV*:**

(1) All three random field models examined can capture closely the statistical distribution and spatial structure of the true $(q_{c1N})_{cs}$ and LPI fields, provided that the amount of field test data for model parameter inference is sufficient. The model performances deteriorate with the reduction of test samples as expected.

(2) All random field models are found to overestimate slightly liquefaction potentials over the studied area, compared to the benchmark liquefaction potential fields.

(3) When there is sufficient amount of field data for model parameter inference, the 3D local soil property approach (M3) slightly outperforms the averaged index approach (M1) and the 2D local soil property approach (M2) in terms of the accuracy in predicting the liquefaction potentials, while M1 is significantly more efficient than M2 and M3.

(4) When there are sufficient field test data to infer model parameters, it is recommended that the averaged index approach (M1) be used for liquefaction mapping considering a tradeoff between efficiency (in terms of computational effort) and accuracy. On the other hand, under the scenario of insufficient data, the 3D local soil property approach (M3) is recommended for its highest accuracy among the three models examined.

***The following conclusions are drawn from the results of the study, "Mitigation of liquefaction hazard by dynamic compaction - a random field perspective" presented in Chapter V*:**

(1) The random field-based visualization procedure developed in this study was shown effective in assessing the effect of dynamic compaction using CPT data at limited locations at a project site before and after the dynamic compaction. The effectiveness of this visualization procedure was demonstrated in a case study of a ground improvement project on a reclaimed ground in western Taiwan.

(2) The developed random field-based approach removed the need for side-by-side, one-to-one correspondence in the pre- and post-compaction CPT tests.

(3) The developed visualization procedure greatly facilitated the communications among the engineers and with their clients, as the effect and benefit of dynamic compaction in the mitigation of liquefaction hazard was easily visualized.

Recommendations for future studies

(1) In general, uncertainties in the seismic loading (shaking level), the liquefaction case histories, and the empirical liquefaction model, and errors in measurement (testing) and soil variability all demand use of the probabilistic approaches. Research to reduce the uncertainty through improved knowledge adds to the world-wide efforts in assessing and mitigating liquefaction hazards and should be pursued. To this end, recent development in robust geotechnical design may be followed to develop robust procedures for robust design of liquefaction mitigation effort (such as ground improvement).

(2) In Chapter III, the model calibration methodologies are applied to V_s-based liquefaction databases. There have been efforts by various parties in many parts of the world to collect and expand databases of liquefaction case histories. Applying these model calibration methodologies to new and expanded databases may be a worthwhile effort to improve the existing models. To this end, perhaps a more pressing issue is to determine how much more data is necessary to gain a robust assessment of liquefaction hazard. What are the data that are really needed and currently missing? Answering these questions may be more important than simply to collect more data and expand the database.

(3) In Chapter IV, the random field models were studied and assessed using a synthetic digital field with the assumptions of stationarity of the random field and evenly-spaced virtual field investigation plans. These assumptions may be appropriate for the intended purpose of evaluating and comparing different random field models in terms of accuracy and time-efficiency. In reality, the number of test data that are available may be limited, and the test pattern at a project site may not be evenly-spaced, the most suitable random field model in such scenario may not necessarily be the same as the one reached in this study. Thus, the conclusions should be viewed with caution and further study to quantify the effect of these assumptions is warranted.

(4) In Chapter V, the random-field-based visualization procedure has been demonstrated effective to aid in the evaluation of the effect of dynamic compaction using CPT soundings at limited locations at a project site before and after the dynamic compaction. The findings were obtained through modeling the liquefaction hazard of the project site as a random field of the liquefaction potential index (LPI). As a careful calibration of LPI is always desirable, and the depth of in situ test does not always reach to 20 m (the depth in the definition of LPI), additional work to adopt other liquefaction potential measure, e.g., the liquefaction probability (P_L), to model the liquefaction hazard of the site should be a worthwhile effort.

APPENDICES

Appendix A

Summary of the Andrus and Stokoe (2000) method

Factor of safety F_S is computed as:

$$F_S = \frac{\mathrm{CRR}_{7.5}}{\mathrm{CSR}_{7.5}} \tag{A.1}$$

Cyclic stress ratio $\mathrm{CSR}_{7.5}$ is computed as:

$$\mathrm{CSR}_{7.5} = \frac{\tau_{av}}{\sigma'_v} = 0.65\left(\frac{a_{\max}}{\mathrm{g}}\right)\left(\frac{\sigma_v}{\sigma'_v}\right)(\gamma_d)\left(\frac{1}{\mathrm{MSF}}\right) \tag{A.2}$$

where τ_{av} is the average equivalent uniform cyclic shear stress caused by the earthquake and assumed to be 0.65 of the maximum induced stress; $a_{\max}$ is the peak horizontal ground surface acceleration; g is the acceleration of gravity; σ_v is the total overburden stress in kPa; σ'_v is the initial effective overburden stress in kPa, and γ_d is a shear stress-reduction coefficient given as

$$\gamma_d = \begin{cases} 1.0 - 0.00765z & \text{for } \mathrm{z} \le 9.15\mathrm{m} \\ 1.174 - 0.0267z & \text{for } 9.15\mathrm{m} < \mathrm{z} \le 23\mathrm{m} \\ 0.744 - 0.008z & \text{for } 23\mathrm{m} < \mathrm{z} \le 30\mathrm{m} \end{cases} \tag{A.3}$$

where z is the depth below the ground surface.

MSF is the magnitude scaling factor, defined as:

$$\mathrm{MSF} = (M_w / 7.5)^{-2.56} \tag{A.4}$$

Cyclic resistance ratio $\mathrm{CRR}_{7.5}$ is computed as:

$$\mathrm{CRR}_{7.5} = 0.022\left(\frac{V_{s1,cs}}{100}\right)^2 + 2.8\left(\frac{1}{215 - V_{s1,cs}} - \frac{1}{215}\right) \tag{A.5}$$

where $V_{s1,cs}$ is the clean sand equivalence of stress-corrected shear wave velocity designated as modified shear wave velocity here.

$$V_{s1,cs} = K_{fc}V_{s1} = K_{fc}V_s C_{vs} = K_{fc}V_s\left(\frac{P_a}{\sigma'_v}\right)^{0.25} \tag{A.6}$$

where K_{fc} is a fines content correction to adjust values to a clean soil equivalent.

$$K_{fc} = \begin{cases} 1 & \text{for } FC \le 5\% \\ 1 + (FC - 5)f(V_{s1}) & \text{for } 5\% < FC < 35\% \\ 1 + 30f(V_{s1}) & \text{for } FC \ge 35\% \end{cases} \tag{A.7}$$

$$f(V_{s1}) = 0.009 - 0.0109(V_{s1}/100) + 0.0038(V_{s1}/100)^2 \tag{A.8}$$

The V_{s1} is the stress-corrected shear wave velocity; C_{vs} is a factor to correct measured V_s for overburden pressure; P_a is a reference stress of 100 kPa.

Appendix B

CPT-based liquefaction model

The CPT-based liquefaction model proposed in Robertson and Wride (1998) and subsequently updated by Robertson (2009) is adopted in this study. The factor of safety against liquefaction (F_S) is defined as the ratio of cyclic resistance (CRR) and cyclic stress (CSR).

$$F_S = \frac{\text{CRR}}{\text{CSR}} \tag{B.1}$$

The CRR provides soil resistances and it is defined in Eq. (B.2), which is a function of the equivalent clean sand normalized CPT penetration tip resistance $(q_{c1N})_{\text{cs}}$.

$$\text{CRR} = \begin{cases} 0.8333[(q_{c1N})_{\text{cs}}/1000] + 0.05 & \text{if} \quad (q_{c1N})_{\text{cs}} < 50 \\ 93[(q_{c1N})_{\text{cs}}/1000]^3 + 0.08 & \text{if} \quad 50 < (q_{c1N})_{\text{cs}} < 160 \end{cases} \tag{B.2}$$

The CSR represents the earthquake loadings, and the following adjusted form is adopted (Youd et al. 2001)

$$\text{CSR} = 0.65\left(\frac{a_{\max}}{\text{g}}\right)\left(\frac{\sigma_{\text{vo}}}{\sigma'_{\text{vo}}}\right)(r_d)\left(\frac{1}{\text{MSF}}\right)\left(\frac{1}{K_\sigma}\right) \tag{B.3}$$

where $a_{\max}$ is the maximum horizontal acceleration at the ground surface; g is the gravitational acceleration and equal to 9.81 m/s^2, σ_{vo} and σ'_{vo} are the respective total and effective vertical overburden stresses.

The stress reduction factor r_{d} is a function of depth z and defined below (Youd et al. 2001)

$$r_{\mathrm{d}} = \frac{1.000 - 0.4113z^{0.5} + 0.04052z + 0.001753z^{1.5}}{1.000 - 0.4177z^{0.5} + 0.05729z - 0.006205z^{1.5} + 0.001210z^{2}} \tag{B.4}$$

The MSF is the magnitude scaling factor and related to the moment magnitude M_{w} as (Youd et al. 2001)

$$\mathrm{MSF} = \frac{10^{2.24}}{M_{\mathrm{w}}^{2.56}} \tag{B.5}$$

The K_{σ} in Eq.(B.6) is the overburden correction factor for CSR (Youd et al. 2001). The correction is applied when the σ'_{vo} greater than 100 kPa.

$$K_{\sigma} = \left(\frac{\sigma'_{vo}}{P_a}\right)^{(f-1)} \tag{B.6}$$

where P_a is the atmospheric pressure; f is an exponent and recommended as: f = 0.7–0.8 for relative densities between 40 and 60%; f = 0.6–0.7 for relative densities between 60 and 80%.

Appendix C

Liquefaction potential index

The liquefaction potential index (LPI) was developed by Iwasaki et al. (1978&1982). It is based on the assumption that the liquefaction potential is related to the thickness of the liquefied layer and the factor of safety against liquefaction, and its equation is expressed as follows:

$$\mathrm{LPI} = \int_0^{20} \omega(z) F_L \mathrm{d}z \tag{C.1}$$

where z is the soil depth in meters and it is commonly evaluated top 20 m of soil profile; $\omega(z)$ is the function of soil depth and F_L is a function of factor of safety (F_S) against liquefaction listed as follow:

$$\omega(z) = 10 - 0.5z \tag{C.2}$$

$$F_L = \begin{cases} 0 & F_S \geq 1.2 \\ 1 - F_S & F_S \leq 0.95 \\ 2\times 10^6 e^{-18.427 F_S} & 0.95 < F_S < 1.2 \end{cases} \tag{C.3}$$

REFERENCES

Akaike, H. (1973). Information theory and an extension of the maximum likelihood principle. In B.N. Petrox and F. Caski, Second International Symposium on Information Theory (pp. 267-281). Akademia Kiado, Budapest.

Andrus, R. D., Stokoe, K. H., & Chung, R. M. (1999). Draft guidelines for evaluating liquefaction resistance using shear wave velocity measurements and simplified procedures (p. 140). US Department of Commerce, Technology Administration, National Institute of Standards and Technology.

Andrus, R. D. and Stokoe II, K. H. (2000). Liquefaction resistance of soils from shear-wave velocity. Journal of Geotechnical and Geoenvironmental Engineering, 126(11):1015–1025.

Andrus, R. D., Stokoe, K. H., & Juang, C.H. (2004). Guide for shear-wave-based liquefaction potential evaluation. Earthquake Spectra, 20(2), 285-308.

Armstrong, J. S. and Collopy, F. (1992). Error measures for generalizing about forecasting methods: Empirical comparisons. International Journal of Forecasting, 8(1):69–80.

Asgari, A., Oliaei, M., & Bagheri, M. (2013). Numerical simulation of improvement of a liquefiable soil layer using stone column and pile-pinning techniques. Soil Dynamics and Earthquake Engineering, 51, 77-96.

Baise, L. G., Higgins, R. B., and Brankman, C. M. (2006). Liquefaction hazard mapping – statistical and spatial characterization of susceptible units. Journal of Geotechnical and Geoenvironmental Engineering, 132(6):705–715.

Baise, L. G., Lenz, J. A., and Thompson, E. M. (2008). Discussion of "mapping liquefaction potential considering spatial correlations of CPT measurements" by Chia-Nan Liu and Chien-Hsun Chen. Journal of Geotechnical and Geoenvironmental Engineering, 134(2), 262-263.

Baker, J. W. and Faber, M. H. (2008). Liquefaction risk assessment using geostatistics to account for soil spatial variability. Journal of Geotechnical and Geoenvironmental Engineering, 134 (1):14–23.

Baker, J. W., Seifried, A., Andrade, J. E., and Chen, Q. (2011). Characterization of random fields at multiple scales: an efficient conditional simulation procedure and

applications in geomechanics. Applications of Statistics and Probability in Civil Engineering, page 347.

Bong, T., & Stuedlein, A. W. (2017). Spatial variability of CPT parameters and silty fines in liquefiable beach sands. Journal of Geotechnical and Geoenvironmental Engineering, 143(12), 04017093.

Bong, T., & Stuedlein, A. W. (2018). Effect of Cone Penetration Conditioning on Random Field Model Parameters and Impact of Spatial Variability on Liquefaction-Induced Differential Settlements. Journal of Geotechnical and Geoenvironmental Engineering, 144(5), 04018018.

Boulanger, R. W. and Idriss, I. M. (2012). Probabilistic standard penetration test-based liquefaction triggering procedure. Journal of Geotechnical and Geoenvironmental Engineering, 138(10): 1185–1195.

Boulanger, R. W., & Idriss, I. M. (2015). CPT-based liquefaction triggering procedure. Journal of Geotechnical and Geoenvironmental Engineering, 142(2), 04015065.

Bradley, B. A., & Hughes, M. (2012). Conditional peak ground accelerations in the Canterbury earthquakes for conventional liquefaction assessment. In Technical Report for the Ministry of Business, Innovation and Employment, New Zealand.

Brankman, C. M., & Baise, L. G. (2008). Liquefaction susceptibility mapping in Boston, Massachusetts. Environmental & Engineering Geoscience, 14(1), 1-16.

Building Seismic Safety Council (BSSC). 1997. NEHRP Recommended Provisions for Seismic Regulations for New Buildings and Other Structures, Part 2: Commentary, Foundation Design Requirements. Washington, DC: Building Seismic Safety Council.

Carrasco, P. C. (2010). Nugget effect, artificial or natural? Journal of the Southern African Institute of Mining and Metallurgy, 110(6), 299-305.

Cetin, K. O., Der Kiureghian, A., & Seed, R. B. (2002). Probabilistic models for the initiation of seismic soil liquefaction. Structural safety, 24(1), 67-82.

Cetin, K. O., Seed, R. B., Der Kiureghian, A., Tokimatsu, K., Harder Jr, L. F., Kayen, R. E., and Moss, R. E. (2004). Standard penetration test-based probabilistic and deterministic assessment of seismic soil liquefaction potential. Journal of Geotechnical and Geoenvironmental Engineering, 130(12), 1314–1340.

Chen, C. J., & Juang, C. H. (2000). Calibration of SPT-and CPT-based liquefaction evaluation methods. Geotechnical Special Publication, 49-64.

Chen, Q., Seifried, A., Andrade, J. E., and Baker, J. W. (2012). Characterization of random fields and their impact on the mechanics of geosystems at multiple scales. International Journal for Numerical and Analytical Methods in Geomechanics, 36(2):140–165.

Chen, Q., Wang, C., and Juang, C. H (2015). CPT-based evaluation of liquefaction potential accounting for soil spatial variability at multiple scales. Journal of Geotechnical and Geoenvironmental Engineering, 04015077-1.

Chen, Q., Wang, C., and Juang, C. H. (2016). Probabilistic and spatial assessment of liquefaction- induced settlements through multiscale random field models. Engineering Geology, 211: 135–149.

Christian, J. T., & Swiger, W. F. (1975). Statistics of liquefaction and SPT results. Journal of the Geotechnical Engineering Division, 101(11), 1135-1150.

Cressie, N. (1985). Fitting variogram models by weighted least squares. Journal of the International Association for Mathematical Geology, 17(5), 563-586.

Cubrinovski, M., Bradley, B., Wotherspoon, L., Green, R., Bray, J., Wood, C., ... & Wells, D. (2011). Geotechnical aspects of the 22 February 2011 Christchurch earthquake. Bulletin of the New Zealand Society for Earthquake Engineering, 44(4), 205-226

Cubrinovski, M., Taylor, M., Henderson, D., Winkley, A., Haskell, J., Bradley, B. A., Hughes, M., Wotherspoon, L., Bray, J., & O'Rourke, T. (2014). Key factors in the liquefaction-induced damage to buildings and infrastructure in Christchurch: Preliminary findings. In Proceedings, 2014 New Zealand Society for Earthquake Engineering Conference, New Zealand Society for Earthquake Engineering Inc., Wellington, New Zealand, Paper No. O78.

David, M. (1977). Geostatistical ore reserve estimation. Elsevier Sci. Publ. Co., New York, Developments in Geomathematics, vol. 2, p. 384.

Dawson, K. and Baise, L. G. (2004). Three dimensional liquefaction hazard analysis. In Proceedings of the 13th World Conference on Earthquake Engineering. Vancouver, BC, Canada.

Dise, K., Stevens, M. G., & Von Thun, J. L. (1994). Dynamic compaction to remediate liquefiable embankment foundation soils. In Proceedings, In-Situ Deep Soil Improvement, GSP 45, ASCE, 1-25.

Elkateb, T., Chalaturnyk, R., & Robertson, P. K. (2003). Simplified geostatistical analysis of earthquake-induced ground response at the Wildlife Site, California, USA. Canadian geotechnical journal, 40(1), 16-35.

Fenton, G. A., & Vanmarcke, E. H. (1998). Spatial variation in liquefaction risk. Geotechnique, 48(6), 819-831.

Fenton, G. A. (1999). Random field modeling of CPT data. Journal of Geotechnical and Geoenvironmental Engineering, 125(6):486–498.

Finn, W. D. L. (2002). State of the art for the evaluation of seismic liquefaction potential. Computers and Geotechnics, 29(5):329–341.

Fox, J. (2015). Applied regression analysis and generalized linear models. Sage Publications.

Gelman, A., Carlin, J. B., Stern, H. S., & Rubin, D. B. (1995). Bayesian data analysis (Vol. 2). Chapman & Hall/CRC.

Gessler, P. E., Moore, I. D., McKenzie, N. J., & Ryan, P. J. (1995). Soil-landscape modelling and spatial prediction of soil attributes. International Journal of Geographical Information Systems, 9(4), 421-432.

Ghassemi, A., Pak, A., & Shahir, H. (2010). Numerical study of the coupled hydro-mechanical effects in dynamic compaction of saturated granular soils. Computers and Geotechnics, 37(1-2), 10-24.

Goovaerts, P. (1997). Geostatistics for Natural Resources Evaluation. Oxford University Press, New York.

Gotway, C. A., & Stroup, W. W. (1997). A generalized linear model approach to spatial data analysis and prediction. Journal of Agricultural, Biological, and Environmental Statistics, 157-178.

Green, R. A., Cubrinovski, M., Cox, B., Wood, C., Wotherspoon, L., Bradley, B., & Maurer, B. (2014). Select liquefaction case histories from the 2010-2011 Canterbury earthquake sequence. Earthquake Spectra, 30(1), 131-153.

Hamada, M., Isoyama, R., & Wakamatsu, K. (1996). Liquefaction-induced ground displacement and its related damage to lifeline facilities. Soils and foundations, 36(Special), 81-97.

Han, J. (2015). Principles and practice of ground improvement. John Wiley & Sons.

Hausler, E. A., & Sitar, N. (2001). Performance of soil improvement techniques in earthquakes. In Proceedings, International Conferences on Recent Advances in Geotechnical Earthquake Engineering and Soil Dynamics, Paper No. 10.15

Hausler, E. A., & Koelling, M. (2004). Performance of improved ground during the 2001 Nisqually earthquake. In Proceedings, Fifth International Conference on Case Histories in Geotechnical Engineering, New York, Paper No. 3.27.

Hayati, H., & Andrus, R. D. (2008). Liquefaction potential map of Charleston, South Carolina based on the 1886 earthquake. Journal of Geotechnical and Geoenvironmental Engineering, 134(6), 815-828.

Heidari, T., & Andrus, R. D. (2010). Mapping liquefaction potential of aged soil deposits in Mount Pleasant, South Carolina. Engineering Geology, 112(1-4), 1-12.

Heidari, T., & Andrus, R. D. (2012). Liquefaction potential assessment of Pleistocene beach sands near Charleston, South Carolina. Journal of Geotechnical and Geoenvironmental Engineering, 138(10), 1196-1208.

Ho, C.S. (1988). An Introduction to the Geology of Taiwan: Explanatory Text of the Geology Map of Taiwan, 2nd edition.

Hoffmann, J. P. (2004). Generalized linear models: An applied approach. Pearson College Division.

Holzer, T. L., Bennett, M. J., Noce, T. E., Padovani, A. C., and Tinsley III, J. C. (2006a). Liquefaction hazard mapping with LPI in the greater oakland, california, area. Earthquake Spectra, 22 (3):693–708.

Holzer, T. L., Luke Blair, J., Noce, T. E., and Bennett, M. J. (2006b). Predicted liquefaction of east bay fills during a repeat of the 1906 san francisco earthquake. Earthquake Spectra, 22(S2): 261–277.

Ishihara, K. (1999). Terzaghi oration: Geotechnical aspects of the 1995 Kobe earthquake. In Proceedings of (Vol. 14, pp. 2047-2073).

Iwasaki, T., Tatsuoka, F., Tokida, K., and Yasuda, S. (1978). A practical method for assessing soil liquefaction potential based on case studies at various sites in Japan. In Proceedings 2nd International Conference on Microzonation, 885–896.

Iwasaki, T., Tokida, K., Tatsuoka, F., Watanabe, S., Yasuda, S., and Sato, H (1982). Microzonation for soil liquefaction potential using simplified methods. In Proceedings of the 3rd International Conference on Microzonation, Seattle, vol 3, pp 1319–1330.

Jang, C. S., & Liu, C. W. (2004). Geostatistical analysis and conditional simulation for estimating the spatial variability of hydraulic conductivity in the Choushui River alluvial fan, Taiwan. Hydrological Processes, 18(7), 1333-1350.

Journel, A. G., & Huijbregts, C. J. (1978). Mining geostatistics. Academic press.

Juang, C. H., Rosowsky, D. V., & Tang, W. H. (1999). Reliability-based method for assessing liquefaction potential of soils. Journal of Geotechnical and Geoenvironmental Engineering, 125(8), 684-689.

Juang, C. H., Chen, C. J., Rosowsky, D. V., & Tang, W. H. (2000). CPT-based liquefaction analysis, Part 2: Reliability for design. Geotechnique, 50(5), 593-599.

Juang, C. H., Chen, C. J., & Jiang, T. (2001). Probabilistic framework for liquefaction potential by shear wave velocity. Journal of geotechnical and geoenvironmental engineering, 127(8), 670-678.

Juang, C. H., Jiang, T., & Andrus, R. D. (2002). Assessing probability-based methods for liquefaction potential evaluation. Journal of Geotechnical and Geoenvironmental Engineering, 128(7), 580-589.

Juang, C. H., Yuan, H., Lee, D. H., and Lin, P. S. (2003). Simplified cone penetration test-based method for evaluating liquefaction resistance of soils. Journal of Geotechnical and Geoenvironmental engineering, 129(1), 66–80.

Juang, C. H., Fang, S. Y., & Khor, E. H. (2006). First-order reliability method for probabilistic liquefaction triggering analysis using CPT. Journal of Geotechnical and Geoenvironmental Engineering, 132(3), 337-350.

Juang, C. H., Liu, C. N., Chen, C. H., Hwang, J. H., and Lu, C. C. (2008). Calibration of liquefaction potential index: A re-visit focusing on a new CPTU model. Engineering Geology, 102(1), 19–30.

Juang, C. H., Fang, S. Y., Tang, W. H., Khor, E. H., Kung, G. T. C., & Zhang, J. (2009). Evaluating model uncertainty of an SPT-based simplified method for reliability analysis for probability of liquefaction. Soils and Foundations, 49(1), 135-152.

Juang, C. H., Ching, J., Luo, Z., & Ku, C. S. (2012). New models for probability of liquefaction using standard penetration tests based on an updated database of case histories. Engineering Geology, 133, 85-93.

Juang, C. H., Luo, Z., Atamturktur, S., and Huang, H. (2012). Bayesian updating of soil parameters for braced excavations using field observations. Journal of Geotechnical and Geoenvironmental Engineering, 139(3):395–406.

Juang, C. H., Ching, J., & Luo, Z. (2013). Assessing SPT-based probabilistic models for liquefaction potential evaluation: a 10-year update. Georisk: Assessment and management of risk for engineered systems and geohazards, 7(3), 137-150.

Juang, C. H., Zhang, J., Khoshnevisan, S., & Gong, W. (2017a). Probabilistic methods for assessing soil liquefaction potential and effect. In proceedings, Geo-Risk 2017, GSP282, ASCE, 122-144.

Juang, C. H., Shen, M., Wang C., & Chen, Q. (2017b). Random field-based regional liquefaction hazard mapping - data inference and model verification using a synthetic digital soil field. Bulletin of Engineering Geology and the Environment, doi:10.1007/s10064-017-1071-y.

Juang, C.H., Chen, Q., Shen, M., & Wang, C. (2018). Probabilistic assessment and mapping of liquefaction hazard: from site-specific analysis to regional mapping. Keynote Lecture, GeoShanghai 2018.

Khoshnevisan, S., Juang, C. H., Zhou, Y. G., & Gong, W. (2015). Probabilistic assessment of liquefaction-induced lateral spreads using CPT—Focusing on the 2010–2011 Canterbury earthquake sequence. Engineering Geology, 192, 113-128.

Knudsen, K. L., Witter, J. M., Wentworth, R. C., Helley, C. M., Nicholson, E. J., Wright, R. S., & HM Brown, K. M. (2000). Preliminary maps of Quaternary deposits and liquefaction susceptibility, nine-county San Francisco Bay Region, California: A digital database.

Ku, C. S., Juang, C. H., Chang, C. W., & Ching, J. (2012). Probabilistic version of the Robertson and Wride method for liquefaction evaluation: development and application. Canadian Geotechnical Journal, 49(1), 27-44.

Robertson and Wride method for liquefaction evaluation: development and application. Canadian Geotechnical Journal, 49(1), 27-44

Kung, G. T., Juang, C. H., Hsiao, E. C., and Hashash, Y. M. (2007). Simplified model for wall deflection and ground-surface settlement caused by braced excavation in clays. Journal of Geotechnical and Geoenvironmental Engineering, 136(6):731–747.

Lai, S. Y., Chang, W. J., & Lin, P. S. (2006). Logistic regression model for evaluating soil liquefaction probability using CPT data. Journal of geotechnical and geoenvironmental engineering, 132(6), 694-704.

Lane, P. W. (2002). Generalized linear models in soil science. European Journal of Soil Science, 53(2), 241-251.

Lee, D. H., Juang, C. H., & Ku, C. S. (2001). Liquefaction performance of soils at the site of a partially completed ground improvement project during the 1999 Chi-Chi earthquake in Taiwan. Canadian geotechnical journal, 38(6), 1241-1253.

Lenz, J. A. and Baise, L. G (2007). Spatial variability of liquefaction potential in regional mapping using CPT and SPT data. Soil Dynamics and Earthquake Engineering, 27(7):690–702.

Li, D. K., Juang, C. H., and Andrus, R. D. (2006). Liquefaction potential index: a critical assessment using probability concept. Taiwan Geotechnical Society Journal of Geoengineering, 1(1), 11–24.

Liao, S. S., Veneziano, D., & Whitman, R. V. (1988). Regression models for evaluating liquefaction probability. Journal of Geotechnical Engineering, 114(4), 389-411.

Liu, C. N. and Chen, C. H. (2006). Mapping liquefaction potential considering spatial correlations of CPT measurements. Journal of Geotechnical and Geoenvironmental Engineering, 132 (9):1178–1187.

Liu, F., Li, Z., Jiang, M., Frattini, P., & Crosta, G. (2016). Quantitative liquefaction-induced lateral spread hazard mapping. Engineering Geology, 207, 36-47.

Liu, W., Chen, Q., Wang, C., Juang, C.H. and Chen, G. (2017). Spatially correlated multiscale Vs30 mapping and a case study of the Suzhou site, Engineering Geology, 220, 110-122.

Lukas, R. G. (1995). Geotechnical Engineering Circular No. 1, Dynamic compaction. Federal Highway Report FHWA-SA-95-037, U.S.A.

Martin, J. R., Olgun, C. G., & Mitchell, J. K. (2002). Preliminary findings from an investigation of improved ground performance during the 1999 Turkey Earthquakes. In NSF-TUBITAK Turkey-Taiwan Earthquakes Grantee Workshop, 24-26.

Mayne, P. W., Jones Jr, J. S., & Dumas, J. C. (1984). Ground response to dynamic compaction. Journal of Geotechnical Engineering, 110(6), 757-774.

McKenzie, N. J., & Ryan, P. J. (1999). Spatial prediction of soil properties using environmental correlation. Geoderma, 89(1), 67-94.

Ministry of Communication. 1996. Seismic design specifications for highway bridges. Ministry of Communication, Taipei, Taiwan. (In Chinese)

Mitchell, J. K., & Wentz, F. J. (1991). Performance of improved ground during the Loma Prieta Earthquake. Berkeley: Earthquake Engineering Research Center, University of California, Vol. 91, No. 12.

Moss, R. E., Seed, R. B., Kayen, R. E., Stewart, J. P., Der Kiureghian, A., and Cetin, K. O. (2006). CPT-based probabilistic and deterministic assessment of in situ seismic soil liquefaction potential. Journal of Geotechnical and Geoenvironmental Engineering, 132(8), 1032–1051.

Myung, J. I., & Pitt, M. A. (2004). Model comparison methods. Methods in Enzymology, 383, 351-366.

Ogasawara, T., Matsubayashi, Y., Sakai, S., & Yasuda, T. (2012). Characteristics of the 2011 Tohoku earthquake and tsunami and its impact on the northern Iwate coast. Coastal Engineering Journal, 54(1), 1250003-1.

Olgun, C. G. (2003). Performance of Improved Ground and Reinforced Soil Structures during Earthquakes a Case Studies and Numerical Analyses (Doctoral dissertation, Virginia Tech).

Onyejekwe, S., Kang, X., Ge, L., 2016. Evaluation of the scale of fluctuation of geotechnical parameters by autocorrelation function and semivariogram function. Engineering Geology, 214: 43-49.

Orense, R. P., Kiyota, T., Yamada, S., Cubrinovski, M., Hosono, Y., Okamura, M., & Yasuda, S. (2011). Comparison of liquefaction features observed during the 2010 and 2011 Canterbury earthquakes. Seismological Research Letters, 82(6), 905-918.

Popescu, R., Prévost, J. H., & Deodatis, G. (1997). Effects of spatial variability on soil liquefaction: some design recommendations. Geotechnique, 47(5), 1019-1036.

Prasomphan, S. and Mase, S. (2013). Generating prediction map for geostatistical data based on an adaptive neural network using only nearest neighbors. International Journal of Machine Learning and Computing, 3(1):98–102.

Robertson, P. K. and Wride, C. E. (1998). Evaluating cyclic liquefaction potential using the cone penetration test. Canadian Geotechnical Journal, 35(3):442–459.

Robertson, P. K. (2009). Performance based earthquake design using the CPT. Proc. IS-Tokyo, 3-20.

Robertson, P. K. (2010). Soil behaviour type from the CPT: an update. In 2nd international symposium on cone penetration testing, USA, 9-11.

Schwarz, G. (1978). Estimating the dimension of a model. The annals of statistics, 6(2), 461-464.

Seed, H. B. and Idriss, I. M. (1971). Simplified procedure for evaluating soil liquefaction potential. Journal of the Soil Mechanics and Foundations Division, 97(9):1249–1273.

Seed, H.B. (1981). Earthquake-resistant design of earth dams. In Seismic Design of Embankments and Caverns, proceedings of the ASCE National Convention, Philadelphia, PA, May 16-20, 1983, Terry R. Howard, Editor, ASCE, New York. 41-64.

Seed, H. B. and Idriss, I. M. (1982). Ground motions and soil liquefaction during earthquakes. Earthquake Engineering Research Institute. Vol. 5.

Seed, H. B., Idriss, I. M., & Arango, I. (1983). Evaluation of liquefaction potential using field performance data. Journal of Geotechnical Engineering, 109(3), 458-482.

Seed, H. B., Tokimatsu, K., Harder, L. F., and Chung, R. M. (1985). Influence of SPT procedures in soil liquefaction resistance evaluations. Journal of Geotechnical Engineering, 111(12):1425–1445.

Shen, M., Chen, Q., Zhang, J., Gong, W., & Juang, C. H. (2016). Predicting liquefaction probability based on shear wave velocity: an update. Bulletin of Engineering Geology and the Environment, 75(3), 1199-1214.

Shen, M., Martin, J. R., Ku, C. S., & Lu, Y. C. (2018). A case study of the effect of dynamic compaction on liquefaction of reclaimed ground. Engineering Geology, 240, 48-61, doi:10.1016/j.enggeo.2018.04.003.

Sonmez, H. (2003). Modification of the liquefaction potential index and liquefaction susceptibility mapping for a liquefaction-prone area (Inegol, Turkey). Environmental Geology, 44(7): 862–871.

Stone, M. (1974). Cross-validatory choice and assessment of statistical predictions. Journal of the Royal Statistical Society. Series B (Methodological), 111-147.

Tonkin and Taylor (2013) Liquefaction vulnerability study, Tonkin and Taylor Report 52020.0200/v1.0. February 2013.

Toprak, S., Holzer, T. L., Bennett, M. J., & Tinsley III, J. C. (1999). CPT-and SPT-based probabilistic assessment of liquefaction. In Proc., 7th US–Japan Workshop on Earthquake Resistant Design of Lifeline Facilities and Countermeasures against Liquefaction. Buffalo, NY: Multidisciplinary Center for Earthquake Engineering Research, pp. 69-86.

Toprak, S., & Holzer, T. L. (2003). Liquefaction potential index: field assessment. Journal of Geotechnical and Geoenvironmental Engineering, 129(4), 315-322.

USGS. (2015). United States Geological Survey, CPT Database of Earthquake Hazards Program. http://earthquake.usgs.gov/research/cpt/.

Uzarski, J., & Arnold, C. (Editors). (2001). Chi-Chi, Taiwan, earthquake of September 21, 1999: reconnaissance report. Earthquake Spectra, Vol. 17, Supplement A.

Van Ballegooy, S., Wentz, F., and Boulanger, R. W. (2015). Evaluation of cpt-based liquefaction procedures at regional scale. Soil Dynamics and Earthquake Engineering, 79:315–334.

Vanmarcke, E. (2010). Random Fields – Analysis and Synthesis. World Scientific Publishing Co. Pte. Ltd., Singapore 596224.

Vivek, B. and Raychowdhury, P. (2014). Probabilistic and spatial liquefaction analysis using CPT data: a case study for alameda county site. Natural Hazards, 71(3):1715–1732.

Wang, C., Chen, Q., Shen, M., & Juang, C. H. (2017). On the spatial variability of CPT-based geotechnical parameters for regional liquefaction evaluation. Soil Dynamics and Earthquake Engineering, 95, 153-166.

Wang, C., & Chen, Q. (2017). A hybrid geotechnical and geological data-based framework for multiscale regional liquefaction hazard mapping. Géotechnique, 1-12.

Webster, R. and Oliver, M. A. (1992). Sample adequately to estimate variograms of soil properties. Journal of Soil Science, 43(1):177–192.

Witter, R. C., Knudsen, K. L., Sowers, J. M., Wentworth, C. M., Koehler, R. D., Randolph, C. E., ... & Gans, K. D. (2006). Maps of Quaternary deposits and liquefaction susceptibility in the central San Francisco Bay region, California (No. 2006-1037). Geological Survey (US).

Youd, T. L., & Perkins, D. M. (1978). Mapping liquefaction-induced ground failure potential. Journal of the Soil Mechanics and Foundations Division, 104(4), 433-446.

Youd, T. L., Idriss, I. M., Andrus, R. D., Arango, I., Castro, G., Christian, J. T., Dobry, R., Finn, W.L., Harder Jr. L.F., Hynes, M.E., Ishihara, K., Koester, J. P., Liao, S. S. C., Marcuson, W.F., Martin, G. R., Mitchell, J. K., Moriwaki, Y., Power, M. S., Robertson, P. K., Seed, R. B., & Stokoe, K. H. (2001). Liquefaction resistance of soils: summary report from the 1996 NCEER and 1998 NCEER/NSF workshops on evaluation of liquefaction resistance of soils. Journal of geotechnical and geoenvironmental engineering, 127(10), 817-833.

Zhou, Y.G., Liang, T., Ling, D.S., Chen, Y.M., (2012). Liquefaction performance case histories in Christchurch area during the 2010 and 2011 earthquakes from cone penetration test and shear wave velocity. Proceedings, Second International Conference on Performance-based Design in Earthquake Geotechnical Engineering. May 28–30, 2012, Taormina, Italy.

Zhang, J., Zhang, L. M., & Huang, H. W. (2013). Evaluation of generalized linear models for soil liquefaction probability prediction. Environmental earth sciences, 68(7), 1925-1933.